STUDY OF TRANSPORT PROPERTIES IN MAGNETIC NANOSTRUCTURES

By

KINGSHUK MAJUMDAR

A DISSERTATION PRESENTED TO THE GRADUATE SCHOOL
OF THE UNIVERSITY OF FLORIDA IN PARTIAL FULFILLMENT
OF THE REQUIREMENTS FOR THE DEGREE OF
DOCTOR OF PHILOSOPHY

UNIVERSITY OF FLORIDA

1999

ACKNOWLEDGMENTS

My deepest gratitude goes to my supervisor, Professor Selman Hershfield, for his constant support, encouragement, and guidance. I really learned many technical things from him. He pushed me to learn different numerical techniques which helped me to conduct research efficiently. I will definitely benefit from this training throughout my research career. Other than a physicist and a nice person I will also remember him bar-be-cuing chicken and vegetables in his backyard for our dinner.

I am also very grateful to Professors Peter Hirschfeld, Khandker Muttalib, David Tanner, and Stephen Pearton for serving on my supervisory committee. Thanks to Professor Peter Hershfield for organizing the canoe trips and for the dinner at his place – I really had a wonderful time. Many thanks go to Professor Khandker Muttalib with whom I had fruitful discussions from time to time. I am also thankful to Professor Khandker Muttalib and Dr. Jaha Hamida for their generous hospitality. Specially Dr. Jaha Hamida who used to call me from her laboratory for trying her delicious home-cooked food. I will surely miss the occasional dinner invitations at their residence.

Thanks also to Professors Fred Sharifi, Jeffrey Childress, Mark Meisel, and Arthur Hebard for many interesting discussions. My sincere thanks go to Dr. Avraham Schiller and Dr. Jian Chen who helped me to learn to do numerical calculations at the beginning of my research career. Many discussions with them were both fruitful and enjoyable. One of the most important lesson I learnt from Dr. Avraham Schiller and Professor Selman Hershfield is "how to organize." This

has certainly helped me with my research and also to write this thesis within few weeks. Thanks also to my friend, Tat-Sang Choy, for help with many aspects of my numerical calculations. On the whole I was lucky to meet so many good people in our department specially in our condensed matter group.

I would now like to thank all my friends: Vladimir Boychev, Subrahmanyam Pilla, Kaundiya Gopinath, Steven Patamia, Garrett Granroth, Matthias Hettler, and all others. Without their help I never would have organized our weekly graduate student seminars. Thanks also to the professors of our department for sponsoring the pizza in our student seminars. Besides physics Vladimir helped me many times in different situations. I would like to take the opportunity to thank my other good friends, Dr. Dibyendu Sarkar and Srabanti Sarkar, for many wonderful evenings and good Indian cuisine at their place. Also I thank my roommates, Dr. Raja Chatterjee and Dr. Chhandomay Mandal, for helping me in many occasions. Finally, I would like to thank Dr. Michael Jones and Dr. Youli Kanev for helping with the "documentation."

Most of all I am indebted to my parents and my brother for their constant support and encouragement.

TABLE OF CONTENTS

ACKNOWLEDGMENTS ii

ABSTRACT vi

CHAPTERS

1 INTRODUCTION 1
1.1 Giant Magnetoresistance (GMR) in Magnetic Multilayers 1
1.2 Junction Magnetoresistance (JMR) and Coulomb Blockade in Tunnel Junctions 16
1.3 Magnetization Reversal in Ultra-Thin Magnetic Films and in Ferromagnetic Grains 23

2 GIANT MAGNETORESISTANCE (GMR) IN LATERALLY CONFINED MAGNETIC MULTILAYERS 36
2.1 Semi-Classical Fuchs-Sondheimer's Theory for Thin Films 37
2.2 Generalization to Magnetic Multilayers 43
2.3 Thin wires – Theory and Results 50
2.4 Generalization to Laterally Confined Magnetic Multilayers 63
2.5 Conclusion 75

3 JUNCTION MAGNETORESISTANCE (JMR) IN DOUBLE TUNNEL JUNCTIONS WITH MAGNETIC METALS 77
3.1 Coulomb Blockade in Double Tunnel Junctions 77
3.2 Magnetoresistance in the Coulomb Blockade Regime 86
3.3 Conclusion 99

4 MAGNETIZATION REVERSAL IN SINGLE-DOMAIN THIN FILMS BY EXTERNAL ELECTRIC FIELD 103
4.1 Effect of Electric Field on Magnetic Anisotropy – An Atomic Calculation 103
4.2 Conclusion 112

5 CONCLUSION 113
5.1 GMR in Laterally Confined Magnetic Multilayers 113

5.2 JMR in Tunnel Junctions with Magnetic Metals 114
5.3 Magnetocrystalline Anisotropy in Thin Magnetic Films 117

APPENDICES

A THE SPIN-ORBIT COUPLING MATRIX ELEMENTS 119

B ELECTRIC FIELD MATRIX ELEMENTS 121

REFERENCES 123

BIOGRAPHICAL SKETCH 140

Abstract of Dissertation Presented to the Graduate School
of the University of Florida in Partial Fulfillment of the
Requirements for the Degree of Doctor of Philosophy

STUDY OF TRANSPORT PROPERTIES IN MAGNETIC NANOSTRUCTURES

By

Kingshuk Majumdar

May 1999

Chairman: S. Hershfield
Major Department: Physics

Nanoscale magnetic materials exhibit a wide range of fascinating phenomena which have applications in recent technology. Some of them are giant magnetoresistance in magnetic multilayers, Coulomb blockade in tunnel junctions, and magnetoelectric effect in spin-ordered materials. Understanding the physics behind all these different mechanisms is a challenge to any theorist.

Magnetic multilayers are thin alternating layers of ferromagnets and paramagnets. In these multilayers a large change in resistivity from antiparallel to parallel alignment of magnetizations has been observed. This new phenomenon is called the giant magnetoresistance and is being applied in the recording industry. The physics of giant magnetoresistance in magnetic multilayers has been known for several years. With improved fabrication techniques it is now possible to fabricate nanowires which are laterally confined magnetic multilayers. It is then natural to investigate how the giant magnetoresistance changes with lateral confinement. Theoretical investigation on these laterally confined magnetic multilayers revealed

that in general the giant magnetoresistance decreases with confinement. This reduction can be understood in terms of decrease in the effective mean free path. Also I find that there are special parameter regimes where the giant magnetoresistance increases with lateral confinement.

Transport properties in tunnel junctions with magnetic metals in the Coulomb blockade regime are being studied. In this regime the current-voltage curves take the form of a "staircase" structure. To understand the experimental results we study the magnetoresistance in these tunnel junctions and in the Coulomb blockade regime. My study shows that the magnetoresistance curves exhibit spikes as a function of voltage. The spikes occur at those places where the current increases by a step. The spikes finally disappear at large voltages.

Change of magnetization (or polarization) by applying an electric field (or magnetic field) in some spin-ordered materials is known as the magnetoelectric effect and has been observed experimentally in antiferromagnetic insulators. For thin magnetic films this effect has not been measured. With a simple atomic calculation I show that the electric field can indeed change the orientation of magnetization by changing the magnetic surface anisotropy of the material.

CHAPTER 1
INTRODUCTION

Magnetic nanostructures are electrical devices with smallest dimension of order of a nanometer (0.000000001 meters) [1, 2]. Recent advances in fabrication techniques such as optical, x-ray and electron-beam lithography, molecular-beam epitaxy (MBE), sputtering, and others have made it possible to fabricate such nanostructures. Magnetic nanostructures now play an important role in the commercial market as well as in scientific research activities. Areas of application include the automotive and aerospace industries, medicine, surveillance, information storage systems, communication and manufacturing control. Study of electrical transport properties thus has become essential. In my thesis I discuss the transport properties of three different types of nanostructures: laterally confined magnetic multilayers, double-tunnel-junction with magnetic metals, and thin magnetic films. Before detailing the specific models used to study the transport properties of the above mentioned nanostructures it is useful to review the general methods, the experimental results, and their applications.

1.1 Giant Magnetoresistance (GMR) in Magnetic Multilayers

Magnetic multilayers are thin alternating layers of ferromagnets (FM) and paramagnets (PM) of thicknesses a few angstroms (15–30 Å). Fig. 1.1 is a prototype of a magnetic multilayer. In these layers a large decrease in the resistivity from

antiparallel to parallel alignment of the film magnetizations has been observed experimentally. This new phenomenon is known as the giant magnetoresistance

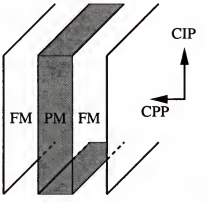

Figure 1.1: Schematic diagram of a 3-layer magnetic structure (FM/PM/FM). A paramagnetic spacer layer (PM) is sandwiched between two ferromagnetic (FM) layers. The direction of the current is shown with the arrows. The current can be in-plane (CIP) or perpendicular to the plane (CPP).

(GMR). Although there were earlier reports of unusual magnetoresistive effects in layered structures [3, 4, 5] it was only around 1988 that GMR effects were first clearly observed and characterized in antiferromagnetically coupled Fe/Cr systems. In Fig. 1.2 we show the first observation of GMR in Fe/Cr multilayers by Baibich et al. [6, 7] and one observes that the resistivity drops dramatically when an applied field aligns the magnetic moments of successive layers. Since then, the quest for larger GMR has continued with different layered structures and films grown either by molecular beam epitaxy (MBE) or by sputtering techniques. All these efforts lead to CIP (current-in-plane) – GMR ranging from 4% - 150% [8] but also have provided us with valuable information. Systematic studies of GMR as a function of the thickness of the spacer layer have shown oscillations in the magnetoresistance. Fig. 1.3 shows one of the result for Co/Cu multilayers obtained

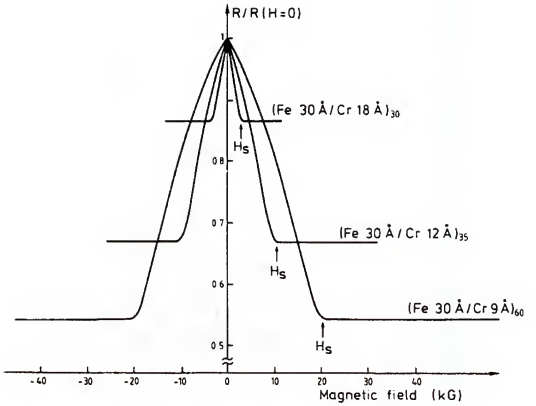

Figure 1.2: Magnetoresistance of three Fe/Cr superlattices at 4.2 K for different Cr thicknesses as measured by Baibich et al. [6] The current and the applied field are along the same [110] axis in the plane of the layers. H_s is the saturation field required to align the magnetizations of the Fe layers in parallel.

by Parkin [9, 10, 11]. A large GMR is present when the layers are antiferro-

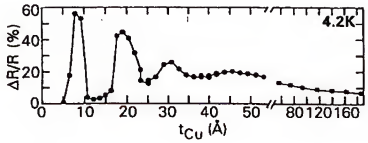

Figure 1.3: Magnetoresistance (MR) for Co (10 Å)/Cu (t_{Cu}) measured by Parkin et al. [9] Magnetoresistance oscillates as a function of the spacer layer thickness which indicates that there is an interlayer exchange coupling between the ferromagnetic layers.

magnetically coupled and a very small GMR otherwise. The oscillations indicate that there is an interlayer exchange coupling of Ruderman-Kittel-Kasuya-Yosida (RKKY) type between the magnetic layers [12]. The GMR is generally due to the interplay between spin dependent scattering in successive magnetic layers. The conditions for the interplay is that the distance between the layers is relatively small in comparison with the mean free path of the electron. The variation of the GMR with the thickness of the magnetic layers also contains potential information about the ratio of bulk and interfacial spin dependent scattering. In this context it is useful to mention that bulk scattering means that the mean free paths of the electrons are spin-dependent. On the other hand interface scattering arises due to the difference between transmission and reflection coefficients for the spin-up and spin-down electrons at the interface.

Influence of interface structure plays an important role on the GMR and also have been studied by various groups [8, 13, 14]. It has been found that the spin-

dependent scattering by the interfaces is enhanced when the surfaces are "rougher" which thus increases the GMR.

GMR also depends on the direction of the current. In most experiments the current flows in the plane of the layers, this is the CIP (current-in-plane) geometry. However, magnetoresistance measurements also have been done for the case where the current is perpendicular to the plane – this is known as the CPP geometry (see Fig. 1.1). Vertical transport (CPP) is the common mode for using semiconducting superlattices, but for a given sample of 1 μm thick and area 1 mm^2 in the plane of the layer the resistance is one million times smaller for CPP than CIP. Thus, it is harder to measure the CPP resistance by conventional means. However, CPP-MR ratio has been measured in sputtered Co/Cu and Ag/Co superlattices by a group in Michigan State University [15, 16] and a value of 170% has been obtained. The GMR in CPP geometry exhibits similar oscillations as a function of the thickness of the non-magnetic spacer layers, and decreases less rapidly at large thicknesses. Fig. 1.4 shows the experimental result [15, 16].

Temperature dependence of the GMR is of critical importance to its applications. It has been seen that the MR ratio drops with increase in temperature [13]. Fig. 1.5 illustrates this feature. Several aspects contribute to the decrease in GMR. At higher temperature inelastic scattering processes (with phonons, magnons, etc.) come into play which reduces the mean free path which then decreases the magnetoresistance.

Since the discovery of giant magnetoresistance in magnetic multilayers many different theoretical models, both classical and quantum, have been proposed to understand the various features of the GMR seen in the experiment [17, 18, 19, 20].

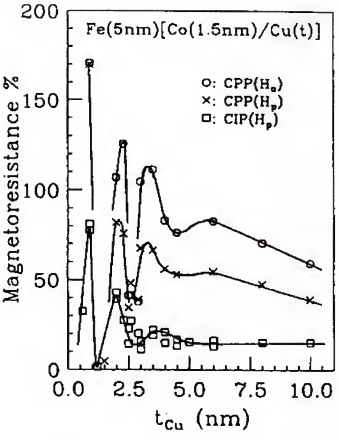

Figure 1.4: The magnetoresistance of Co/Cu layers at T =4.2 K as a function of the thickness of the spacer layer (Cu) for currents perpendicular to the plane of the layers (CPP) as measured by the Michigan State University group. The change in resistance is measured from the zero field value to saturation (H_0), and from its peak value after recycling through the hysteresis curve (H_p). Comparing the reproducible peak values of the CIP-MR with CPP-MR shows that CPP-MR is much larger than the CIP-MR.

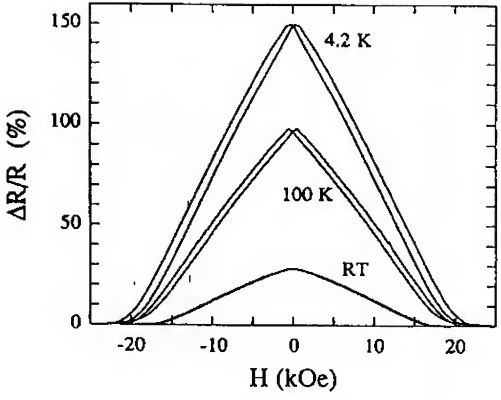

Figure 1.5: Magnetoresistance as a function of the magnetic field at different temperatures as measured by Bader's group [8]. A maximum CIP-MR of 150% is observed at 4.2 K (28% at room temperature) for Fe/Cr superlattices.

Fuchs-Sondheimer's semiclassical theory for the conduction in thin films has been known since 1950s [21, 22]. It was later extended by Camley and Barnaś for the CIP geometry to magnetic multilayers [23]. Their model has been used extensively to numerically calculate the magnetoresistance in multilayers [24, 25, 26] . In the limit where the thickness of the magnetic multilayers is much larger than the mean free path of the conduction electrons Barthélémy and Fert obtained simple analytical expressions for the GMR [27]. In the limit of very long mean free path analytical results have been obtained by Edwards et al. [28] Various modifications of the model of Camley and Barnaś have been proposed. For example, to describe the scattering at the interface Johnson and Camley [29] introduced a thin interfacial layer with a shorter mean free path. Hood and Falicov took into account the potential scattering by the interfaces [30]. For CPP geometry theoretical models based on Boltzmann equation have also been worked out [31, 32].

In the regime when the film thickness becomes smaller than the electron mean free path, the semiclassical theory of Fuchs and Sondheimer predicts that the resistivity varies as the inverse of the logarithm of the mean free path. In the limit of infinite mean free path, the resistivity becomes zero which implies that in the absence of bulk scattering there is no contribution due to surface scattering. One would rather expect a finite surface scattering and therefore a finite residual resistivity in this limit. To correct this non-physical result, the quantum theory of transport in thin metallic films in the presence of disorder was first developed by Tesanovic et al. [33] This can also be understood by considering the Landauer conductance formula [34] in the absence of disorder and for temperatures much less than the Fermi energy ($k_B T << E_F$). The conductance (G) is expressed in

terms of the number of channels (N). For a 3D film of length L with finite cross section S the number of channels $N = Sk_F^2/4\pi$ where k_F is the Fermi wave vector. The end result for the conductance is

$$G = \frac{2e^2}{h}N = \frac{2e^2}{h}\left(\frac{Sk_F^2}{4\pi}\right) = \frac{\sigma S}{L}. \tag{1.1}$$

where σ is the conductivity. The conductivity is now obtained from the conductance as

$$\sigma = \frac{LG}{S}. \tag{1.2}$$

This result shows that the conductivity is always finite for a sample of finite size. Different quantum models of GMR based on Kubo formalism [17, 35, 36, 37, 38, 39, 40, 41], Landauer-Buttiker formalism [42], quantum Boltzmann equation [43], ab-initio calculations using realistic superlattice band structures [44, 45, 46, 47] etc. have been developed.

The basic qualitative features of the giant magnetoresistance can be understood classically by a simple model [19]. In this model one assumes that the GMR is entirely due to the bulk scattering, the mean free path of the electrons within the layers (100 Å is a typical value) is much larger than the thickness of the layers, and there is no spin-flip scattering. Fig. 1.6 schematically shows the mechanism of the magnetoresistance. For high magnetic fields the magnetizations are parallel. One can then imagine this as an electrical circuit with two resistivity channels (for majority and minority electrons) in parallel (Fig. 1.6a). Depending on the spin directions $s_z = 1/2$ or $s_z = -1/2$ the scattering probabilities and therefore the resistivities are different. The majority electrons with $s_z = 1/2$ form a low

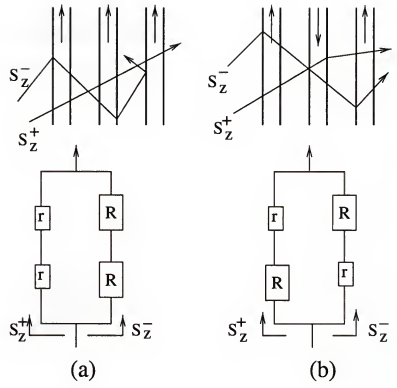

Figure 1.6: Schematic diagram of conduction in multilayer magnetic films showing how spin scattering produces a different resistance for parallel (case a) and anti-parallel (case b) alignments of magnetizations [19]. When the magnetizations are parallel (case a) it is relatively easy for spin-up (S_z^+) electrons (majorities) to move freely within the layers (less scattering) where as spin-down (S_z^-) electrons (minorities) scatter the most. Equivalent resistor array for parallel alignments is shown below. R and r are the resistances for the spin-down and the spin-up electrons. For case (a) r is smaller than R thus the effective resistance is lower. For case (b) magnetizations are anti-parallel – no electron can traverse two magnetic layers without becoming the unfavored highly scattered species. Thus in this case the high and the low resistances are in series and the effective resistance is larger than the effective resistance in case (a).

resistivity channel throughout the sample.

$$\rho_F = \frac{\rho^{\uparrow}\rho^{\downarrow}}{(\rho^{\uparrow} + \rho^{\downarrow})}. \tag{1.3}$$

Fig. 1.6b represents the opposite case with an antiparallel alignments of the magnetizations in successive layers. In this case the low resistivity electrons (majority electrons) in a layer becomes the high resistivity electrons (minority electrons) in the next. Each channel has the average resistivity $(\rho^{\uparrow} + \rho^{\downarrow})/2$ and the final resistivity is high

$$\rho_{AF} = \frac{(\rho^{\uparrow} + \rho^{\downarrow})}{4}. \tag{1.4}$$

The magnetoresistance in the infinite mean free path limit is then:

$$\text{GMR} = \frac{\rho_{AF} - \rho_F}{\rho_{AF}} = \left(\frac{\rho^{\downarrow} - \rho^{\uparrow}}{\rho^{\downarrow} + \rho^{\uparrow}}\right)^2. \tag{1.5}$$

The above result shows that in the absence of bulk scattering, i.e. $\rho^{\uparrow} = \rho^{\downarrow}$, there is no magnetoresistance. But this is not true for a real system. GMR is due to both bulk and interface scattering, so even in the absence of bulk scattering there is GMR due to the interface scattering alone. The above simple model can be generalized for a FM/PM/FM multilayer with different thicknesses. Let t_{FM} and t_{PM} are the thicknesses of the ferromagnet and the paramagnet, respectively. Then the total resistivity for the majority electrons (with $S_z = 1/2$) is obtained by adding the resistivities for the individual layers in series. In terms of the resistivity

($\rho^{\uparrow\uparrow}$) of the majority electrons we have:

$$\rho^{\uparrow\uparrow} = \frac{2t_{\rm FM}\rho^{\uparrow} + t_{\rm PM}\rho^{\rm PM}}{2t_{\rm FM} + t_{\rm PM}}. \tag{1.6}$$

Similarly, the resistivity ($\rho^{\downarrow\downarrow}$) for the minority electrons (with $S_z = -1/2$) is given by:

$$\rho^{\downarrow\downarrow} = \frac{2t_{\rm FM}\rho^{\downarrow} + t_{\rm PM}\rho^{\rm PM}}{2t_{\rm FM} + t_{\rm PM}}. \tag{1.7}$$

The total resistivity for the parallel alignments of the magnetizations is then obtained by adding the resistivities in Eqs. (1.6) and (1.7) in parallel:

$$\rho_F = \frac{\rho^{\uparrow\uparrow}\rho^{\downarrow\downarrow}}{\rho^{\uparrow\uparrow} + \rho^{\downarrow\downarrow}}. \tag{1.8}$$

Proceeding in the same way the total resistivity for the anti-parallel alignments of the magnetizations (in this case $\rho^{\uparrow\downarrow} = \rho^{\downarrow\uparrow}$) is

$$\begin{aligned} \rho_{AF} &= \frac{\rho^{\uparrow\downarrow}\rho^{\downarrow\uparrow}}{\rho^{\uparrow\downarrow} + \rho^{\downarrow\uparrow}} \\ &= \frac{\rho^{\uparrow\downarrow}}{2} \\ &= \frac{t_{\rm FM}\rho^{\uparrow} + t_{\rm PM}\rho^{\rm PM} + t_{\rm FM}\rho^{\downarrow}}{2(2t_{\rm FM} + t_{\rm PM})}. \end{aligned} \tag{1.9}$$

Using Eq. (1.5) the magnetoresistance for bulk scattering is now given by:

$$\text{GMR(Bulk)} = \left[\frac{t_{\rm FM}(\rho^{\uparrow} - \rho^{\downarrow})}{t_{\rm FM}(\rho^{\uparrow} + \rho^{\downarrow}) + t_{\rm PM}\rho^{\rm PM}}\right]^2. \tag{1.10}$$

In the limit of $t_{\rm PM} \to 0$ we recover Eq. (1.5) from Eq. (1.10).

These new phenomenon in magnetism has been combined with electronics to build new devices [48]. For example, magnetic sensors have wide applications in our present day technology [49]. Applications include magneto-optic sensors, anti-theft devices, Hall effect sensors, different kinds of magnetometers such as fiber-optic magnetometers, SQUID magnetometers, search-coil magnetometers, flux-gate magnetometers, and many others. The motivation driving the research in GMR both theoretically and experimentally is its application in the hard disk drive industry [50]. High sensitive read heads made of giant magnetoresistive materials have been introduced recently. The GMR head employs a sensor whose resistance changes in the presence of a magnetic field. Its performance gain has enhanced the density of storage by more than 50%. GMR also increase the MR strip sensitivity dR/R to provide higher signal amplitudes [51, 52]. A prototypical MR head is shown in Fig. 1.7. The head senses the magnetic field from the recorded bit. With

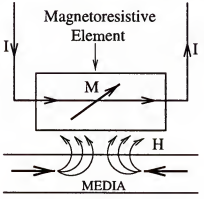

Figure 1.7: Schematic diagram of a magnetoresistive "read" head [50]. With a GMR material in the "read head", the resistance changes with a small change in the magnetic field.

a GMR material in the sensor the resistance of the material changes with change in

the magnetic field. For better performance one needs larger sensitivity i.e. dR/dH to be large which means a large change in the resistance with a small change in the magnetic field.

Another application of GMR materials is in the magnetic random access memory (MRAM) [53, 54]. In MRAM technology two particular properties of magnetic materials are used: uniaxial anisotropy and magnetoresistance. Uniaxial anisotropy aligns the magnetization along the easy axis. The magnetization will thus point in one of the two antiparallel directions which are used to store "1" or a "0". The magnetoresistance property of the material can then be used to distinguish between a "1" or a "0" in a MRAM cell. The basic MRAM cell configuration is a magnetic sensing line and an orthogonal and insulated word line which is shown in Fig. 1.8. The magnetic sense line consists of thin magnetic films sandwiched

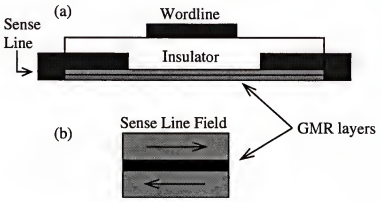

Figure 1.8: A GMR based MRAM cell: (a) cross-section along the sense line and (b) the direction of the magnetic field across the sense line due to a current in the line which goes into the paper [53].

between a nonmagnetic layer. The magnetic thin films are made of giant magnetoresistive materials. Due to interlayer exchange coupling the magnetic fields

align across the sense line in opposite directions in the top and the bottom film (as shown by the arrows in Fig. 1.8b) with the application of a current (which goes into the page). About the sense current the storage states are either in clockwise or in anticlockwise orientation of the magnetizations in the sandwich layers. A one or zero is written into a two-dimensional array of these cells by a word current in combination with a sense current of appropriate polarity. MRAM chips with up to 16 kilobits of storage have been demonstrated. Designs of chips with up to a million bits are now in progress.

With such a tremendous progress in nanofabrication techniques it is now possible to laterally confine the magnetic multilayers [55, 56, 57]. Multilayered wire

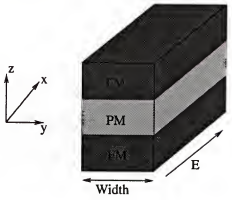

Figure 1.9: Schematic diagram of a laterally confined magnetic multilayer. PM is the paramagnetic layer sandwiched between two ferromagnetic (FM) layers. The direction of the electric field (E) is in the plane of the layers (CIP).

arrays have been fabricated recently by high-resolution electron-beam lithography and lift-off techniques to study finite size effects and giant magnetoresistance [58, 59]. A prototype of a laterally confined magnetic multilayer is shown in Fig. 1.9. Laterally confined magnetic multilayers hold the potential to be used

in future technologies [60]. It is then natural to study these laterally confined magnetic multilayers. Understanding the effect of lateral confinement on GMR theoretically is the primary focus of my investigation [61].

1.2 Junction Magnetoresistance (JMR) and Coulomb Blockade in Tunnel Junctions

Electron tunneling is a quantum phenomenon in which the electrons travel from one electrode to another through a thin oxide layer which acts as an insulating barrier. This three-layer system – electrode, barrier, and counter-electrode is referred to as tunnel junction. The quantity usually measured in a tunneling experiment is the current or its derivative as a function of applied voltage [62].

Some of the earliest experiments were on tunneling between a superconductor and a ferromagnet [63]. In these experiments, the difference between the spin-up and spin-down density of states of a superconductor in a magnetic field was observed [64]. These experiments also provided a quantitative measure of the spin polarization of the current from the ferromagnetic metal.

Later experiments were done on tunneling between two ferromagnetic metals [65]. Because of the spin dependence of the density of states, the conductance changed when the relative orientation of the two magnetizations changed. One of the measurable quantities of practical importance is the junction magnetoresistance, which is defined as the ratio of the change in the conductance from parallel to antiparallel alignment divided by the parallel conductance. Large magnetoresistance response in low magnetic fields has been observed in a variety of tunnel junctions by several groups [66, 67, 68, 69, 70, 71, 72, 73, 74, 75, 76, 77]. Fig. 1.10

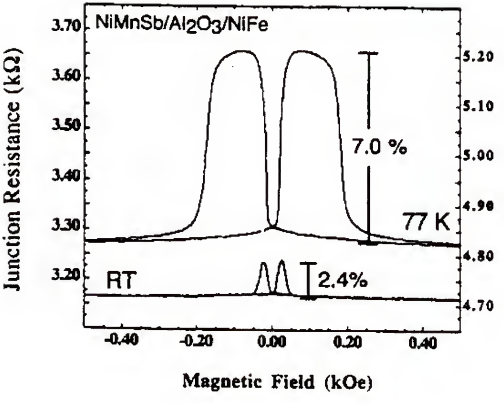

Figure 1.10: Magnetoresistance for $NiMnSb/Al_2O_3/NiFe$ junction at room temperature and 77 K [66]. The left scale corresponds to the room temperature (RT) curve, the right to the 77 K data. The broad peak at 77 K indicates well-separated coercive forces of the ferromagnets and antiparallel orientation at the peak. The sharp peak at RT indicates that the coercivities of the two FM's are close to each other which implies that complete antiparallel orientation is not achieved at the peaks. The maximum value obtained for JMR is about 2.4% at RT where as highest JMR observed at 77 K is about 7.0%.

shows the JMR as a function of the magnetic field measured by Tanaka et al. [66] From the point of view of application higher value of JMR as well as low junction resistance of the order of 1 $k\Omega/\mu m^2$ is required. Very recently such a value for the resistance has been obtained [78]. Using half-metallic compounds as electrodes can also increase the value of JMR. At the Fermi level the half-metallic compounds have only one spin-direction which is reflected as a gap in the density of states. Examples of such compounds are Heusler alloys [79, 80, 81].

To estimate the junction magnetoresistance, Julliere in 1975 proposed a simple model based on the free electron picture [65]. For a ferromagnetic-insulator-ferromagnetic (FM/I/FM) tunnel junction the conductance depends on the relative magnetizations of the two ferromagnetic electrodes. For magnetizations parallel in both the electrodes we define the conductance to be G^{P} and G^{AP} is the conductance when the magnetization of the electrodes are anti-parallel. Let a_1 and a_2 be the fraction of the number of spins parallel to the magnetization and N_1 and N_2 the density of states of the electrons at the Fermi level in the two ferromagnets. Using Fermi's golden rule we obtain the two conductances which are

$$G^{\mathrm{P}} = \left(\frac{e^2}{h}\right) |T|^2 N_1 N_2 \{a_1 a_2 + (1-a_1)(1-a_2)\}, \tag{1.11}$$

$$G^{\mathrm{AP}} = \left(\frac{e^2}{h}\right) |T|^2 N_1 N_2 \{a_1(1-a_2) + (1-a_1)a_2\}. \tag{1.12}$$

Here the tunneling matrix element T, is taken to be both energy and momentum independent. Using the definitions of the spin polarizations P_1 and P_2 of the two

ferromagnets

$$P_1 = 2a_1 - 1, \tag{1.13}$$

$$P_2 = 2a_2 - 1. \tag{1.14}$$

Eqs. (1.11) and (1.12) can be rewritten in terms of P_1 and P_2. The junction magnetoresistance (JMR) is defined as the ratio of the change in the conductance from parallel, G^{P} to antiparallel alignments, G^{AP}, divided by the parallel conductance

$$\mathrm{JMR} = 1 - \frac{G^{\mathrm{AP}}}{G^{\mathrm{P}}}. \tag{1.15}$$

The above expression for JMR can also be rewritten in terms of the polarizations

$$\mathrm{JMR} = \frac{2P_1P_2}{(1 + P_1P_2)}. \tag{1.16}$$

For a Fe/Ge/Co junction using the polarization values (P_1=44%, P_2=34%) as measured by Tedrow and Meservey on Al-Al_2O_3-ferro junctions Julliere estimated the value of JMR from Eq. (1.16) to be 26%. The maximum measured experimental value for this Fe/Ge/Co tunnel junction is about 14%. The discrepancy between the experimental value and the theoretically predicted value may be due to spin-flip processes, magnetic impurities, and other mechanisms.

Besides spin, electrons carry charge and at low temperatures in tunnel junctions with small capacitance, the discreteness of electron charge manifests itself through the physics of the Coulomb blockade [82, 83, 84, 85, 86, 87]. The transfer of an electron by tunneling between two initially neutral regions of capacitance C

increases the electrostatic energy of the system by an amount $e^2/2C$. At low temperatures and small voltages, the tunneling current is suppressed because of the charging energy. This energy barrier is called the Coulomb blockade. The effect of this in a two-junction system (a prototype of which is shown in Fig. 1.11) is the incremental increase in the current at voltages where it is energetically favorable for an electron to tunnel to the center island. The occurrence of these current steps in the current-voltage characteristics is known as the "Coulomb staircase." One

Figure 1.11: The basic structure of a double tunnel junction. The source, island, and the drain are the electrodes separated by insulating layers.

of the recent experiments on the Coulomb blockade phenomenon in nanoparticles is by Ralph et al. [88] Using electron-beam lithography and reactive-ion etching techniques his group fabricated a bowl-shaped hole in a suspended silicon nitride membrane (See Fig. 1.12a). The orifice has a size between 5 and 10 nm in diameter. A single particle is then formed by deposition techniques under the nm-scale tunnel junction to contact the top and the bottom Al electrodes. Electrons tunnel from the top to the bottom electrode through the single nano-particle. The gate voltage tunes the number of electrons in the particle. In this device geometry the current plotted as a function of the voltage clearly shows the Coulomb staircase structure (Fig. 1.12).

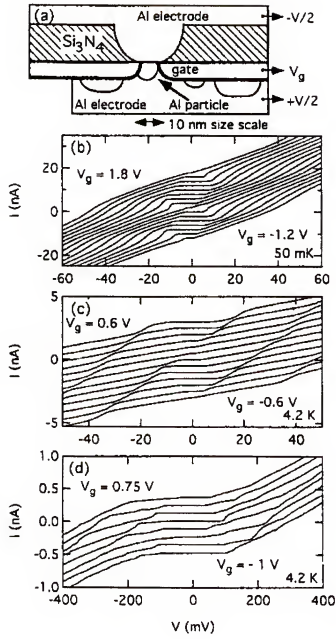

Figure 1.12: (a) Schematic cross section of the device geometry. Electrons tunnel between the top and the bottom electrodes through a single nanoparticle. The gate voltage V_g controls the flow of the electrons. Figs. (b) - (d) display the Coulomb-staircase structure for different samples, at equally spaced values of gate voltage [88].

There are number of new experiments which exhibit the Coulomb blockade phenomenon: granular thin films [89, 90], lithographically patterned tunnel junctions [88, 91, 92, 93, 94], narrow disordered quantum wires [95, 96], scanning tunneling microscopy of small metal droplets [97], metal-insulator-metal tunnel junctions with small metal particles embedded in the insulator [98, 99, 100, 101].

Recently there have been experiments where spin-polarized tunneling and the Coulomb blockade have been combined [102, 103, 104, 105, 106]. In discontinuous metal/insulator multilayers consisting of closely spaced ferromagnetic nanoparticles in an insulating matrix a Coulomb blockade is seen (Fig. 1.13) in the current-voltage characteristic at low temperatures.

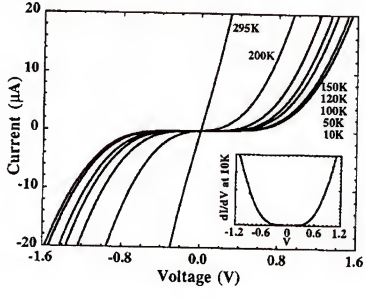

Figure 1.13: I(V) at different temperatures for the annealed multilayer [CoFe(15 Å)HfO_2(40 Å)]$_{20}$ [102]. At low temperature we see a Coulomb blockade. In the inset the differential conductance (dI/dV) at 10 K is plotted to show the magnitude of the Coulomb blockade (0.3 V).

To explain the recent experimental results theories have been proposed [107, 108, 109]. The role of electronic structure in magnetic tunneling has also been studied [110, 111, 112].

Spin-transistors and spin-polarized field-effect-transistor (known as spin FET) are based on the application of spin-polarized transport [113]. In the near future it may be possible to make a device which combines both of these effects (spin-polarized tunneling and Coulomb blockade) [114]. The purpose of my work is to theoretically study the different transport properties of a double-tunnel-junction with magnetic metals at low temperatures where the phenomenon of Coulomb blockade has been seen [108].

1.3 Magnetization Reversal in Ultra-Thin Magnetic Films and in Ferromagnetic Grains

One of the present day research areas in magnetics is focussed on the phenomenon of magnetization reversal in ultra-thin magnetic films and in single domain magnetic nano-particles [115, 116, 117, 118, 119]. Magnetization reversal in nanoscale ferromagnets has potential application in the next-generation recording media such as magnetic tapes and disks. During recording different regions of the recording medium are briefly exposed to strong magnetic fields so that each grain is magnetized in a certain direction. For better storage devices the grains should retain their magnetization for long periods of time. The grain size and the lifetime of the magnetization opposed to the applied magnetic field are therefore of considerable technological interest.

Magnetization reversal by droplet formation is a possible scenario in single-domain nanoscale ferromagnets [120, 121, 122, 123, 124, 125, 126, 127] but the standard theory is due to Néel [128] and Brown [129, 130]. Before we discuss Néel-Brown's theory [131] let us illustrate the phenomenon of magnetization reversal with a simple example from statistical mechanics. Consider a spin-chain. We apply a magnetic field large enough to saturate the magnetization of this chain in the field's direction. We then slowly reduce the field to zero and then increase slowly in the opposite direction. At some stage during this process, the initial state will become unstable, and some change will start to take place. Finally the magnetization will saturate in the opposite direction. The field at which the original saturated state becomes unstable and any change in magnetization just starts is called the nucleation field (also known as the switching field). The transition state between the initial and the final stable states is known as the metastable state. Metastable phases are observed in a wide variety of systems in condensed matter physics, high energy physics, and in cosmology. A few examples are supercooled liquids, permanent magnets, ferroelectrics, in certain alloys, in the electroweak phase transition, and the supercooled quark-gluon plasma associated with the QCD confinement transition [132]. A fully satisfactory description of the metastable phase would be extremely helpful to understand all these different systems. Some of the pertinent questions to ask are: (1) How does a metastable state decay into a more stable state? (2) How long is the switching time, i.e. the time to go from one stable state to another stable state? (3) What are the factors the switching time depend on and how can one control the switching time?

Nanoscale ferromagnetic grains have been studied for many years, but recently with magnetic force microscopy (MFM) and Lorentz microscopy the magnetic properties of individual single-domain particles are studied. Chang et al. [133] used MFM to study the dependence of the switching field with the diameter of isolated barium ferrite fine particles. The resulting effective field has a peak at a grain diameter of about 55 nm. MFM measurements in individual iron particles [134] showed that the switching fields decrease with the increase of the particle diameters from 20 to 70 nm. Study of size effects in single-domain Ni bars [135] also shows peak in the switching field at a width of 55 nm which then decreases with increase in the bar-width. Another set of experiments involved the measurement of the probability P that the magnetization in γ-Fe_2O_3 [119] single-domain particles is switched by an opposing field. The experiments show that the mean switching time depends strongly on the strength of the applied field.

To understand the phenomenon of magnetization reversal we need to study Brown's equation of micromagnetics [130, 136]. We consider a ferromagnetic body of any shape in which the magnetization is a function of space. The total energy (ϵ) then consists of four terms: the exchange energy (ϵ_e), the anisotropy energy (ϵ_a), the magnetostatic energy (ϵ_M), and the Zeeman energy (ϵ_H):

$$\epsilon = \epsilon_e + \epsilon_a + \epsilon_M + \epsilon_H. \tag{1.17}$$

The only term which is left out in Eq. (1.17) is magnetostriction. When a ferromagnet is magnetized it shrinks (or expands) in the direction of the magnetization – this is know as magnetostriction. In some cases magnetostriction can be absorbed

inside the anisotropy term. The exchange energy stems from the interaction between the neighboring spins. Written in terms of the magnetization unit vectors it takes the following form:

$$\epsilon_e = \frac{C}{2} \int d\tau \left[(\nabla m_x)^2 + (\nabla m_y)^2 + (\nabla m_z)^2 \right], \tag{1.18}$$

where C is a constant which depends on the coupling constant (assumed to be constant), lattice spacing, and size of the spins.

For most cases the Hamiltonian for a crystal is not isotropic which means that the energy levels depend on the direction in space in which the crystal is magnetized. This is known as anisotropy [137]. For example the anisotropy of hexagonal crystals depend only on the angle (θ) between the c-axis and the direction of magnetization. The anisotropy energy density in this case is

$$\begin{aligned} w_a &= K_1 \sin^2\theta + K_2 \sin^4\theta \\ &= K_1(1 - m_z^2) + K_2(1 - m_z^2)^2, \end{aligned} \tag{1.19}$$

where K_1 and K_2 are known as anisotropy constants. Depending on the magnetic material K_1 and K_2 can have both signs. K_2 is usually an order of magnitude smaller than K_1, so the sign of K_1 determines whether the magnetization prefers in-plane or perpendicular to the plane. For example in Fe films, K_1 is positive [138, 139, 140, 141, 142], so the magnetization prefers to be perpendicular to the plane. On the other hand, K_1 is negative for Ni and Co films – magnetization thus prefers

to be in-plane [140]. In general the total anisotropy energy can be written as

$$\epsilon_a = \int d\tau \; w_a + \int ds \; w_s. \tag{1.20}$$

Here w_a and w_s are the volume and the surface anisotropy densities, respectively.

The origin of the magnetostatic term is the coupling of the magnetization with the internal field ($\mathbf{H}_{\text{int}}$) due to the dipoles:

$$\epsilon_M = -\frac{1}{2} \int d\tau \mathbf{M} \cdot \mathbf{H}_{\text{int}}. \tag{1.21}$$

The remaining Zeeman term is due to the response of the external magnetic field ($\mathbf{H}_{\mathbf{a}}$)

$$\epsilon_H = -\int d\tau \mathbf{M} \cdot \mathbf{H}_{\mathbf{a}}. \tag{1.22}$$

Brown's equation can be obtained by minimizing the total energy in Eq. (1.17) and the result is

$$\mathbf{m} \times \mathbf{H}_{\text{eff}} = 0, \tag{1.23}$$

with the constraint $|\mathbf{m}| = 1$. $\mathbf{H}_{\text{eff}}$ in Eq. (1.23) is defined as

$$\mathbf{H}_{\text{eff}} = \frac{C}{M_s} \nabla^2 \mathbf{m} + \mathbf{H} - \frac{1}{M_s} \frac{\partial w_a}{\partial \mathbf{m}}. \tag{1.24}$$

M_s is the saturation magnetization in the above equation. Eq. (1.23) implies that in equilibrium the total torque is zero everywhere and the magnetization is parallel to an effective field. Brown's equations have been solved for different geometries and the nucleation fields also have been calculated in each case. Buckling, curling,

fanning, uniform rotation are different theoretical relaxation processes for different cases [131]. Using the effective field we can also study the details of magnetization configurations and magnetization reversal processes in magnetic materials. The dynamics of magnetization orientation follows the famous Landau-Lifshitz-Gilbert equation:

$$\frac{d\mathbf{M}}{dt} = -\gamma \mathbf{M} \times \mathbf{H} - \frac{\lambda}{M} \mathbf{M} \times (\mathbf{M} \times \mathbf{H}), \tag{1.25}$$

where γ is the electron gyromagnetic ratio and λ is the damping constant. Based on Eq. (1.25) which is the basic equation of micromagnetic theory one can simulate complete magnetization processes for different geometries [143, 144, 145]. Micromagnetic modeling enriches our understanding about the formation of complex domains.

In Néel-Brown's theory one assumes uniform rotation of all the atomic moments in the system. This is to avoid the energy barrier due to exchange interactions between atomic moments with unlike orientations. The remaining barrier is due to magnetic anisotropy, either intrinsic or shape-induced. Anisotropy makes it energetically possible for each atomic moment to be aligned along one of the "easy" axes. We consider a simple scenario where the total energy consists of the leading order term in the anisotropy energy and the Zeeman term (magnetic field is applied along the z direction)

$$E = K_1 V \sin^2 \theta - M_s V H \cos \theta, \tag{1.26}$$

where V is the volume. The energy is plotted as a function of θ in Fig. 1.14.

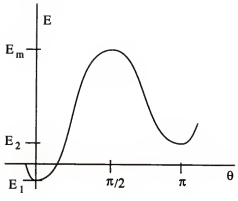

Figure 1.14: Energy as a function of the angle between the z axis and the magnetization. the two minima are at $\theta = 0$ and at $\theta = \pi$.

There are two minima, one at $\theta = 0$ and one at $\theta = \pi$ with energies $E_1 = -M_s V H$ and $E_2 = M_s V H$ respectively with an energy barrier between them. At thermal equilibrium, the magnetization will be in the vicinity of these minima. The peak value of the energy is given by

$$E_m = K_1 V \left[1 + \left(\frac{H M_s}{2K_1}\right)^2\right]. \tag{1.27}$$

The nucleation field H_N can be obtained by minimizing the total energy (Eq. (1.26))

$$H_N = \frac{2K_1}{M_s}. \tag{1.28}$$

Due to thermal fluctuations particles can jump from one minimum to the other. The number of particles jumping over the barrier from minimum 1 to minimum 2 per unit time can be written as

$$\nu_{12} = c_{12} e^{-\beta(E_m - E_1)}, \tag{1.29}$$

where c_{12} is a constant and β is related to the temperature (T) via $\beta = 1/(k_B T)$ (k_B is the Boltzmann constant). Similarly, the number of particles jumping over the barrier from minimum 2 to 1 per unit time is

$$\nu_{21} = c_{21} e^{-\beta(E_m - E_2)}, \tag{1.30}$$

where c_{21} is another constant. For the case of zero magnetic field ($H = 0$) the barrier is the same in either directions, and these two constants c_{12}, c_{21} are the same. The relaxation time τ which is the average time the system takes (for $H = 0$) to jump from one minimum to another is given by

$$\frac{1}{\tau} = f_0 e^{-KV/k_B T}, \tag{1.31}$$

where f_0 is a constant of the order of 10^{10} s^{-1} which can be obtained by solving Brown's equation. The essence of this simple calculation for the nucleation field and the relaxation time is that both can be changed by changing the temperature or the anisotropy (and also the magnetic field in the general case).

The dependence of the energy of a ferromagnetic metal on the direction of magnetic moment is known as magnetocrystalline anisotropy (MCA) and is one of the most important properties of ferromagnetic materials. Specially in thin films a large anisotropy is seen to be present at the surface. This is now commonly known as surface anisotropy and has attracted attention from both theorists and experimentalists [140, 142, 146, 147]. The total energy due to surface anisotropy (typically 0.1-1.0 meV/atom) is also few orders of magnitude larger than the total energy due to bulk anisotropy (few μeV/atom) per unit length. The

reduced symmetry, the lower coordination number, and the role of highly localized surface states offer new phenomena which may have applications in future electronic devices. As an example it has been seen in photoemission experiments [148] that in a ferromagnetic thin film the magnetic moment is enhanced at the surface [148, 149]. Using SQUID magnetometry enhanced magnetic moments for Fe on Ag(100) with interface moments enhanced by as much as 29% have been observed recently [150]. The reduced coordination number at the surface leads to narrowing of the d bands which thus increases the density of states at the Fermi level. This is reflected in the enhancement of the magnetic moment at the surface. Self-consistent electronic structure calculations also predict this unusual feature [151, 152, 153, 154, 155, 156, 157, 158].

Attempts to understand the origin of the magnetocrystalline anisotropy started many years ago [159]. More than 60 years ago Van Vleck [137] proposed that the origin of anisotropy is a relativistic effect due to the coupling of the spin of the electrons with the angular momentum. The magnetic dipole and other possible anisotropic exchange interactions also play roles in the magnetocrystalline anisotropy. In transition metals the spin-orbit coupling is smaller than the crystalline field which makes the theoretical calculations much more difficult. Many theoretical attempts using *ab initio* calculations [160, 161, 162], perturbative techniques based on tight-binding model [163, 164, 165], non-perturbative techniques [166, 167], etc. have been employed to calculate the anisotropy energy which is several orders of magnitude smaller than other contributions to the total energy of a crystal. All these calculations indicate that the anisotropy energy is extremely sensitive to the details of the band structure at the Fermi level – thus

correct estimation of the anisotropy energy is still a numerical challenge. The dependence of the MCA on the number on layers also have been studied both experimentally [140] and theoretically [164, 166, 168, 169, 170]. It has been seen that for thin Fe films deposited on Cu(001) a transition from magnetization perpendicular to film to magnetization in-plane occurs at 5 ML [140, 141]. On the other hand, no such transition occurs for Ni and Co slabs. At this point it is worthwhile to mention that in the anisotropy energy there are two competing effects – one due to spin-orbit coupling which prefers the magnetization to be perpendicular to the plane and the shape anisotropy which prefers the magnetization to be in-plane. Shape anisotropy originates from magnetic dipole-dipole interactions and for a monolayer the energy due to shape anisotropy is given by

$$E_{\text{shape}} = -\frac{1}{2}\mathbf{M_s} \cdot \mathbf{H}, \tag{1.32}$$

where the field $\mathbf{H} = \mathbf{N} \cdot \mathbf{M_s}$. $\mathbf{N}$ is known as the demagnetization factor which depends on the geometry of the sample. As an example for thin films $N_x = N_y = 0, N_z = 1$ and the shape anisotropy energy is simply

$$E_{\text{shape}}^{\text{film}} = \frac{1}{2} V M_s^2 \cos^2\theta. \tag{1.33}$$

For a multilayer the generalization of Eq. (1.32) can be found in Ref. [160]. Using either ferromagnetic resonance (FMR) techniques or by torque measurement, shape anisotropy can be measured experimentally [138, 139, 140, 141].

For Fe films less than five monolayers the anisotropy due to spin-orbit coupling wins – thus the magnetization prefers to be perpendicular to the plane. For more

than five monolayers the shape anisotropy wins – thus the magnetization prefers to be in-plane. Experimentally the measurement of the thickness of the thin film where this reorientation transition takes place depends on the preparation of the sample. Theoretically better numerical techniques are required to explain the experimental results.

Landau and Lifshitz [171] suggested the possibility that a crystal placed in an applied electric field may experience a magnetization which is proportional to the electric field. This magnetoelectric effect was first observed experimentally by Astrov in a monocrystal of antiferromagnetic Cr_2O_3 [172]. It was also observed by Rado et al. that in spin-ordered materials such as Fe_3O_4 the induced electric polarization is proportional to the applied magnetic field [173, 174]. The latter effect is known as magnetically induced magnetoelectric effect $[(ME)_H]$ and the former is known as electrically induced magnetoelectric effect $[(ME)_E]$. To linear order what this means is that the magnetization of the crystal is given by

$$M_i = \alpha_{ij} E_j^{\text{ext}} + \chi_{ij} H_j^{\text{ext}}, \tag{1.34}$$

and the polarization by

$$P_i = \alpha_{ij} E_j^{\text{ext}} + \beta_{ij} H_j^{\text{ext}}, \tag{1.35}$$

where $\mathbf{E}^{\text{ext}}$ and $\mathbf{H}^{\text{ext}}$ are the applied external electric and magnetic fields and α, β, χ are the proportionality constants (summation over j is implied). Fig. 1.15 shows the result of the experiment on magnetite crystals by Rado et al. [174]

Simple phenomenological theory [173, 174] as well as microscopic theory [175] based on perturbation have been proposed to explain the magnetoelectric phe-

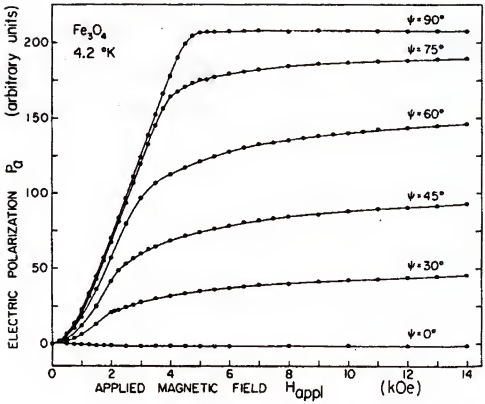

Figure 1.15: Experimental dependence of the polarization P on applied magnetic field for different values of the angle (ψ) between the applied magnetic field and the easy axis [174].

nomenon in spin-ordered materials. The microscopic origin of this magnetoelectric effect lies in the spin-orbit coupling term. We can think of the spatial part of the wave-function as being distorted by the applied electric field. Due to the spin-orbit coupling the spins are affected by this distortion and hence they give rise to an induced magnetization. In other words, the electric field affects the atoms near the surface - thus the surface anisotropy changes which again changes the total energy and the magnetization of the system.

Current-driven excitation of magnetic multilayers also have been studied in recent years [176, 177, 178]. It has been shown theoretically that magnetization of a multilayer can be changed by applying a spin-polarized current. Is it possible to reverse the magnetization of a thin magnetic film by applying a reasonable electric field? How does the surface magnetization change with the electric field? Chapter 4 addresses the above questions.

Finally, Chapter 5 will briefly review the conclusions of the previous chapters and provide suggestions for future work.

CHAPTER 2
GIANT MAGNETORESISTANCE (GMR) IN LATERALLY CONFINED MAGNETIC MULTILAYERS

The importance of studying the transport properties in magnetic multilayers was discussed in Section 1.1 of Chapter 1. The discussion was primarily focussed on the new phenomenon known as the giant magnetoresistance (GMR). Various experimental results and different theoretical models were also briefly outlined. In this chapter we focus on GMR in laterally confined magnetic multilayers. In spite of different existing models – classical or quantum [17, 179] the semiclassical model of Fuchs and Sondheimer [21, 22] is quite successful in predicting the qualitative features of GMR. Moreover, one of the strength of using the Boltzmann equation is to get simple explanations of more complex results. Thus we will use the semiclassical theory for our calculations on laterally confined multilayers in the current-in-plane (CIP) geometry. The organization of this chapter is pedagogical. We start with the semi-classical Fuchs-Sondheimer's derivation of conductivity for a thin film. We then generalize the thin-film result to magnetic multilayers. Dependencies of GMR on different parameters are studied. The derivation for a single wire follows next. To study the effect of lateral confinement we compare the conductivity with that of a film. Finally we generalize the single-wire to laterally confined magnetic multilayers. The effect of lateral confinement on GMR is studied in detail. All our results are then summarized in the conclusion.

2.1 Semi-Classical Fuchs-Sondheimer's Theory for Thin Films

Fuchs-Sondheimer theory [22] for thin films is based on the classical steady-state Boltzmann transport equation:

$$\mathbf{v} \cdot \nabla_{\mathbf{r}} f(\mathbf{v}, \mathbf{r}) - \frac{e}{m} \mathbf{E} \cdot \nabla_{\mathbf{v}} f(\mathbf{v}, \mathbf{r}) = \left(\frac{\partial f(\mathbf{v}, \mathbf{r})}{\partial t} \right)_{\text{scatt}}, \tag{2.1}$$

where $f(\mathbf{v}, \mathbf{r})$ is the distribution function for electrons of mass m at position $\mathbf{r}$ with velocity $\mathbf{v}$ in presence of the electric field $\mathbf{E}$. Because of the scattering term, Eq. (2.1) is complicated. For simplicity we consider the case where the scattering term is

$$\left(\frac{\partial f(\mathbf{v}, \mathbf{r})}{\partial t} \right)_{\text{scatt}} = -\frac{f(\mathbf{v}, \mathbf{r}) - \langle f(\mathbf{v}, \mathbf{r}) \rangle}{\tau}, \tag{2.2}$$

with $\langle f(\mathbf{v}, \mathbf{r}) \rangle$ being the spherical average of the distribution function, and τ is the relaxation time. This is the simplest scattering term to represent elastic scattering. To solve Eq. (2.1) with the right hand side of Eq. (2.2), we define $g(\mathbf{v}, \mathbf{r})$ to be the deviation of the distribution function from its equilibrium value:

$$f(\mathbf{v}, \mathbf{r}) = f_{\text{eq}}(|\mathbf{v}|) + g(\mathbf{v}, \mathbf{r}). \tag{2.3}$$

We next make the ansatz that within linear response the spherical average of the distribution function is equal to the equilibrium distribution function, $\langle f(\mathbf{v}, \mathbf{r}) \rangle = f_{\text{eq}}(|\mathbf{v}|)$, i.e., the spherical average of $g(\mathbf{v}, \mathbf{r})$ is zero. This ansatz will be tested later. This approximation leads to a form known as the relaxation time approximation.

The linearized Boltzmann equation then reduces to

$$\mathbf{v} \cdot \nabla_{\mathbf{r}} g(\mathbf{v}, \mathbf{r}) - \frac{e}{m} \mathbf{E} \cdot \nabla_{\mathbf{v}} f_{\mathrm{eq}}(|\mathbf{v}|) = -\frac{g(\mathbf{v}, \mathbf{r})}{\tau}. \tag{2.4}$$

We now consider the case of a metallic thin film of thickness d as shown in Fig. 2.1. The z-axis is perpendicular to the plane of the film and the current is along the x direction. In this geometry Eq. (2.4) simplifies to:

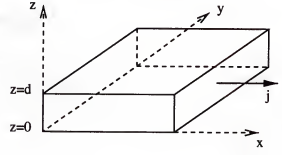

Figure 2.1: Thin film geometry. Current is along the x direction.

$$v_z \frac{\partial g(\mathbf{v}, z)}{\partial z} + e E v_x \left(-\frac{\partial f_{\mathrm{eq}}}{\partial \epsilon_v} \right) = -\frac{g(\mathbf{v}, z)}{\tau}. \tag{2.5}$$

The general solution of Eq. (2.5) is

$$g(\mathbf{v}, z) = -e\tau v_x E \left(-\frac{\partial f_{\mathrm{eq}}}{\partial \epsilon_v} \right) + F(\mathbf{v}) \exp\left(-\frac{z}{\tau v_z} \right), \tag{2.6}$$

where the energy, $\epsilon_v = mv^2/2$. $F(\mathbf{v})$ is an arbitrary function of $\mathbf{v}$ to be determined from the boundary conditions. At each surface ($z = 0$ and $z = d$) the electrons scatter either specularly or diffusively. We assume that a fraction S of the electrons is scattered elastically at the surfaces and the rest $(1 - S)$ is scattered diffusively.

$S = 0$ corresponds to complete diffusive scattering whereas $S = 1$ is for perfectly specular scattering. In general, the specularity factor S can depend on the direction of the electrons but here for simplicity we take it to be a constant. Depending on the directions there are two distribution functions g^+ for electrons moving away from the surface (with $v_z > 0$) and g^- for electrons coming into the surface (with $v_z < 0$). The boundary conditions at the $z = 0$ surface are

$$g^+(\mathbf{v}, z = 0+) = Sg^-(\mathbf{v}, z = 0-) + C_1, \tag{2.7}$$

$$g^-(\mathbf{v}, z = d-) = Sg^+(\mathbf{v}, z = d+) + C_2, \tag{2.8}$$

where C_1, C_2 are due to diffusive scattering at the surfaces and they are independent of the direction of the velocities of the electrons. For convenience we define,

$$g^0(v) = -eEv_z\tau\left(-\frac{\partial f_{\text{eq}}}{\partial \epsilon_v}\right). \quad (v = |\mathbf{v}|) \tag{2.9}$$

Combining Eq. (2.6) with Eq. (2.9) the boundary conditions in Eq. (2.7) and Eq. (2.8) can be expressed as

$$g^0(v) + F^+ = S\left\{g^0(v) + F^-\right\} + C_1, \tag{2.10}$$

$$g^0(v) + F^- \exp\left(\frac{d}{\tau|v_z|}\right) = S\left\{g^0(v) + F^+ \exp\left(-\frac{d}{\tau|v_z|}\right)\right\} + C_2. \tag{2.11}$$

From Eqs. (2.10) and (2.11) F^+ and F^- can be written in terms of C_1 and C_2. Again at each surface current-in is equal to current-out in the z-direction. This gives two more equations to solve for C_1 and C_2. The average of g^0 is zero because it is odd under $v_z \leftrightarrow -v_z$. The equations for C_1 and C_2 are homogeneous and the

only solution is $C_1 = C_2 = 0$. The distribution functions then are:

$$\begin{aligned} g^+(\mathbf{v},z) &= -e\tau E v_x \left(-\frac{\partial f_{\rm eq}}{\partial \epsilon_v}\right) \\ &\times \left\{1 - \frac{1-S}{1-S\exp(-d/\tau|v_z|)} \exp\left(-\frac{z}{\tau|v_z|}\right)\right\}, \qquad (2.12) \\ g^-(\mathbf{v},z) &= -e\tau E v_x \left(-\frac{\partial f_{\rm eq}}{\partial \epsilon_v}\right) \\ &\times \left\{1 - \frac{1-S}{1-S\exp(d/\tau|v_z|)} \exp\left(-\frac{d-z}{\tau|v_z|}\right)\right\}. \qquad (2.13) \end{aligned}$$

By explicitly doing the spherical average of the above distribution functions we find that $< g^+(\mathbf{v},z) >= 0$ and $< g^-(\mathbf{v},z) >= 0$. Thus our ansatz is verified.

The current density along the direction of the electric field is given by

$$\mathcal{J}_x(z) = -2e\left(\frac{m}{h}\right)^3 \int d^3\mathbf{v} v_x g(\mathbf{v},z). \qquad (2.14)$$

The factor of two accounts for the spin-degeneracy. The conductivity σ per unit area is obtained by averaging the current density

$$\sigma = \frac{1}{E}\int dz \mathcal{J}_x(z). \qquad (2.15)$$

Restoring to polar coordinates:

$$\begin{aligned} v_z &= v\cos\theta, \quad v_x = v\sin\theta\cos\phi, \quad v_y = v\sin\theta\sin\phi, \\ d^3\mathbf{v} &= v^2 dv \sin\theta d\theta d\phi, \end{aligned}$$

the ratio of the conductivity of the film to that of the bulk metal can be derived. The result is

$$\begin{aligned}\frac{\sigma_{\text{film}}}{\sigma_{\text{bulk}}} &= \left\{1-\frac{3L}{2d}(1-S)\right. \\ &\times \left.\int_0^1 d(\cos\theta)\cos\theta\sin^2\theta\frac{1-\exp(-d/L|\cos\theta|)}{[1-S\exp(-d/L|\cos\theta|)]}\right\}, \end{aligned} \tag{2.16}$$

where L is the mean free path of the electrons and the bulk conductivity is defined to be

$$\sigma_{\text{bulk}} = \left(\frac{ne^2L}{mv_F}\right). \tag{2.17}$$

For perfectly diffusive scattering at the surfaces (S=0), Eq. (2.16) takes an analytical form in terms of the exponential integral function $E_1(d/L)$ [180]

$$\begin{aligned}\frac{\sigma_{\text{film}}}{\sigma_{\text{bulk}}} &= \left\{1-\frac{3L}{2d}+\left(\frac{5}{8}-\frac{3L}{8d}+\frac{d}{16L}-\frac{d^2}{L^2}\right)\exp\left(-\frac{d}{L}\right)\right. \\ &+ \left.\left(\frac{d^3}{16L^3}-\frac{3d}{4L}\right)E_1\left(\frac{d}{L}\right)\right\}. \end{aligned} \tag{2.18}$$

Limiting values for thick films and very thin films can now be obtained from Eq. (2.16). For large d/L (thick films)

$$\frac{\sigma_{\text{film}}}{\sigma_{\text{bulk}}} = 1-\frac{3L(1-S)}{8d}, \tag{2.19}$$

and for thin films ($d/L << 1$) we get

$$\frac{\sigma_{\text{film}}}{\sigma_{\text{bulk}}} = \frac{3d}{4L}(1+2S)\left(\log\frac{L}{d}+0.423\right). \tag{2.20}$$

In the limit $d/L >> 1$ [Eq. (2.19)] there are two contributions to the scattering rate – one due to the background scattering and the other due to surface scattering. On the other hand, in the limit $d/L << 1$ [Eq. (2.20)] the conductivity diverges (the resistivity goes to zero) for fixed d when the background scattering vanishes (i.e. $L \to \infty$). This is puzzling as one would expect a finite residual resistivity due to the surface scattering. In quantum mechanical models, this divergence of the conductivity for large mean free path disappears and the resistivity remains finite for finite thickness. This has been explained in Section 1.1 of Chapter 1. In Fig. 2.2 we plot the ratio of the conductivity of a film to that of the bulk

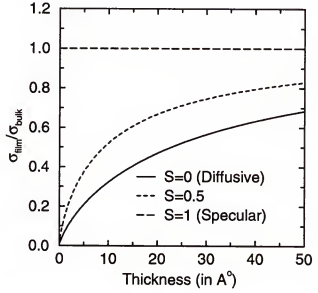

Figure 2.2: The ratio of conductivity of a thin film (σ_{film}) to that of the bulk conductivity (σ_{bulk}) as a function of the thickness of the film. The mean free path of the electrons is taken to be 50 Å. For specular scattering there is no change in the conductivity where as for diffusive scattering conductivity increases with thickness and finally saturates to the bulk value.

conductivity for three different values of the specularity factors. For specular scattering ($S = 1$) there is no change in the conductivity as a function of thickness and the conductivity is equal to the bulk value. But for diffusive scattering at the surfaces conductivity increases with thickness and finally saturates to the bulk value.

2.2 Generalization to Magnetic Multilayers

Calculation of the conductivity and the giant magnetoresistance (GMR) of a magnetic multilayer structure is due to Camley and Barnaś [23, 24]. Their theory is the generalization of Fuchs-Sondheimer theory for thin films. The Boltzmann equation [Eq. (2.1)] is same as before with the only difference that the distribution functions and the parameters carry an extra index n for the layers. A N layer system which is alternating layers of ferromagnets (FM) and paramagnets (PM) is shown schematically in Fig. 2.3. The general solution for the distribution function is thus

$$g_n(\mathbf{v}, z) = -ev_z\tau_n E\left(-\frac{\partial f_{\mathrm{eq}}}{\partial \epsilon_v}\right) + F_n(\mathbf{v}) \exp\left(-\frac{z}{\tau_n v_z}\right). \tag{2.21}$$

The functional form of $F_n(\mathbf{v})$ is determined from the boundary conditions. We proceed in the same fashion as we did for the film. Let $g_n^+(\mathbf{v}, z)$ and $g_n^-(\mathbf{v}, z)$ be the distribution functions of the electrons with $v_z > 0$ and with $v_z < 0$ respectively. At each interface the electrons undergo specular or diffuse scattering. For specular scattering, the reflection and transmission coefficients enter into the boundary

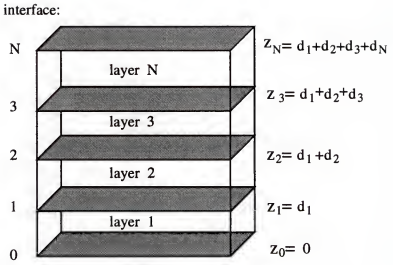

Figure 2.3: Schematic diagram of a N-layer system. Thickness of the n-th layer is d_n.

conditions. The boundary conditions at the nth interface are

$$g_n^+\left(\mathbf{v}, z_n^+\right) = S_n T_n g_{n-1}^+\left(\mathbf{v}, z_n^-\right) + S_n R_n g_n^-\left(\mathbf{v}, z_n^+\right) + C_n, \qquad (2.22)$$

$$g_{n-1}^-\left(\mathbf{v}, z_n^-\right) = S_n T_n g_n^-\left(\mathbf{v}, z_n^+\right) + S_n R_n g_{n-1}^+\left(\mathbf{v}, z_n^-\right) + C_n, \qquad (2.23)$$

where R_n and T_n are reflection and transmission coefficients at the nth interface, and S_n is the specularity factor. C_n is a constant due to the diffuse scattering at the interface. At each interface the sum of the reflection and transmission coefficients is unity, i.e. $R_n + T_n = 1$. We have assumed T, R, and C depend only on the interface - not on how the electrons enter or exit the interface. Also to mention that the transmission coefficient is zero (thus $R = 1$) for the first ($n = 0$) and the last surface ($n = N$).

We now combine the boundary conditions in Eqs. (2.22), (2.23), and the solution of the Boltzmann equation [Eq. (2.21)] within each layer. For convenience we choose the following convention:

$$g_n^+(\mathbf{v},z) = g_n^0(v) + F_n^+(\mathbf{v})\exp\left(-\frac{z-z_{n-1}}{|v_z|\tau_n}\right), \tag{2.24}$$

$$g_n^-(\mathbf{v},z) = g_n^0(v) + F_n^-(\mathbf{v})\exp\left(-\frac{z_n-z}{|v_z|\tau_n}\right), \tag{2.25}$$

where we have introduced the simplifying notation:

$$g_n^0(v) = -eEv_z\tau_n\left(-\frac{\partial f_{\text{eq}}}{\partial\epsilon_v}\right). \qquad (v=|\mathbf{v}|) \tag{2.26}$$

This allows us to express the boundary conditions solely in terms of the F's and C's:

$$g_n^+\left(\mathbf{v},z_n^+\right) = g_n^0(v) + F_n^+(\mathbf{v}), \tag{2.27}$$

$$g_{n-1}^+\left(\mathbf{v},z_n^-\right) = g_n^0(v) + F_{n-1}^+(\mathbf{v})\exp\left(-\frac{d_{n-1}}{|v_z|\tau_{n-1}}\right), \tag{2.28}$$

$$g_n^-\left(\mathbf{v},z_n^+\right) = g_n^0(v) + F_n^-(\mathbf{v})\exp\left(-\frac{d_n}{|v_z|\tau_n}\right), \tag{2.29}$$

$$g_{n-1}^-\left(\mathbf{v},z_n^-\right) = g_n^0(v) + F_{n-1}^-(\mathbf{v}). \tag{2.30}$$

Substituting Eqs. (2.27) and (2.30) in Eqs. (2.22) and (2.23) yields:

$$\begin{aligned} S_nT_ng_{n-1}^0(v) - (1-S_nR_n)g_n^0(v) - C_n &= F_n^+(\mathbf{v}) \\ &\quad - S_nT_nF_{n-1}^+(\mathbf{v})\exp\left(-\frac{d_{n-1}}{|v_z|\tau_{n-1}}\right) \end{aligned}$$

$$- \; S_n R_n F_n^- (\mathbf{v}) \exp\left(-\frac{d_n}{|v_z|\tau_n}\right), \quad (2.31)$$

$$\begin{aligned} S_n T_n g_n^0(v) - (1 - S_n R_n) g_{n-1}^0(v) - C_n &= F_{n-1}^+ (\mathbf{v}) \\ &- S_n R_n F_{n-1}^+ (\mathbf{v}) \exp\left(-\frac{d_{n-1}}{|v_z|\tau_{n-1}}\right) \\ &- S_n T_n F_n^- (\mathbf{v}) \exp\left(-\frac{d_n}{|v_z|\tau_n}\right). \end{aligned} \quad (2.32)$$

There are $2N$ of these equations – one for each $F^{\pm}$. We go through them sequentially and eliminate the $F^{\pm}$ one at a time. At each step, we move terms to the left-hand-side containing g^0 and the C's. These terms may be multiplied by one or more of the exponential functions with $|v_z|$. On the right-hand-side are terms which are linear in the $F^{\pm}$. They also may be multiplied by one or more of the exponential functions with $|v_z|$. This means that the final $F^{\pm}$ and each of the others have the form

$$F^{\pm} = \frac{\sum (g^{0\prime}\text{s}) \times (\exp\text{'s}) + \sum (C\text{'s}) \times (\exp\text{'s})}{\sum (\exp\text{'s})}. \quad (2.33)$$

This still leaves $N + 1$ number of C's. The remaining $N + 1$ equations are that the current-in is equal to the current-out in the z-direction at each interface. The average of the g^0's is zero because they are odd under $v_x \leftrightarrow -v_x$. The equations for the C's are homogeneous, and baring any special coincidence, the only solution is that all the C's are zero.

The $2N$ equations we must now solve are:

$$S_n T_n g_{n-1}^0(v) - (1 - S_n R_n) g_n^0(v) = F_n^+ (\mathbf{v}) - S_n T_n F_{n-1}^+ (\mathbf{v}) \exp\left(-\frac{d_{n-1}}{|v_z|\tau_{n-1}}\right)$$

$$- \; S_n R_n F_n^- (\mathbf{v}) \exp\left(-\frac{d_n}{|v_z|\tau_n}\right), \tag{2.34}$$

$$\begin{aligned} S_n T_n g_n^0(v) - (1 - S_n R_n) g_{n-1}^0(v) &= F_{n-1}^+ (\mathbf{v}) - S_n T_n F_n^- (\mathbf{v}) \exp\left(-\frac{d_n}{|v_z|\tau_n}\right) \\ &- S_n R_n F_{n-1}^+ (\mathbf{v}) \exp\left(-\frac{d_{n-1}}{|v_z|\tau_{n-1}}\right). \end{aligned} \tag{2.35}$$

We now simplify the above equations. Each of the g^0's on the left-hand-side has the common factor $-eEv_x(-\partial f_{\text{eq}}/\partial\epsilon_v)$ which we can divide out. Defining

$$F(\mathbf{v}) = -eE\hat{v}_x \left(-\frac{\partial f_{\text{eq}}}{\partial \epsilon_v}\right) \bar{F}(\mathbf{v}), \tag{2.36}$$

Eqs. (2.34) and (2.35) now read

$$\begin{aligned} S_n T_n l_{n-1} - (1 - S_n R_n) l_n &= \bar{F}_n^+ (\mathbf{v}) - S_n T_n \bar{F}_{n-1}^+ (\mathbf{v}) \exp\left(-\frac{d_{n-1}}{|v_z|\tau_{n-1}}\right) \\ &- S_n R_n \bar{F}_n^- (\mathbf{v}) \exp\left(-\frac{d_n}{|v_z|\tau_n}\right), \end{aligned} \tag{2.37}$$

$$\begin{aligned} S_n T_n l_n - (1 - S_n R_n) l_{n-1} &= \bar{F}_{n-1}^+ (\mathbf{v}) - S_n T_n \bar{F}_n^- (\mathbf{v}) \exp\left(-\frac{d_n}{|v_z|\tau_n}\right) \\ &- S_n R_n \bar{F}_{n-1}^+ (\mathbf{v}) \exp\left(-\frac{d_{n-1}}{|v_z|\tau_{n-1}}\right), \end{aligned} \tag{2.38}$$

where $l_n = v_F \tau_n$ is the mean free path in the nth layer. The angular dependence in these equations only comes in through $|v_z|$. Letting $u = |\cos\theta|$, we get

$$\begin{aligned} S_n T_n l_{n-1} - (1 - S_n R_n) l_n &= \bar{F}_n^+(u) - S_n T_n \bar{F}_{n-1}^+(u) \exp\left(-\frac{d_{n-1}}{l_{n-1} u}\right) \\ &- S_n R_n \bar{F}_n^-(u) \exp\left(-\frac{d_n}{l_n u}\right), \end{aligned} \tag{2.39}$$

$$S_n T_n l_n - (1 - S_n R_n) l_{n-1} = \bar{F}_{n-1}^+(u) - S_n T_n \bar{F}_n^-(u) \exp\left(-\frac{d_n}{l_n u}\right)$$

$$- \quad S_n R_n \bar{F}^{+}_{n-1}(u) \exp\left(-\frac{d_{n-1}}{l_{n-1}u}\right). \tag{2.40}$$

The above equations have to solved for u between zero and one.

Averaging the current over the z-direction the conductivity can be expressed as

$$\begin{aligned}\sigma &= \frac{1}{E}\int dz \mathcal{J}_x(z) = N(E_F)e^2 v_F \sum_{n=1}^{N} d_n \frac{l_n}{3} \\ &+ N(E_F)e^2 v_F \sum_{n=1}^{N} \int_0^1 \frac{du}{2}\frac{1}{2}\left(1-u^2\right) l_n u \left\{1 - \exp\left(-\frac{d_n}{l_n u}\right)\right\} \\ &\times \left\{\bar{F}^{+}_{n}(u) + \bar{F}^{-}_{n}(u)\right\}. \end{aligned} \tag{2.41}$$

where $N(E_F)$ is the density of states at the Fermi surface. For this multi-layer geometry we compute the conductivity in two cases: when the ferromagnet's magnetizations are parallel, σ_F, and when they are antiparallel, σ_{AF}. The magnetoresistance is defined as the ratio of the change in the conductivity from parallel to antiparallel alignments divided by the parallel conductivity:

$$\mathrm{GMR} = 1 - \frac{\sigma_{\mathrm{AF}}}{\sigma_{\mathrm{F}}}. \tag{2.42}$$

In Fig. 2.4 we plot the giant magnetoresistance of a three-layer structure as a function of thickness of the spacer layer for three cases: (a) GMR due to bulk scattering, (b) GMR due to surface scattering, and (c) GMR due to both bulk and surface scattering. For bulk scattering [case (a)] the GMR decreases monotonically whereas for surface scattering [case (b)] the GMR initially increases and then decreases with the thickness of the spacer layer. This can be understood from the

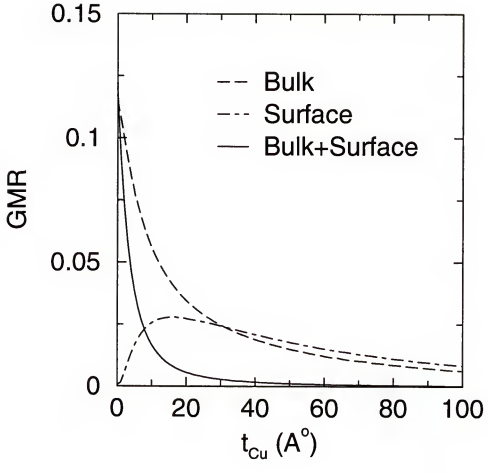

Figure 2.4: GMR of a three-layer structure (Co/Cu/Co) as a function of the thickness of the Cu layer (t_{Cu}) for (a) bulk scattering, (b) surface scattering, and (c) both bulk and surface scattering. The thickness of the Co layers are kept fixed at 8 Å. For cases (a) and (c) the mean free paths are chosen to be that of Co/Cu/Co, $L^{\uparrow} = 55$ Å, $L^{\downarrow} = 10$ Å, and $L^{\mathrm{PM}} = 226$ Å [181]. For case (b) in which the surface scattering contributes to the GMR we use $L^{\uparrow} = L^{\downarrow} = 17$ Å and $L^{\mathrm{PM}} = 226$ Å. For cases (b) and (c) the transmission coefficients are taken to be $T^{\uparrow} = 0.8$, $T^{\downarrow} = 0.4$ [182]. In case of (a) which is for the bulk scattering we take $T^{\uparrow} = T^{\downarrow} = 0.6$. We choose the interfaces to have the same specularity factor $S = 0.9$.

classical model we derived in Chapter 1. Following Eq. (1.10) we see that for bulk scattering in the limit of zero thickness of the spacer layer the GMR is finite and is equal to the GMR obtained from Eq. (1.5). The decrease in GMR with increase in thickness of the spacer layer also follows from Eq. (1.10). The maximum value of the GMR for case (a) primarily depends on the mean free paths of the ferromagnet. The general case of both bulk and surface scattering [case (c)] is a combination of case (a) and case (b). The decrease of GMR with the thickness of the spacer layer is in agreement qualitatively with the experimental results [9, 10, 11].

GMR as a function of thickness of the ferromagnet for the same cases as in Fig. 2.4 is plotted in Fig. 2.5. In all cases GMR initially increases and then decreases with increase in the thickness of the ferromagnetic layers. Also note that the contribution to GMR due to bulk scattering is more than the contribution from the interface scattering.

The effect of the surface roughness (S) on the GMR is shown in Fig. 2.6. With entirely diffusive ($S = 0$) surfaces and interfaces the multilayers are independent of each other which means that there is no GMR. With a decrease in the interface roughness, the GMR increases and finally reaches a maximum for perfectly specular surfaces.

2.3 Thin wires – Theory and Results

In the case of thin wires the problem is two-dimensional and the Boltzmann equation takes the form of a partial differential equation in the space variables [183]. With completely diffusive surfaces results for wires with square cross-section were obtained by MacDonald and Sarginson [184] and for wires with circular cross-

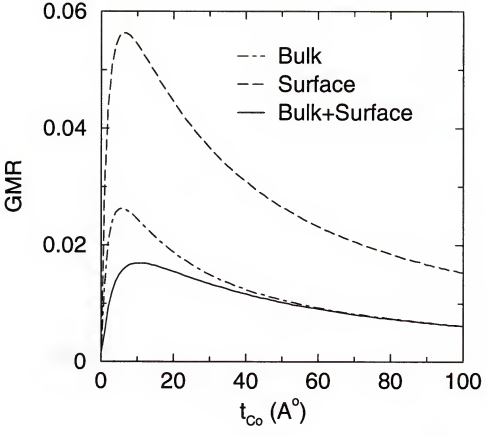

Figure 2.5: GMR of a three-layer structure (Co/Cu/Co) as a function of the thickness of the Co layer (t_{Co}) for (a) bulk scattering, (b) surface scattering, and (c) both bulk and surface scattering. The thickness of the Cu layer is kept fixed at 10 Å. In all cases GMR initially increases and then decreases with increase in the thickness of the ferromagnet. Note that GMR due to bulk scattering is more than the surface scattering. The parameters chosen are the same as in Fig. 2.4.

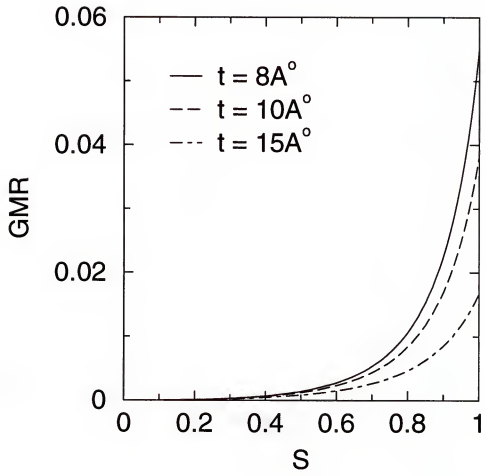

Figure 2.6: GMR is plotted as a function of the specularity factor for different thicknesses (t) of the layers. GMR increases with decrease in the interface roughness. For convenience the thickness of the Co and Cu layers is taken to be the same. We use the same parameters as in Fig. 2.4.

section by Dingle [185]. In this section we first present analytical results for the conductivity of a thin wire with rectangular cross-section but with diffusive surfaces. We then generalize to wires with specular and diffusive surfaces. In the latter case we solve for the conductivity numerically using an iterative procedure.

We consider a wire of width w and thickness t. For convenience, the electric field is taken to be along the z direction. Similar to Eq. (2.5) the Boltzmann equation in this geometry under the relaxation time approximation reads

$$v_x \frac{\partial g(\mathbf{v},x,y)}{\partial x} + v_y \frac{\partial g(\mathbf{v},x,y)}{\partial y} + \frac{g(\mathbf{v},x,y)}{\tau} = -eEv_z \left(-\frac{\partial f_{\rm eq}}{\partial \epsilon_v}\right). \tag{2.43}$$

The general solution of Eq. (2.43) can be written as

$$g(\mathbf{v},x,y) = -eEv_z \left(-\frac{\partial f_{\rm eq}}{\partial \epsilon_v}\right) \left[1 - \exp\left(-\frac{x}{\tau v_x}\right) \Psi\left(\frac{y}{v_y} - \frac{x}{v_x}\right)\right], \tag{2.44}$$

or equally well,

$$g(\mathbf{v},x,y) = -eEv_z \left(-\frac{\partial f_{\rm eq}}{\partial \epsilon_v}\right) \left[1 - \exp\left(-\frac{y}{\tau v_y}\right) \Phi\left(\frac{x}{v_x} - \frac{y}{v_y}\right)\right]. \tag{2.45}$$

The functions Ψ and Φ are arbitrary and have to be determined from the boundary conditions. We assume scattering is completely diffusive at the boundaries - so the distribution function g of the electrons leaving the boundaries must be independent of the ratio $v_x : v_y : v_z$ at $x = 0, w$; and $y = 0, t$. Specifically g is equal to zero under these conditions. The complete distribution function can be represented by the following set of equations in velocity space:

First quadrant: $v_x > 0, v_y > 0,$

$$g\left(v_x > 0, v_y > 0, x, y < \frac{v_y}{v_x}x\right) = -eEv_z\left(-\frac{\partial f_{\rm eq}}{\partial \epsilon_v}\right) \times \left[1 - \exp\left(-\frac{y}{\tau v_y}\right)\right], \quad (2.46)$$

$$g\left(v_x > 0, v_y > 0, x, y > \frac{v_y}{v_x}x\right) = -eEv_z\left(-\frac{\partial f_{\rm eq}}{\partial \epsilon_v}\right) \times \left[1 - \exp\left(-\frac{x}{\tau v_x}\right)\right]. \quad (2.47)$$

Second quadrant: $v_x > 0, v_y < 0,$

$$g\left(v_x > 0, v_y < 0, x < -\frac{v_x}{v_y}(t-y), y\right) = -eEv_z\left(-\frac{\partial f_{\rm eq}}{\partial \epsilon_v}\right) \times \left[1 - \exp\left(-\frac{x}{\tau v_x}\right)\right], \quad (2.48)$$

$$g\left(v_x > 0, v_y < 0, x > -\frac{v_x}{v_y}(t-y), y\right) = -eEv_z\left(-\frac{\partial f_{\rm eq}}{\partial \epsilon_v}\right) \times \left[1 - \exp\left(\frac{t-y}{\tau v_y}\right)\right]. \quad (2.49)$$

Third quadrant: $v_x < 0, v_y < 0,$

$$g\left(v_x < 0, v_y < 0, (w-x) < \frac{v_x}{v_y}(t-y), y\right) = -eEv_z\left(-\frac{\partial f_{\rm eq}}{\partial \epsilon_v}\right) \times \left[1 - \exp\left(\frac{w-x}{\tau v_x}\right)\right], \quad (2.50)$$

$$g\left(v_x < 0, v_y < 0, (w-x) > \frac{v_x}{v_y}(t-y), y\right) = -eEv_z\left(-\frac{\partial f_{\rm eq}}{\partial \epsilon_v}\right) \times \left[1 - \exp\left(\frac{t-y}{\tau v_y}\right)\right]. \quad (2.51)$$

Fourth quadrant: $v_x < 0, v_y > 0,$

$$g\left(v_x<0,v_y>0,x,y<-\frac{v_y}{v_x}(w-x)\right) = -eEv_z\left(-\frac{\partial f_{\rm eq}}{\partial \epsilon_v}\right) \times \left[1-\exp\left(-\frac{y}{\tau v_y}\right)\right], \quad (2.52)$$

$$g\left(v_x<0,v_y>0,x,y>-\frac{v_y}{v_x}(w-x)\right) = -eEv_z\left(-\frac{\partial f_{\rm eq}}{\partial \epsilon_v}\right) \times \left[1-\exp\left(\frac{w-x}{\tau v_x}\right)\right]. \quad (2.53)$$

Due to symmetry each quadrant contributes equally to the total current $\mathcal{J}_z$. Using Eq. (2.15) and Eqs. (2.46 - 2.53) the conductivity is calculated and the result is,

$$\begin{aligned}\frac{\sigma_{\rm wire}}{\sigma_{\rm film}} &= \left\{L-\left(\frac{3}{8}\right)\left(\frac{L^2}{w}+\frac{L^2}{t}\right)+\left(\frac{4}{5\pi}\right)\left(\frac{L^3}{wt}\right)\right. \\ &= \left(\frac{6L^2}{\pi w}\right)\int_0^{\pi/2}d\theta\sin^2\theta\cos^2\theta\int_0^{\tan^{-1}(t/w)}d\phi\cos\phi e^{-w/L\sin\theta\cos\phi} \\ &+ \left(\frac{6L^2}{\pi t}\right)\int_0^{\pi/2}d\theta\sin^2\theta\cos^2\theta\int_0^{\tan^{-1}(w/t)}d\phi\cos\phi e^{-t/L\sin\theta\cos\phi} \\ &+ \left(\frac{6L^3}{\pi wt}\right)\int_0^{\pi/2}d\theta\sin^3\theta\cos^2\theta\left[e^{-\sqrt{(w^2+t^2)}/L\sin\theta}-e^{-w/L\sin\theta}\right] \\ &- \left.\left(\frac{6L^3}{\pi wt}\right)\int_0^{\pi/2}d\theta\sin^3\theta\cos^2\theta e^{-t/L\sin\theta}\right\}. \end{aligned} \quad (2.54)$$

Different limiting values of Eq. (2.54) can be obtained. In the limit ($L << w, t$) we obtain

$$\frac{\sigma_{\rm wire}}{\sigma_{\rm film}} \approx 1-\left(\frac{3}{8}\right)\left(\frac{L}{w}+\frac{L}{t}\right)+\left(\frac{4}{5\pi}\right)\left(\frac{L^2}{wt}\right)+.... \quad (2.55)$$

In the other limit i.e. $L >> w, t$ we get

$$\begin{aligned}
\frac{\sigma_{\text{wire}}}{\sigma_{\text{film}}} \approx & \left(\frac{3w}{8L}\right)\ln\left(\frac{\sqrt{w^2+t^2}+t}{\sqrt{w^2+t^2}-t}\right)+\left(\frac{3t}{8L}\right)\ln\left(\frac{\sqrt{w^2+t^2}+w}{\sqrt{w^2+t^2}-w}\right) \\
& - \left(\frac{1}{4wtL}\right)\left[\left(w^2+t^2\right)^{3/2}-w^3-t^3\right] \\
& + \left(\frac{3wt}{2\pi L^2}\right)\left(\gamma-\ln 2-\frac{25}{12}\right)+\left(\frac{wt}{\pi L^2}\right)\ln\left(\frac{w^2+t^2}{L^2}\right) \\
& + \left(\frac{1}{\pi L^2}\right)\left[w^2\tan^{-1}\left(\frac{t}{w}\right)+t^2\tan^{-1}\left(\frac{w}{t}\right)\right] \\
& - \left(\frac{1}{4\pi wtL^2}\right)\left[\left(w^2+t^2\right)^2\ln\left(\frac{\sqrt{w^2+t^2}}{L}\right)\right] \\
& + \left(\frac{1}{4\pi wtL^2}\right)\left[w^4\ln\left(\frac{w}{L}\right)+t^4\ln\left(\frac{t}{L}\right)\right]+\ldots, \qquad (2.56)
\end{aligned}$$

where γ is the euler constant.

For the case of a wire with square cross-section ($w = t$), Eqs. (2.55) and (2.56) can be simplified.

$$\frac{\sigma_{\text{wire}}}{\sigma_{\text{film}}} \approx 1-\frac{3L}{4t}+\ldots \quad (L << t) \qquad (2.57)$$

and in the other limit ($L >> t$)

$$\frac{\sigma_{\text{wire}}}{\sigma_{\text{film}}} \approx \frac{3t}{4L}\ln\left(\frac{\sqrt{2}+1}{\sqrt{2}-1}\right)-\frac{t}{2L}\left(\sqrt{2}-1\right)=1.115\frac{t}{L}. \qquad (2.58)$$

Comparing Eq. (2.57) with the results of a thin film with $S = 0$ in Eq. (2.19) and Eq. (2.58) with Eq. (2.20) the much more rapid decrease of the conductivity in the case of a wire is evident. The result for the conductivity of a wire with rectangular cross-section but diffusive surfaces is shown in Fig. 2.7. The ratio of conductivities is compared with that of a thin film.

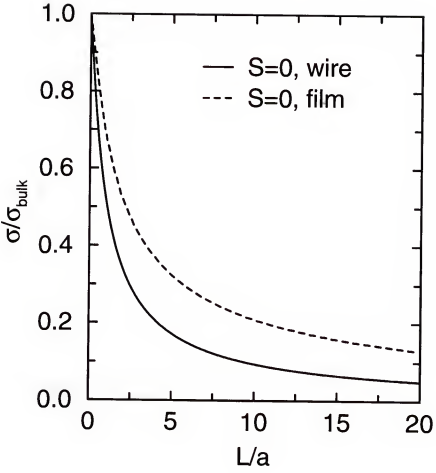

Figure 2.7: Comparison of a thin square wire result with that of a thin film. The ratio of the conductivities ($\sigma/\sigma_{\text{bulk}}$) is plotted as a function of the ratio of the mean free path (L) and the width (a) (thickness in case of the film). Due to lateral confinement $\sigma/\sigma_{\text{bulk}}$ decreases faster in case of wire than that of the film.

We numerically solve the general case, i.e. when scattering at the surfaces is both specular and diffusive. We go back to the linearized Boltzmann equation in Eq. (2.1). When the electric field is zero, Eq. (2.4) becomes a homogeneous equation with the expected solution being $g(\mathbf{v},\mathbf{r}) = 0$. For non-zero electric field, $g(\mathbf{v},\mathbf{r})$ is proportional to $(e\mathbf{E}/m)\nabla_{\mathbf{v}} f_{\mathrm{eq}}(|\mathbf{v}|) = e\mathbf{E}\cdot\mathbf{v}\partial f_{\mathrm{eq}}(|\mathbf{v}|)/\partial\epsilon_v$. Thus, $g(-\mathbf{v},\mathbf{r}) = -g(\mathbf{v},\mathbf{r})$, irrespective of the boundary conditions, and the ansatz that the spherical average of $g(\mathbf{v},\mathbf{r})$ is zero is justified. We write the general solution in a slightly different form than before [186, 187]

$$g(\mathbf{v},\mathbf{r}) \;=\; g(\mathbf{v},\mathbf{r_B})e^{-|\mathbf{r}-\mathbf{r_B}|/\tau|\mathbf{v}|} + e\tau\mathbf{E}\cdot\mathbf{v}\left(\frac{\partial f^{\mathrm{eq}}}{\partial\epsilon_v}\right)\left(1-e^{-|\mathbf{r}-\mathbf{r_B}|/\tau|\mathbf{v}|}\right), \quad (2.59)$$

where $\mathbf{r}_B$ is a point on the boundary. Eq. (2.59) implies that to find the distribution function at position $\mathbf{r}$ with velocity $\mathbf{v}$, we proceed from $\mathbf{r}$ backwards along $\mathbf{v}$ until we reach a point $\mathbf{r}_B$ at the boundary. The distribution function at the boundary, $g(\mathbf{v},\mathbf{r_B})$, is determined by the boundary conditions. We recover the usual bulk value if we go far away from the boundary points. Also we can see from Eq. (2.59) that the electrons lose their momentum as they diffuse into the medium and the characteristic length scale for this is just the mean free path, τv_F, where v_F is the Fermi velocity.

We now examine the boundary conditions. Electrons are scattered either specularly or diffusively at each surface. For a thin wire there are four surfaces. A schematic diagram of a rectangular wire is shown in Fig. 2.8. Let j be an index for the surface. The boundary condition at the j-th surface can be expressed as:

$$g_j^{out}(\mathbf{v},\mathbf{r_j}) = S g_j^{in}(-\mathbf{v},\mathbf{r_j}), \quad (2.60)$$

where $\mathbf{r_j}$ is a point on the j-th surface, and the superscripts out, in correspond to electrons going out from the boundary or coming in to the boundary. We iteratively solve the linear set of equations for the distribution functions, $g^{out}(\mathbf{v}, \mathbf{r_B})$, which are non-uniform along the $\hat{x}$ and $\hat{y}$ directions of the surfaces. From Eq. (2.4) we observe that the $g^{out}(\mathbf{v}, \mathbf{r})$'s with different velocities projected along the $\hat{z}$ direction are decoupled. This allows us to discretize the $g^{out}(\mathbf{v}, \mathbf{r})$ according to $\cos\theta = v_z/|v|$ and solve each separately. For each $\cos\theta$, $g^{out}(\mathbf{v}, \mathbf{r})$ at the surfaces carry two more indices: an angle ϕ and a position $\mathbf{r}_i$. The $g^{out}(\mathbf{v}, \mathbf{r})$'s for different ϕ and $\mathbf{r}_i$ are related via Eq. (2.6) and the boundary conditions given in Eq. (2.60). As an

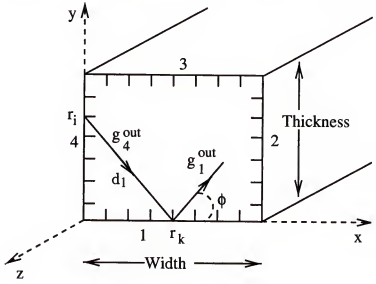

Figure 2.8: Schematic diagram of a thin wire. The four surfaces are labeled as 1, 2, 3, and 4. Current is in plane along the $\hat{z}$ direction. The distribution function for outgoing electrons at point $\mathbf{r}_k$ on surface 1 depend on all possible incoming electrons from points on the other surfaces. As an example the contribution from point $\mathbf{r}_i$ on surface 4 is shown schematically. The precise relationship is described in the text [see Eq. (2.61)].

example the relation between the distribution functions of the outgoing electrons

at a surface 1 is:

$$g_1^{out}(\cos\theta, \phi, \mathbf{r}_k) = S g_4^{out}(\cos\theta, 2\pi - \phi, \mathbf{r}_i) \times e^{-d_1/\tau v_F \sin\theta} \tag{2.61}$$

where d_1 is the path length projected onto the $x-y$ plane from one boundary to another. Initial guesses for $g_j^{out}(\cos\theta, \phi, \mathbf{r}_i)$ are taken from the nearby $g_j^{out}[\cos\theta - \delta(\cos\theta), \phi, \mathbf{r}_i]$. The calculations are converged to within 1%.

Once we know the distribution functions at the boundaries, by using Eqs. (2.3) and (2.6) we can determine the distribution function of the electrons with momentum $\mathbf{v}$ at any point $\mathbf{r}$. The conductivity is then calculated by averaging the current density over an area $\mathcal{A}$:

$$\sigma = \frac{2}{E\mathcal{A}} \int dx dy \mathcal{J}(x, y). \tag{2.62}$$

The factor of two accounts for the spin-degeneracy.

In Fig. 2.9 we plot the ratio of the conductivity of the wire to that of the bulk as a function of the ratio of the mean free path to the width of the wire. Similar to thin films the ratio $\sigma_{\text{wire}}/\sigma_{\text{bulk}}$ decreases with the ratio L/width, where L is the mean free path.

To show the effect of lateral confinement we plot in Fig. 2.10 the ratio of conductivities $\sigma_{\text{wire}}/\sigma_{\text{bulk}}$ as a function of the aspect ratio (width/thickness) for different values of the specularity factor. For perfect specular scattering the ratio is unity. In all other cases the ratio increases with decrease in the aspect ratio. For very large values of the aspect ratio the conductivity of the wire saturates to the bulk conductivity.

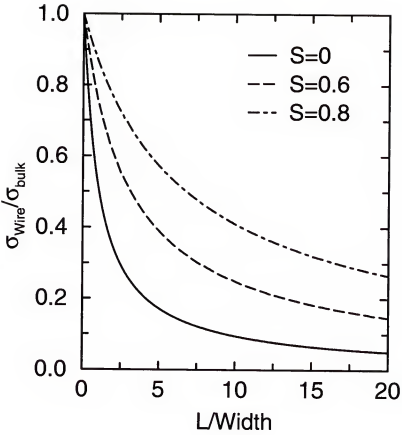

Figure 2.9: Conductivity of a thin wire (σ_{wire}) with respect to the bulk conductivity (σ_{bulk}) is plotted as a function of the ratio of the mean free path (L) and the width of the wire for three different values of the specularity factor (S). The aspect ratio (thickness/width) is kept fixed to unity in all three cases. Similar to thin films the ratio of the conductivities decreases with increase in L/Width.

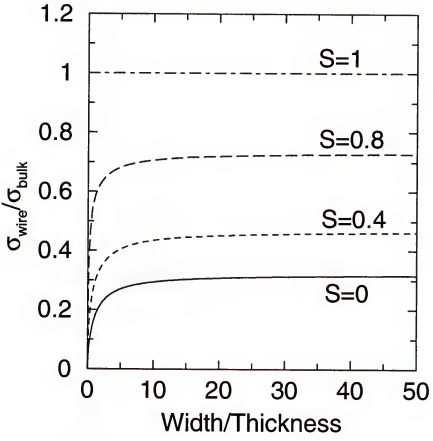

Figure 2.10: $\sigma_{wire}/\sigma_{bulk}$ as a function of the aspect ratio (width/thickness). The ratio of the conductivities increases with increase in the the aspect ratio for different values of the specularity factor S ($S \neq 1$). For $S = 1$ the conductivity of the wire is equal to the bulk conductivity. The thickness is kept fixed to 10 Å in all cases and the mean free path is chosen to be 50 Å.

2.4 Generalization to Laterally Confined Magnetic Multilayers

The geometry of our problem is shown in Fig. 2.11. We compute the current-in-plane conductivity (CIP) for a three-wire structure stacked along the $\hat{y}$-direction. Both the current and the electric field are in the $\hat{z}$ direction. We have two identical ferromagnetic materials (FM) and a paramagnet (PM). For this three wire geometry we compute the conductivity in the case when the ferromagnet's magnetizations are parallel, σ_F, and when they are antiparallel, σ_{AF}. The magnetoresistance is then calculated from Eq. (2.42).

For the laterally confined magnetic multilayers the solution of the Boltzmann equation carries an extra layer index n. The generalized version of Eq. (2.59) reads

$$\begin{aligned} g_{ns}(\mathbf{v},\mathbf{r}) &= g_{ns}(\mathbf{v},\mathbf{r_B})e^{-|\mathbf{r}-\mathbf{r_B}|/\tau_{ns}|\mathbf{v}|} \\ &+ e\tau_{ns}\mathbf{E}\cdot\mathbf{v}\left(\frac{\partial f_{ns}^{eq}}{\partial\epsilon_v}\right)(1-e^{-|\mathbf{r}-\mathbf{r_B}|/\tau_{ns}|\mathbf{v}|}), \end{aligned} \tag{2.63}$$

where $\mathbf{r}_B$ is a point on the boundary or interface and s refers to the spin of the electrons. We now consider the boundary conditions. At each interface the electrons undergo either specular or diffuse scattering. For the nth interface, which is between wires n and $n+1$, we define the probability of spin s electrons being diffusively scattered as $(1-S_{ns})$, where S_{ns} is the spin dependent specularity factor. The probabilities for being specularly reflected and transmitted are $S_{ns}R_{ns}$ and $S_{ns}T_{ns}$, respectively. The sum of R_{ns} and T_{ns} is one. The angular dependence of the surface scattering parameter, [188, 189] the reflection coefficients, and the transmission coefficients [30, 182] have been studied before. For simplicity in our calculations we treat those as angle independent. With these definitions, the

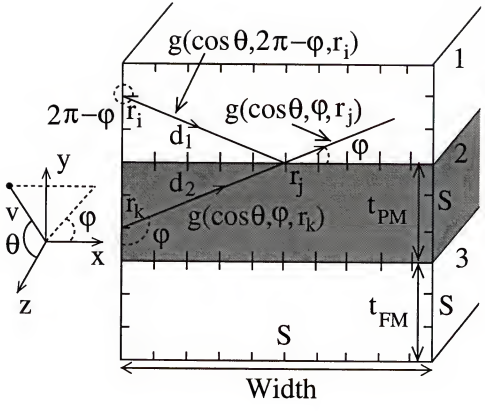

Figure 2.11: Schematic diagram of the three wire structure. Wires 1 and 3 are the ferromagnets of thickness t_{FM}, and wire 2 is a paramagnet of thickness t_{PM} stacked along the $\hat{y}$ direction. Current is in plane (CIP) along the $\hat{z}$ direction. S represents the spin independent specularity factors at the sides of the ferromagnet, and the paramagnet. Considering all possible incoming electrons from points on the edges and interfaces, e.g., points $\mathbf{r}_i$ and $\mathbf{r}_k$ the distribution functions for the outgoing electrons at point $\mathbf{r}_j$, $g(\cos\theta, \phi, \mathbf{r}_j)$ are determined. The exact relationship is described in the text [see Eq. (2.66)].

boundary conditions at the nth interface can be expressed as:

$$g_{ns}^{out}(\mathbf{v}, x, y_n) = S_{ns} T_{ns} g_{n-1s}^{in}(\mathbf{v}, x, y_n) + S_{ns} R_{ns} g_{ns}^{in}(-\mathbf{v}, x, y_n), \quad (2.64)$$

$$g_{n-1s}^{out}(-\mathbf{v}, x, y_n) = S_{ns} T_{ns} g_{ns}^{in}(-\mathbf{v}, x, y_n) + S_{ns} R_{ns} g_{n-1s}^{in}(\mathbf{v}, x, y_n), \quad (2.65)$$

where y_n is the position of the interface, and the superscripts out, in correspond to electrons going out from the boundary or coming in to the boundary. Similar equations are satisfied at the sides of the layers except that there is no transmission ($T = 0, R = 1$). Fig. 2.12 illustrates one of the boundary conditions [Eq. (2.64)].

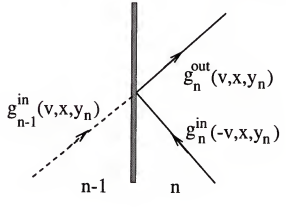

Figure 2.12: Pictorial representation of Eq. (2.64). Only the outgoing and incoming distribution functions of the electrons at the interface of $(n-1)$th and nth layers are shown. The reflected part of the incoming electrons in the nth layer, $g_{ns}^{in}(-\mathbf{v}, x, y_n)$, and the transmitted part of the incoming electrons in the $(n-1)$th layer, $g_{n-1s}^{in}(\mathbf{v}, x, y_n)$ contribute to the outgoing distribution function $g_{ns}^{out}(\mathbf{v}, x, y_n)$. The specularity factor of the interface is S_{ns}.

We use an iterative procedure to compute the distribution functions, $g_{ns}^{out}(\mathbf{v}, \mathbf{r_B})$, which are non-uniform along the $\hat{x}$ and $\hat{y}$ directions of the interfaces and edges (see Fig. 2.11). Our numerical procedure is similar to that applied to calculate the con-

ductivity for a thin wire in Section 2.3. However we briefly describe our numerical procedure below.

From Eq. (2.4), we see that the $g_{ns}^{out}(\mathbf{v},\mathbf{r})$'s with different velocities projected along the $\hat{z}$ direction are decoupled. This allows us to discretize the $g_{ns}^{out}(\mathbf{v},\mathbf{r})$ according to $\cos\theta = v_z/|v|$ and solve each separately. For each $\cos\theta$, $g_{ns}^{out}(\mathbf{v},\mathbf{r})$ at the edges and the interfaces carry two more indices: an angle ϕ and a position $\mathbf{r}_i$. The $g_{ns}^{out}(\mathbf{v},\mathbf{r})$'s for different ϕ and $\mathbf{r}_i$ are related via Eq. (2.6) and the boundary conditions given in Eqs. (2.64) and (2.65). To illustrate this we consider the relations between the distribution functions of the outgoing electrons at the first interface in Fig. 2.11:

$$\begin{aligned} g_{1s}^{out}(\cos\theta,\phi,\mathbf{r}_j) &= S_{1s}R_{1s}g_{1s}^{out}(\cos\theta,2\pi-\phi,\mathbf{r}_i)e^{-d_1/\tau_{1s}v_F\sin\theta} \\ &+ S_{1s}T_{1s}g_{2s}^{out}(\cos\theta,\phi,\mathbf{r}_k)e^{-d_2/\tau_{2s}v_F\sin\theta}. \end{aligned} \tag{2.66}$$

Here d_1, d_2 are the path lengths projected onto the $x-y$ plane from one boundary to another. Initial guesses for $g_{ns}^{out}(\cos\theta,\phi,\mathbf{r}_i)$ are taken from the nearby $g_{ns}^{out}[\cos\theta-\delta(\cos\theta),\phi,\mathbf{r}_i]$. The calculations are converged to within 1% with the total number of divisions for $\cos\theta$, $\mathbf{r}_i$, and ϕ chosen as $N_{\cos\theta}=100$, $N_\phi=500$, and $N_i=400$, respectively.

From the distribution functions at the boundaries using Eqs. (2.3) and (2.63) we can determine the distribution function of the electrons with momentum $\mathbf{v}$ at any point $\mathbf{r}$. Following Eq. (2.15) we then calculate the conductivities both for parallel and antiparallel alignments of the magnetizations. Finally, the giant magnetoresistance is obtained from Eq. (2.42).

We now consider the different input parameters of our problem. They are: the spin dependent mean free paths in the ferromagnet, $L^{\uparrow,\downarrow}$, the mean free path in the paramagnet, L^{PM}, the spin-dependent transmission coefficients, $T^{\uparrow,\downarrow}$, the specularity factors, S, and the thicknesses of the layers, t_{FM} and t_{PM}. We choose the mean free paths to be those determined in an experiment on a Co/Cu/Co structure: [181] $L^{\uparrow} = 55$ Å, $L^{\downarrow} = 10$ Å, and $L^{\mathrm{PM}} = 226$ Å. The transmission coefficients are obtained from an average of the transmission coefficients calculated by Stiles: [182] $T^{\uparrow} = 0.8$ and $T^{\downarrow} = 0.4$. We take the specularity factors at all interfaces and sides to be the same: $S = 0.9$. Finally, the thicknesses are chosen to be those of Cu when the Co layers are antiferromagnetically coupled at zero field [9]. For simplicity we take the ferromagnets to have the same thicknesses as the paramagnets: $t_{\mathrm{FM}} = t_{\mathrm{PM}}$.

GMR is due to both spin anisotropies in the bulk and surface scattering. To understand the role of bulk and surface scattering in GMR we consider the limiting cases i.e., when the GMR is due to only bulk scattering anisotropies or only surface scattering anisotropies. To do this, we consider two special cases: (a) when the transmission coefficients are equal: $T^{\uparrow} = T^{\downarrow} = 0.6$ and (b) when the bulk mean free paths in the ferromagnet are equal: $L^{\uparrow} = L^{\downarrow} = 17$ Å. In the following these are referred to as the (a) bulk scattering case and (b) surface scattering case.

In Fig. 2.13 we plot the giant magnetoresistance as a function of width for the three cases: (a) GMR due to bulk scattering anisotropies, (b) GMR due to surface scattering anisotropies, and (c) GMR due to both bulk and surface scattering anisotropies. In all cases the giant magnetoresistance decreases with decrease in the width. The decrease of GMR with lateral confinement can be understood by

considering a film, i.e., a wire with infinite width. Diffusive scattering at the sides of the wire reduces the conductivity and mean free paths of the wire compared to the film. This reduction in the conductivity in going from a film to a wire should be comparable to the reduction in going from a bulk system to a film with a thickness equal to w. Following Eq. (2.16) the conductivity of such a film is

$$\begin{aligned}\sigma_{\text{slab}} &= \left(\frac{ne^2L}{mv_F}\right)\left\{1-\frac{3L}{2w}(1-S)\right. \\ &\times \left.\int_0^1 d(\cos\theta)\cos\theta\sin^2\theta\frac{1-\exp(-w/L|\cos\theta|)}{[1-S\exp(-w/L|\cos\theta|)]}\right\}, \qquad (2.67)\end{aligned}$$

where the bulk conductivity, σ_{bulk} is defined in Eq. (2.17). We obtain an effective mean free path, L_{eff}, by replacing the mean free path L in Eq. (2.17) with L_{eff} such that $\sigma_{\text{bulk}} = \sigma_{\text{film}}$. The effective mean free paths can be used in a multilayer calculation with infinite width wires. The results of such an effective mean free path multilayer calculation (similar to Section 2.4) are plotted as the solid lines in Fig. 2.13. This approximation is in good agreement with the exact results (symbols), and hence we conclude that the reduction in the GMR is due to a decrease in the effective mean free path within the layers.

Although the GMR is reduced in all the cases shown in Fig. 2.13, the actual GMR vs. width curves are different. In particular, there are different length scales at which the GMR is reduced. The width at which the GMR is half its infinite width value, GMR(wire)/GMR(film) = 1/2, is defined as the half-width. In Fig. 2.14 we have rescaled the GMR vs. width curves shown in Fig. 2.13 by GMR(film) and the half-width. All the points fall close to a single curve. This means that the half-width and the GMR for infinite width wires, GMR(film), determine the GMR

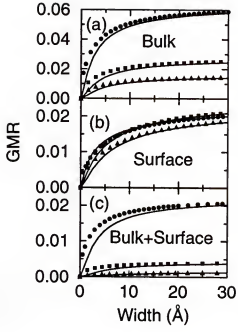

Figure 2.13: Giant magnetoresistance of a three wire structure as a function of width for (a) bulk scattering, (b) surface scattering and (c) both bulk and surface scattering. The symbols refer to different film thicknesses, $t_{\rm PM} = t_{\rm FM} = 8$ Å (circle), 20 Å (box), and 30 Å (triangle). In all cases the GMR decreases as we laterally confine the multilayers. The origin of this decrease in the GMR can be understood in terms of changing the effective mean free paths in the wires. As the wire width is reduced the effective mean free path within each wire decreases. To make this more quantitative we obtain an effective mean free path for each wire and use these mean free paths in a multilayer calculation (infinite width wire). The results, which are shown as the solid lines, are in good agreement with the exact calculation (symbols). For cases (a) and (c) the mean free paths are chosen for a Co/Cu/Co structure, [181] which has $L^{\uparrow} = 55$ Å, $L^{\downarrow} = 10$ Å, and $L^{\rm PM} = 226$ Å. For case (b), in which only surface scattering contributes to the GMR, we use $L^{\uparrow} = L^{\downarrow} = 17$ Å and $L^{\rm PM} = 226$ Å. For cases (b) and (c) the transmission coefficients at the interfaces are taken to be $T^{\uparrow} = 0.8$, $T^{\downarrow} = 0.4$, [182] while for case (a), where the GMR is due only to bulk scattering, we take $T^{\uparrow} = T^{\downarrow} = 0.6$. The thicknesses for wire 2 are chosen to be that of Cu when the Co slabs are antiferromagnetically coupled, [9] and for simplicity we choose the Co layers to have the same thickness as the Cu. In all cases the sides and the interfaces have a specularity factor $S = 0.9$.

vs. width curves. We have also tried the same rescaling with other values of S, which is still the same for all sides and interfaces, and found the same curve.

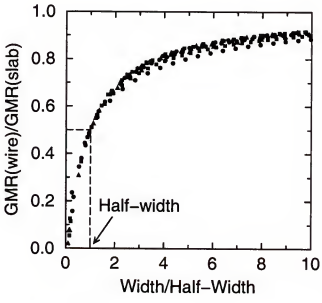

Figure 2.14: Rescaled giant magnetoresistance as a function of width. For large width the GMR for a wire approaches that for an ordinary unconfined multilayer, GMR(film). We define the width at which the GMR is reduced to half of GMR(film) as the half-width. Rescaling the giant magnetoresistance by GMR(film) and the width by the half-width, the GMR vs. width curves of Fig. 2.13 fall onto a single curve. The symbols are the same ones used in Figs. 2.13(a)-(c).

In Figs. 2.15(a) – (c) we have plotted the half-width as a function of the mean free paths in the ferromagnet and the thicknesses. The cases (a) – (c) refer to the same parameters as in Fig. 2.13. The ratio between the mean free paths in the ferromagnet is fixed to $L^{\uparrow}/L^{\downarrow} = 5.5$ in Figs. 2.15(a) and (c), which is the same ratio used in Figs. 2.13(a) and (c). As for Fig. 2.15(b), the mean free paths are equal in the surface scattering case of Fig. 2.13(b): $L^{\uparrow} = L^{\downarrow}$.

For bulk scattering anisotropies [Fig. 2.15(a)] the half-width increases almost linearly with both the thickness and the mean free path. On the other hand, for surface scattering anisotropies [Fig. 2.15(b)] the half-width depends primarily on the thickness of the film and only weakly on the mean free paths in the ferromagnet. When both surface and bulk scattering anisotropies are present [Fig. 2.15(c)], the dependence of the half-width on the mean free path and thickness can be complicated. In the region where the half-width has a peak in Fig. 2.15(c), the GMR has a local minimum as a function of the mean free path. The origin of this local minimum comes from the near cancellation of the GMR from the bulk and surface contributions. The location of this minimum depends primarily on the transmission coefficients.

In general GMR will decrease when the multilayers are laterally confined, but there are very special cases where the GMR actually increases with lateral confinement. The two ways we have found to do this are (i) by introducing additional spin dependence in the scattering at the sides of the wires and (ii) have the sides of the wires selectively decrease the resistivity in the ferromagnet relative to the paramagnet. This again can be understood in terms of the decrease in the effective mean free paths within each layer as we confine the multilayers. By changing the mean free paths by different amounts, one can tune the GMR. As an example in Fig. 2.16 we have plotted the GMR vs. width for two cases which differ only by the specularity factor at the sides of the FM. For the solid curve the specularity factors are 0.9 for both spin-up and spin-down electrons, while for the dashed curve the specularity factor at the sides for spin-up electrons is 0.9 and for spin-down electrons is 0.5. The GMR actually increases as one decreases the width of the

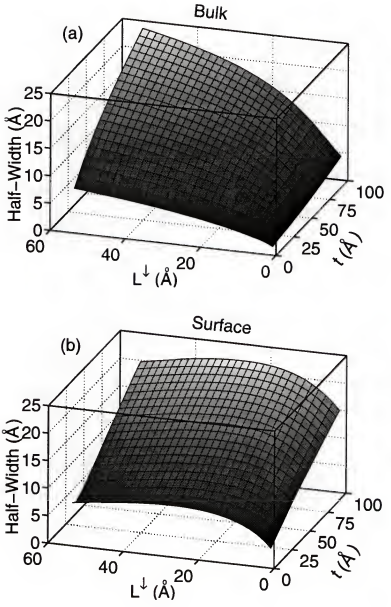
Bulk
(a)
Half–Width (Å)
25
20
15
10
5
0
60
40
20
0
L↓ (Å)
0
25
50
75
100
t (Å)
Surface
(b)
Half–Width (Å)
25
20
15
10
5
0
60
40
20
0
L↓ (Å)
0
25
50
75
100
t (Å)

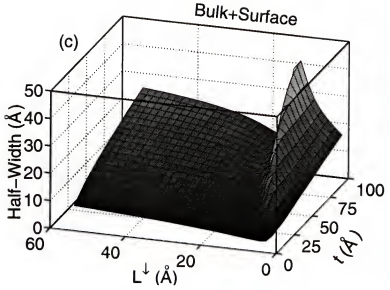

Figure 2.15: Half-width as a function of the thickness and mean free path in the ferromagnet ($L^{\downarrow}$) for (a) bulk scattering, (b) surface scattering, and (c) bulk and surface scattering. In Fig. 2.15(a) and (c) the ferromagnetic spin-up and spin-down mean free paths are kept at a fixed ratio, $L^{\uparrow}/L^{\downarrow} = 5.5$, which is the same ratio used in Figs. 2.13(a) and (c). In the surface scattering case of Fig. 2.15(b) $L^{\uparrow}$ equals $L^{\downarrow}$. The half-width depends both on the thickness and the mean free path for all three cases. In case (a), bulk scattering, the half-width increases roughly linearly with the thickness and the mean free path, while in case (b), surface scattering, the half-width depends primarily on the thickness of the layers. The general case when both bulk and surface scattering are important [case (c)] can lead to complex dependence on the mean free path and film thickness. The feature at small $L^{\downarrow}$ in (c) is associated with the fact that the GMR has a local minimum in this region (see discussion in text). Except for t and $L^{\downarrow}$, which vary, the parameters used in (a), (b), and (c) are the same as in Fig. 2.13.

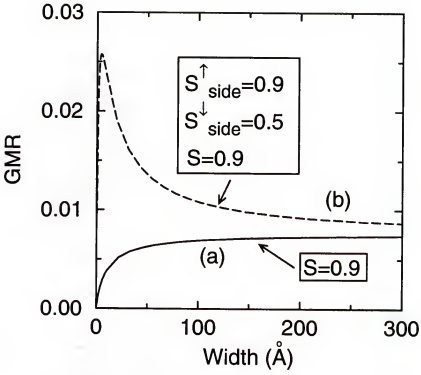

Figure 2.16: Giant magnetoresistance as a function of width for (a) spin-independent scattering at the sides and interfaces, (b) spin-dependent scattering at the sides of the ferromagnet. For (a), the GMR decreases with decreasing width (solid line), whereas for (b), the GMR increases with decreasing width (dashed line). The increase of the GMR with reduced width is due to the spin-down mean free path decreasing faster than the spin-up one. For (a), we choose the same parameters as of Fig. 2.13, except the mean free paths for the spin-up and down electrons in the ferromagnet are 200 Å and 100 Å, respectively. For (b), we use the same parameters except that the specularity factors for the sides of the ferromagnet are spin-dependent: $S^{\uparrow}_{\text{side}} = 0.9$ and $S^{\downarrow}_{\text{side}} = 0.5$. Note that the GMR eventually goes to zero for small enough widths because the effective mean free path in the paramagnet becomes much smaller than the thickness of the paramagnetic layer.

sample because the mean free path for spin-down electrons decreases more rapidly than the mean free path for spin-up electrons. Such spin dependent specularity factors may occur naturally or be attainable by coating the sides of the multilayer. Allowing spin-dependent specularity factors at non-transmitting interfaces opens up the possibility that one can create a GMR device without ferromagnetic conductors, but only insulating ferromagnets which change the surface scattering.

2.5 Conclusion

We have studied the effect of lateral confinement on the giant magnetoresistance in the CIP geometry. With spin independent specularity factors at the sides of the wires the GMR in general decreases as we reduce the width of the wires. In this case we found that the GMR vs. width curves could be very nearly collapsed onto a single curve by rescaling the GMR by its infinite width value and the width by the half-width. The half-width depends on both the mean free paths and the thickness of the films. For the case of the GMR due solely to surface scattering, the thickness of the sample plays a dominant role in determining the half-width, while in the case of GMR due solely to bulk scattering, the half-width increases roughly linearly with both the mean free paths in the ferromagnetic wires and the thicknesses. The general case when both surface and bulk anisotropies are important can lead to more complex dependences.

The source of the decrease in the GMR in the CIP geometry is a reduction in the effective mean free path in the layers due to scattering off the sides of the wires. We showed this quantitatively by determining an effective mean free path within each wire and substituting it into a multilayer calculation for films (infinite

width wires). The results of the approximate solution and the exact solution agree quite well.

For the case of spin-dependent mean free paths we find that there are parameter regimes where the GMR in CIP geometry can increase as the sample is laterally confined. The origin of the increase is again changing of the effective mean free path within each layer as one decreases the width. With spin-dependent specularity factors one can change the ratio of the mean free paths for spin-up and spin-down electrons and hence change the GMR. Thus, with appropriately prepared sides of the wires, one may be able to increase or at least stem the decrease in the GMR. In any case the length scale at which the reduction in the GMR takes place is typically quite small, of order the mean free paths and the thicknesses of the layers. The effects discussed here will not be important until one goes to very small samples.

CHAPTER 3
JUNCTION MAGNETORESISTANCE (JMR) IN DOUBLE TUNNEL JUNCTIONS WITH MAGNETIC METALS

Magnetoresistance in ferromagnetic tunnel junctions have been studied extensively both experimentally and theoretically in the last few years [63, 190]. More recently there are experiments where magnetoresistance has been studied in the Coulomb blockade regime. Experimental results on these recent experiments were shown in Section 1.2 of the introduction. The purpose of this chapter is to theoretically investigate in detail the magnetoresistance of a double-tunnel-junction with magnetic metals in the Coulomb blockade regime, i.e. at very low temperature where the charging energy exceeds the thermal energy. The layout of the chapter is the following. We first begin with the theoretical formalism of the Coulomb blockade. We recover the well known results: the Coulomb gap and the Coulomb staircase structure in the current-voltage characteristic curves. Dependencies on different parameters are also studied. In the next section we use the same model to calculate the non-linear conductances and the junction magnetoresistance of a double-tunnel-junction with magnetic metals. The results are studied in detail. Finally in the last section we summarize our main results.

3.1 Coulomb Blockade in Double Tunnel Junctions

Coulomb blockade in the current-voltage characteristic curves is a manifestation of single-electron tunneling through nano-scale tunnel junctions. The experimental

realization of a double-tunnel-junction consists of three metals separated by oxide layers which act as insulators. The two end leads, denoted by left (L) and right (R), are connected to a constant voltage source V. This double junction can be modeled as a closed loop electrical circuit with two leaky capacitors of capacitances $C_{\rm L}$ and $C_{\rm R}$ connected in series (Fig. 3.1). The resistances of the junctions, R_L and R_R, are connected in parallel to C_L and C_R respectively. Depending on the

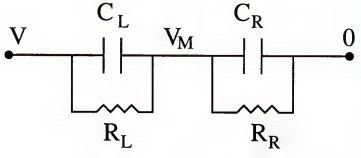

Figure 3.1: Schematic diagram of a double tunnel junction system. The left and right capacitors (C_L and C_R) are connected in series with a voltage source. The resistances of the left and right junctions are R_L and R_R, respectively. The voltage in the left and right leads are kept fixed at V and 0, whereas in the central region the voltage V_M changes.

number of excess electrons, n, in the center metal, the voltage in the central region V_M fluctuates. The voltage drops, $[V_L - V_M(n)]$ and $[V_M(n) - V_R]$, across the left and the right junctions are

$$V_L - V_M(n) = \frac{C_R}{C}V + \frac{ne}{C} + V_P, \tag{3.1}$$

$$V_M(n) - V_R = \frac{C_L}{C}V - \frac{ne}{C} - V_P, \tag{3.2}$$

where $-e$ is the charge of the electron and C is the capacitance $(C_L + C_R)$. The offset voltage, V_P, accounts for the fact that even when n and V are zero, V_M may

not be zero due to the alignment of the Fermi energy in the middle region. Such effects are seen experimentally [97, 191] in a shifting of the $I - V$ characteristic away from a symmetric curve $[I(V) = I(-V)]$. A nonzero V_P can also be created deliberately by patterning a gate capacitor to the central region [192, 193, 194]. To describe the transport of electrons we use a semiclassical model [83, 195, 196, 197]. The different tunneling rates that enter into the dynamics are: the rate for electrons to tunnel onto the center metal from the left ($\Gamma^L_{n\to n+1}$) and right ($\Gamma^R_{n\to n+1}$), and the rate for the electrons to leave the center metal to the left ($\Gamma^L_{n\to n-1}$) and right ($\Gamma^R_{n\to n-1}$). They are pictorially shown in Fig. 3.2. These tunnel rates are calculated

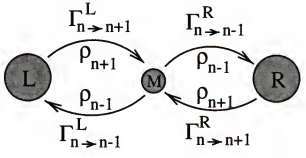

Figure 3.2: The four different tunneling rates (Γ's) are shown pictorially. The probability that there are n electrons at the center metal at any time t is $\rho_n(t)$.

using Fermi's Golden rule. As an example, $\Gamma^L_{n\to n+1}$ is calculated by integrating over energy (dE), the square of the tunneling matrix element coupling the initial and final states ($|T(E)|^2$), the number of occupied initial states, and the number of unoccupied final states:

$$\Gamma^L_{n\to n+1} = \frac{2\pi}{\hbar}\int_{-\infty}^{\infty} dE|T(E)|^2 N_L(E-E_L)N_M(E-E_M)f(E-E_L)[1-f(E-E_M)], \tag{3.3}$$

where $f(E) = 1/[1 + \exp(\beta[E - E_F])]$ is the Fermi-distribution function, β is related to the temperature T via $\beta = 1/k_B T$. $N_L(E)$, $N_M(E)$ are the density of states of the left and the center metals, and E_L, E_M are their Fermi energies. For simplicity, we assume $N_L(E), N_M(E)$ and $|T(E)|^2$ are energy independent, so that $N_L(E) \approx N_L^0$, $N_M(E) \approx N_M^0$, and $|T(E)|^2 \approx |T_0|^2$. With these assumptions Eq. (3.3) becomes

$$\Gamma^L_{n\to n+1} = \frac{2\pi}{\hbar}|T_0|^2 N_L^0 N_M^0 \int_{-\infty}^{\infty} dE f(E - E_L)[1 - f(E - E_M)]. \tag{3.4}$$

We define

$$R_L = \frac{\hbar}{2\pi e^2 N_L^0 N_M^0 |T_0|^2} \tag{3.5}$$

to be the resistance of the left lead. The resistance of the right lead can be defined in a similar way by replacing $L \leftrightarrow R$. One of the basic requirement for single charge tunneling phenomenon to occur is that the tunneling resistances R_L, R_R must exceed the resistance quantum $R_K = \hbar/2\pi e^2 \simeq 25.8$ kΩ i.e., $R_{L(R)} >> R_K$.

Using the identity

$$f(E)[1 - f(E + x)] = \frac{f(E) - f(E + x)}{1 - \exp(-\beta x)}, \tag{3.6}$$

the integral in Eq. (3.4) can be evaluated analytically. The end result for the tunnel rate is

$$\Gamma^L_{n\to n+1} = \left(\frac{1}{e^2 R_L}\right)\left[\frac{E_L - E_M}{1 - \exp(-\beta[E_L - E_M])}\right]. \tag{3.7}$$

Similarly it follows that,

$$\Gamma^{R}_{n\to n+1} = \left(\frac{1}{e^2 R_R}\right)\left[\frac{E_R - E_M}{1-\exp(-\beta[E_R - E_M])}\right]. \tag{3.8}$$

For convenience we introduce a function $\gamma(\epsilon)$:

$$\gamma(\epsilon) = \frac{\epsilon}{1-e^{-\beta\epsilon}}. \tag{3.9}$$

In terms of the above function the various tunnel rates are:

$$\Gamma^{L(R)}_{n\to n\pm 1} = \left(\frac{1}{e^2 R_{L(R)}}\right)\gamma\left\{\pm(E_{L(R)} - E_M)\right\}. \tag{3.10}$$

We now need to calculate the difference between the right (and left) electrode Fermi energy before a tunneling event and the energy of the center electrode after the event, i.e. $(E_R - E_M)$ [and $(E_L - E_M)$] is the energy the electron gains during the tunneling process. For our calculation we consider the voltage source (the battery)

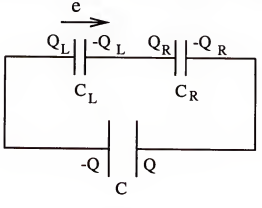

Figure 3.3: Schematic diagram showing charge transfer in a double-tunnel-junction

to be a capacitor with a capacitance C much larger than the capacitances of the

left (C_L) and the right (C_R) junctions. In equilibrium we have from Kirchoff's voltage law

$$\frac{Q}{C} = \frac{Q_L}{C_L} + \frac{Q_R}{C_R}, \tag{3.11}$$

where Q_L, Q_R, and Q are the charges on the left, right, and the big capacitors respectively. Now let us consider that an electron crosses the left junction [See Fig. 3.3], changing the charge in the central region from ne to $(n-1)e$ where n is the excess electrons in the central region. The charge in the left junction also decreases from Q_L to $(Q_L - e)$ and the charge in the second junction is constant. The new charges $(Q_L - e)$ and Q_R do no longer satisfy electrostatic equilibrium. To reestablish equilibrium the big capacitor transfers a charge q to the left and the right capacitors. Thus we have

$$\frac{Q+q}{C} = \frac{Q_L - e + q}{C_L} + \frac{Q_R + q}{C_R}. \tag{3.12}$$

Eqs. (3.11) and (3.12) can be solved for q with the result

$$q = \frac{eC_R}{(C_L + C_R) - C_L C_R / C}. \tag{3.13}$$

The total increase in energy ($\triangle E = E_M - E_L$) due to this tunneling process is:

$$\begin{aligned} \triangle E &= \frac{[Q_L - e + q]^2}{2C_L} + \frac{[Q_R + q]^2}{2C_R} + \frac{[Q+q]^2}{2C} \\ &- \frac{Q_L^2}{2C_L} - \frac{Q_R^2}{2C_R} - \frac{Q^2}{2C}. \end{aligned} \tag{3.14}$$

Substituting the value of q from Eq. (3.13) and taking the limit $C >> C_R, C_L$ we obtain

$$\begin{aligned} E_M - E_L &= \frac{e}{C_L + C_R}\left[\frac{e}{2} - ne\right] - \frac{eVC_R}{C_L + C_R}, \\ &= \frac{e}{C_L + C_R}\left[\frac{e}{2} - ne - C_R V\right], \\ &= E_C - e\left[V_L - V_M(n)\right]. \end{aligned} \tag{3.15}$$

Similarly we can calculate the change in the energy across the right junction. Considering both of them we have

$$E_L - E_M = -e[V_M(n) - V_L] - E_C, \tag{3.16}$$

$$E_R - E_M = e[V_M(n) - V_R] - E_C. \tag{3.17}$$

Here $E_C = e^2/2(C_L + C_R)$ is the charging energy of the system. Substituting Eqs. (3.16) and (3.17) in Eq. (3.10) we obtain

$$\Gamma^{L(R)}_{n\to n\pm 1} = \left(\frac{1}{e^2 R_{L(R)}}\right)\gamma\left\{\pm e\left[V_M(n) - V_{L(R)}\right] - E_C\right\}. \tag{3.18}$$

The transport of the electrons thorough the tunnel junctions is given by a master equation which describes the time evolution of the probability, $\rho_n(t)$, for n excess electrons in the center metal [83]

$$\begin{aligned} \frac{d\rho_n(t)}{dt} &= \left[\rho_{n+1}\Gamma_{n+1\to n} - \rho_n\Gamma_{n\to n+1}\right] \\ &- \left[\rho_n\Gamma_{n\to n-1} - \rho_{n-1}\Gamma_{n-1\to n}\right], \end{aligned} \tag{3.19}$$

where the net tunnel rate $\Gamma_{i\to j}$ is equal to $\left(\Gamma^L_{i\to j}+\Gamma^R_{i\to j}\right)$. Defining a matrix $\mathbf{M}$ with components

$$M_{mn}=\left\{\begin{array}{c}\Gamma_{n\to m}\text{ if } m=n\pm 1\\ -\Gamma_{n\to n+1}-\Gamma_{n\to n-1}\text{ if } m=n\\ 0\text{ otherwise,}\end{array}\right\} \tag{3.20}$$

the master equation may be written in a compact form

$$\frac{d\rho(t)}{dt}=\mathbf{M}\rho(t). \tag{3.21}$$

Due to $\sum_m M_{mn}=0$ which follows from Eq. (3.20) and Eq. (3.21), $\rho_n(t)$ is independent of time. The steady state solution $(d\rho_n(t)/dt=0)$ then has to satisfy

$$\mathbf{M}\rho^{(\mathbf{0})}=0. \tag{3.22}$$

At steady state, the current in the left junction equals the current in the right junction due to current conservation, and is given by

$$I=e\sum_{n=-\infty}^{n=\infty}\rho_n\left(\Gamma^L_{n\to n-1}-\Gamma^L_{n\to n+1}\right). \tag{3.23}$$

To write Eq. (3.23) succinctly we define a new matrix $\mathbf{v^L}$ where

$$v^L_{mn}=\left\{\begin{array}{c}-\Gamma^L_{n\to m}\text{ if m = n − 1}\\ \Gamma^L_{n\to n+1}\text{ if m = n + 1}\\ 0\text{ otherwise,}\end{array}\right\} \tag{3.24}$$

The tunneling current can also now be expressed in a compact form as

$$\begin{aligned} I &= -e\sum_m [v^L \rho(\mathbf{t})]_m \\ &\equiv -e\mathrm{Tr}\{v^L \rho(\mathbf{t})\}. \end{aligned} \tag{3.25}$$

To evaluate the current in general, Eqs. (3.21) – (3.25) have to be solved numerically. We follow the procedure described in Ref. [196]. We diagonalize the matrix $\mathbf{M}$ and determine its eigenvalues and eigenvectors. The eigenvector with the zero eigenvalue is the steady state solution ρ^0. At low temperature and voltage, the higher charge states $|n| >> 1$ are energetically forbidden and therefore we can neglect them. We found that for our choice of parameters it is sufficient to keep the 19 states around $n = 0$. The highest and the lowest states are $n = 9$ and $n = -9$.

We restrict ourselves to low temperature and in the regime where the charging energy is larger than the thermal energy, i.e. $k_B T << E_c$. The number of independent parameters in our model are the ratio of the resistances $R_L/(R_L + R_R)$, the ratio of the capacitances $C_L/(C_L + C_R)$, and the additional voltage V_p. In Fig. 3.4 we plot the tunneling current as a function of voltage for $CV_p = 0$ and $CV_p = 0.25$ for $k_B T = 0.01 E_C$. As expected for an asymmetric junctions with $R_L = 0.01(R_L + R_R)$ and $C_L = 0.01(C_L + C_R)$, the curves exhibit a step-like structure. This is known as Coulomb staircase. Also note that there is no current if the external voltage is smaller than $e/2C$. This shift in the current-voltage characteristic is called the Coulomb gap and the phenomenon of suppression of the current below $e/2C$ is referred to as Coulomb blockade. Comparing the two curves in Fig.

3.4, one with a finite offset voltage and the other without the offset voltage we find that the effect of a finite offset voltage V_p is to shift the $I-V$ curves. Hence, we will consider $V_p = 0$ for our later calculations.

To study the dependence of the tunneling current on the ratio of the capacitances and resistances we plot in Fig. 3.4 the $I-V$ curves for different values of the ratios. For asymmetric junctions with $R_L << R_R$ and $C_L << C_R$ (or $R_L >> R_R$ and $C_L >> C_R$) the Coulomb staircase structure is seen. With increase in the ratios $R_L/(R_L + R_R)$ and $C_L/(C_L + C_C)$ the step-like structure diminishes and finally for $R_L << R_R$ and $C_L >> C_R$ (or $R_L >> R_R$ and $C_L << C_R$) no step-like structure is seen.

The effect of temperature is to smear out the step-like structure seen in the $I-V$ curves. This can be seen by comparing Fig. 3.5 with Fig. 3.4. With increase in temperature the number of accessible states increases which thus destroys the step-like pattern.

3.2 Magnetoresistance in the Coulomb Blockade Regime

In this section we will study the different transport properties of a double-tunnel junction with magnetic metals, specifically the conductances, the differential conductances for parallel and antiparallel magnetization alignment and the magnetoresistance. To estimate the junction resistances we will use Julliere's model [65] which has been described in the section 1.2 of Chapter 1. In this model, for example the parallel, G^{P} and antiparallel conductances G^{AP}, for a FM/I/FM tunnel

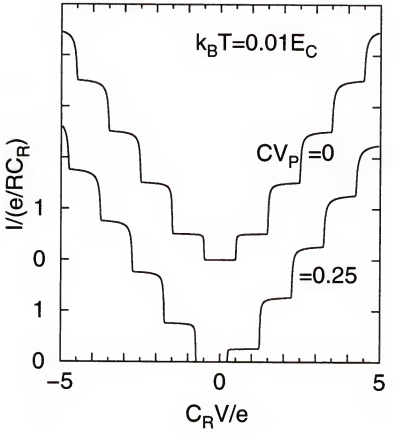

Figure 3.4: Current-Voltage curves at low temperature, $k_BT = 0.01E_C$ for two different values of the offset voltage $V_p = 0.25$ and $V_p = 0$. In both cases we see the Coulomb staircase structure and the Coulomb gap. The suppression of the current at low voltages is known as the Coulomb blockade. As an example, note that for $V_p = 0$ current is suppressed below $e/2C$. The width of the Coulomb gap is e/C. A finite V_p only shifts the $I-V$ curves. In both cases the ratio of resistances and capacitances are kept fixed to $R_L/(R_L+R_R) = 0.01$ and $C_L/(C_L+C_R) = 0.01$.

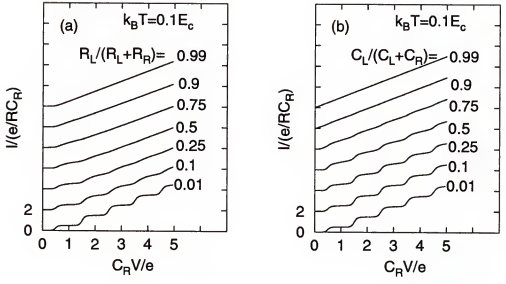

Figure 3.5: Tunneling current as a function of voltage for different values of the ratio of the resistances and capacitances. For case (a) we keep the ratio of the capacitances fixed to $C_L/(C_L + C_R) = 0.01$ and vary the ratio of $R_L/(R_L + R_R)$. For case (b) we keep $R_L/(R_L + R_R)$ to be fixed to 0.01 and vary the ratio of the capacitances $C_L/(C_L + C_R)$. In both cases with increase in the ratio of the resistances or the capacitances the staircase structure disappears. The temperature is kept fixed ($k_BT = 0.1E_C$).

junction are given by:

$$G^{\mathrm{P}} = \left(\frac{e^2}{h}\right) |T|^2 N_1 N_2 \left\{a_1 a_2 + (1-a_1)(1-a_2)\right\}, \tag{3.26}$$

$$G^{\mathrm{AP}} = \left(\frac{e^2}{h}\right) |T|^2 N_1 N_2 \left\{a_1(1-a_2) + (1-a_1)a_2\right\}. \tag{3.27}$$

Here the tunneling matrix element T, is taken to be both energy and momentum independent. The density of states of the electrons at the Fermi level in the two ferromagnets are N_1 and N_2 and the fraction of the number of spins parallel to the magnetization in the two FMs are a_1 and a_2 respectively. Using the definitions of the spin polarizations P_1 and P_2 of the two FMs

$$P_1 = 2a_1 - 1, \tag{3.28}$$

$$P_2 = 2a_2 - 1. \tag{3.29}$$

Eqs. (3.26) and (3.27) can be rewritten in terms of P_1 and P_2.

For magnetic materials, there are two types of carriers: the majority electrons with spins parallel to the magnetization and the minority electrons with spins antiparallel to the magnetization. We make the assumption that the rate of tunneling through the junctions is much smaller than the rate of spin relaxation. Under this assumption the number of majority and minority electrons in the center metal is not conserved separately, but their sum is conserved. The time evolution of the probability, $\rho_n(t)$, for n excess electrons in the center metal [83] is described by the master equation [Eq. 3.21]. Following the same procedure as described in the context of Coulomb blockade the current is calculated using Eq. (3.25). The

total conductance G is then simply given by dividing the current with the voltage, $G = I/V$, and the differential conductance G_{diff} is obtained by differentiating the current with respect to the voltage, $G_{\text{diff}} = dI/dV$.

Within the approximations we made there are two possible choice of materials which lead to non-zero magnetoresistance in a two junction system: (1) all the leads are ferromagnets, i.e. FM/I/FM/I/FM, and (2) the left or the right lead is a paramagnet, i.e. either FM/I/FM/I/PM or PM/I/FM/I/FM. Note that with the center lead non-magnetic (FM/I/PM/I/FM) there is no JMR or DJMR because the antiparallel conductance is identical to the parallel conductance within our assumption. For each of these cases, we calculate the conductances for two different relative orientations of the ferromagnet magnetizations: parallel and antiparallel. Here parallel (P) means that the magnetizations of all ferromagnets are in the same direction, and antiparallel (AP) means the magnetization of the center ferromagnetic metal has been reversed. In case (1) of three ferromagnetic metals, other configurations are also possible: the magnetization of the right or the left lead can be reversed keeping the magnetizations of the other two parallel. For case (2) where one of the left or the right lead is non-magnetic, the magnetization of right or the left ferromagnetic lead can also be reversed. However, the qualitative features of the current, conductance, and the magnetoresistance curves remain the same. The junction magnetoresistance (JMR) is defined as the ratio of the change in the conductance from parallel, G^{P} to antiparallel alignments, G^{AP}, divided by the parallel conductance

$$\text{JMR} = 1 - \frac{G^{\text{AP}}}{G^{\text{P}}}. \tag{3.30}$$

The differential junction magnetoresistance (DJMR) is defined in the same fashion as the JMR but with the total conductances replaced by the differential conductances, $G_{\rm diff}$,

$$\mathrm{DJMR} = 1 - \frac{G^{\rm AP}_{\rm diff}}{G^{\rm P}_{\rm diff}}. \tag{3.31}$$

We now consider the different parameters of our model. They are the capacitances C_L and C_R, the parallel resistances $R^{\rm P}_L$ and $R^{\rm P}_R$, the antiparallel resistances $R^{\rm AP}_L$ and $R^{\rm AP}_R$, the temperature T, and the offset voltage V_P. To estimate the antiparallel resistances, we use Julliere's model for FM/I/FM tunnel junctions, where the junction magnetoresistance is expressed as a product of the magnitudes of the polarizations of the ferromagnets: [65]

$$\frac{\triangle R}{R^{\rm AP}} = \frac{2P_1P_2}{(1+P_1P_2)}. \tag{3.32}$$

Here $\triangle R$ is the change in resistance from antiparallel to parallel orientations, $R^{\rm AP}$ is the junction resistance when the magnetizations of the ferromagnets are antiparallel, and P_1, P_2 are the spin polarizations of the two ferromagnets. Eq. (3.32) can be obtained from Eqs. (1.11) [See Section 1.2 of Chapter 1 for details].

In Fig. 3.6 the currents and the total conductances are plotted for parallel and antiparallel orientations of the magnetizations. Asymmetric junctions and low temperature are used to obtain the steps in the current. As expected in the Coulomb blockade regime, the current increases by steps (cases a and b), and the conductance shows oscillations with decreasing amplitude (case c). Case (a) corresponds to a finite offset voltage whereas cases (b) and (c) correspond to zero offset voltage. The effect of a finite V_P is to shift the $I-V$ curves. For convenience

we thus take the offset voltage to be zero for our later calculations. Finally, for large enough voltage, the current becomes linear with voltage and the conductance approaches the classical limiting value which is the inverse of the resistance of two resistors connected in series

$$G = \frac{1}{(R_L + R_R)}. \tag{3.33}$$

It is also interesting to look at the differential conductances (dI/dV) for parallel and antiparallel alignments of magnetizations. They are plotted as a function of voltage in Fig. 3.7. We see sharp spikes in the differential conductance curves at places where the voltage is equal to $ne/2C$ ($n = 1, 2, 3, ...$). At these places the current also increases by a step as seen in Fig. 3.6.

The effect of temperature dependence is shown in Fig. 3.8. With the rise in temperature, the number of accessible states increases. The steps in the current round off (case a), and the amplitude of the oscillations in the conductance vs. voltage curve (case b) gradually decreases. The peaks in the JMR (case c) and the DJMR vs. voltage curves (case d) become broader and reduced in size. The reduction of JMR with increase in temperature has been observed recently [198].

Considering the parameter regime where $k_B T << E_C$ and zero offset voltage ($CV_P = 0$), in Fig. 3.9 we plot the junction magnetoresistance for four different cases: (a) $FM_1/I/FM_1/I/FM_2$, (b) $FM_2/I/FM_1/I/FM_1$, (c) $FM_1/I/FM_1/I/PM$, and (d) $PM/I/FM_1/I/FM_1$, where FM_1 and FM_2 are different ferromagnetic metals. In the high bias regime (the Ohmic regime) for all four cases, the current is

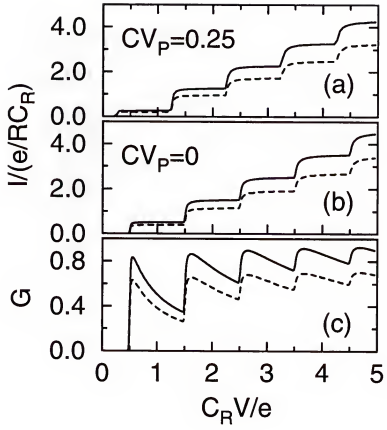

Figure 3.6: Current (I) and total conductance (G) as a function of voltage, for a FM/I/FM/I/FM tunnel junction. For cases (a), (b), and (c), the solid lines represent the current and the conductance for parallel alignment of the magnetizations, whereas the dashed lines are for antiparallel alignment. As a function of voltage the current shows steps (cases a and b), and the total conductance oscillates with decreasing amplitudes (case c). Case (a) corresponds to finite offset voltage $CV_P = 0.25$. Cases (b) and (c) are for zero offset voltage. The effect of a finite offset voltage is to shift the position of the $I - V$ curves. We choose the left and the center metals to be made of iron with polarization, $P_{\rm Fe} = 0.40$ and the right metal to be made of cobalt with polarization $P_{\rm Co} = 0.34$ [63]. The different parameters used are: $C_{\rm L} = 0.01C$, $R_{\rm L}^{\rm P} = 0.01(R_L^{\rm P} + R_R^{\rm P})$, and $k_BT = 0.01E_C$.

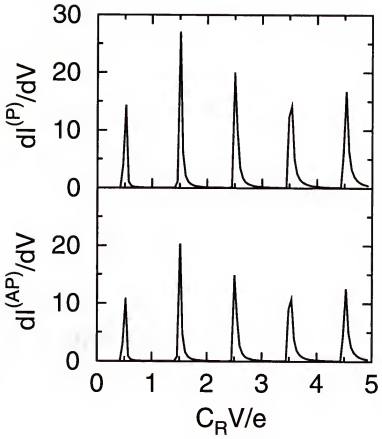

Figure 3.7: Differential conductance G_{diff} for parallel and antiparallel alignments of magnetizations as a function of voltage. Spikes are seen when the voltage is equal to $ne/2C$ where n is an integer. Spikes occur at those places where step-wise increase in current occur. Also note that the differential conductance for parallel orientation is larger than the differential conductance for antiparallel orientation. The parameters chosen are the same as in Fig. 3.6.

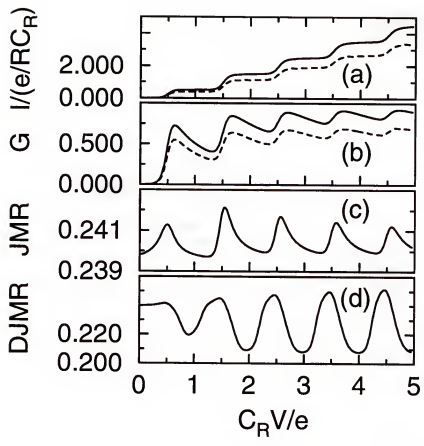

Figure 3.8: Temperature dependence of the (a) Current, (b) Conductances, (c) JMR, and (d) DJMR for a FM/I/FM/I/FM tunnel junction. As in Fig. 3.6, the solid and the dashed lines represent the current and the conductance for parallel and antiparallel alignments. With increase in temperature, the steps in the current vs. With increase in temperature, the steps in the current vs. voltage curve round off (case a), resulting in reduced amplitude of oscillations in the total conductance (case b). The peaks in both the JMR (case c) and the DJMR (case d) curves broaden. Also the peaks in the JMR and the DJMR curves decreases with increase in temperature. The parameters are the same as used in Fig. 3.6, except for the temperature which is $k_B T = 0.1 E_C$.

linearly proportional to the voltage [196]

$$I = \frac{e}{(R_L + R_R)C}\left[\frac{CV}{e} - 1\right]. \tag{3.34}$$

It then follows from Eq. (3.34), that the plateaus in Figs. 3.9(a) – 3.9(d) are given by the difference in the total resistances from antiparallel to parallel alignments divided by the total resistance for the antiparallel alignment,

$$\text{JMR(plateau)} = 1 - \frac{R_L^{\text{P}} + R_R^{\text{P}}}{R_L^{\text{AP}} + R_R^{\text{AP}}}. \tag{3.35}$$

For asymmetric junctions in the low voltage, low temperature regime we see spikes in the JMR vs. voltage curves in Fig. 3.9. The occurrence of the first spike can be understood analytically. We confine ourselves to only three states: the $n = 0$ state and the two states $n = \pm 1$ immediately accessible from it. At very low temperature, the state which is most likely occupied is the $n = 0$ state for $V_P = 0$. The tunnel rates $\Gamma_{0\to 1}$ and $\Gamma_{1\to 0}$ do not enter in the expression for the tunneling current at zero temperature, but at finite temperature they do contribute. In the limit of zero temperature, where we replace the function $\gamma(\epsilon)$ in Eq. (3.9) by $\gamma(\epsilon) = \epsilon\theta(\epsilon)$, the steady state current can be expressed in terms of the tunnel rates in the regime $(e/2) \leq C_R V \leq (C_R/C_L)(e/2)$ as

$$I = e\frac{\Gamma^L_{0\to -1}\Gamma^R_{-1\to 0}}{(\Gamma^L_{0\to -1} + \Gamma^R_{-1\to 0})}. \tag{3.36}$$

In the derivation of Eq. (3.36) we have assumed that the capacitance of the right junction is larger than the capacitance of the left junction, i.e, $C_R > C_L$.

Near the special point $C_R V \approx e/2$, where the current increases by a step at zero temperature, the height of the spike is simply given by the difference,

$$\mathrm{JMR}(C_R V = \frac{e}{2}, T \to 0) = 1 - \frac{R_L^{\mathrm{P}}}{R_L^{\mathrm{AP}}}. \tag{3.37}$$

At finite temperature, the height of the spikes depend on the temperature, the capacitances, and the resistances of the junctions. We also notice that spikes go up for cases 3.9(a) and 3.9(c) whereas spikes go down for cases 3.9(b) and 3.9(d). Cases 3.9(a) – 3.9(b) or cases 3.9(c) – 3.9(d) differ only by the exchange of the metals in the left and the right leads. In all the above cases we keep the resistance of the left junction for the parallel alignment fixed, $R_L^{\mathrm{P}} = 0.01(R_L^{\mathrm{P}} + R_R^{\mathrm{P}})$. By only exchanging the metals of the left and the right leads, we go from spikes which go up to spikes which go down and vice versa. The interchange of the spikes from up to down or down to up can be explained in the following way. At zero temperature, whenever the JMR obtained from Eq. (3.37) is greater than the height of the plateau [Eq. (3.35)], we see an up-spike [Figs. 3.9(a) and 3.9(c)], otherwise we see a down-spike [Figs. 3.9(b) and 3.9(d)]. Within Julliere's model [65], we should mention that to see the spikes, the left or the right metal should be of a different ferromagnetic material. When all three metals are of the same ferromagnetic materials, the steady state solution $\rho_n^0(t)$ is the same for parallel and antiparallel orientation of magnetizations since the solution depends only on the ratio of the left and the right resistances.

Comparing Figs. 3.9(a) – 3.9(b) with Figs. 3.9(c) – 3.9(d), we see that the variation of the JMR as a function of voltage is larger when one of the leads is

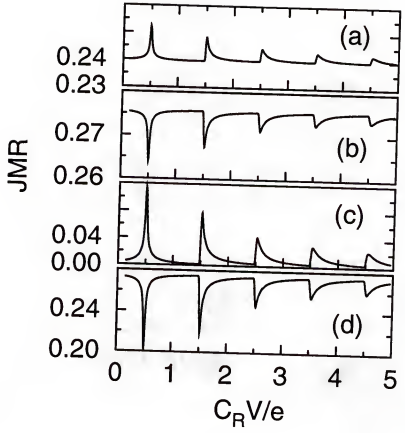

Figure 3.9: Junction magnetoresistance (JMR) as a function of voltage for different cases: (a) $FM_1/I/FM_1/I/FM_2$, (b) $FM_2/I/FM_1/I/FM_1$, (c) $FM_1/I/FM_1/I/PM$, and (d) $PM/I/FM_1/I/FM_1$, where FM_1 and FM_2 are two different ferromagnets, and PM is any paramagnet. In all cases we see spikes in the JMR: spikes go up for cases (a) and (c) whereas spikes go down for cases (b) and (d). These spikes occur at those places where the current increases by a step [see Fig. 3.6(b)]. The plateaus in all cases are given by the difference in the total resistances from antiparallel to parallel alignments divided by the total resistance for the antiparallel alignment. As a function of voltage the variation of JMR is larger when one of the end metals is a paramagnet (cases c and d). For our plots we consider the ferromagnet FM_1 to be of iron, and FM_2 is of cobalt. The parameters chosen are the same as in Fig. 3.6.

non-magnetic. Following Eq. (3.35) and Eq. (3.37), which give the height of the plateau and the height of the first spike at zero temperature, we see that the height of the plateau for case (c) is lower than for case (a). On the other hand, the heights of the first spikes are the same for both cases because the metals in the left and the center are same. Thus the variation of the JMR for case (c) is more than case (a). Cases (b) and (d) can be understood similarly.

We plot the differential junction magnetoresistance as a function of the voltage in Fig. 3.10 for the same cases as in Fig. 3.9 and in the same parameter regime. Many of the features of the DJMR are the same as for the JMR. The spikes are at the same places. The height of the spikes is also the same as in Eq. (3.37). The DJMR at large voltages is the same as in Eq. (3.37). The DJMR at large voltages is obtained from the classical value with two resistors in series. Finally, the variation of the DJMR with the voltage is larger in cases 3.10(c) and 3.9(d) than in cases 3.9(a) and 3.9(b). There are, however, some differences. The DJMR can be negative, as shown in Fig. 3.9(c), while the JMR must be positive from Eq. (3.37) as long as $R_L^{\rm P} < R_L^{\rm AP}$ and $C_R > C_L$. Also, comparing Fig. (3.9) with Fig. (3.10), we see that the variation of DJMR as a function of voltage is larger than the variation of the JMR with the voltage.

3.3 Conclusion

We have studied the magnetoresistance for double tunnel junctions with magnetic metals in the Coulomb blockade regime. For both the parallel and antiparallel orientations of the magnetizations, the steps in the current and the oscillations in the total conductance are observed. Also with increase in temperature the struc-

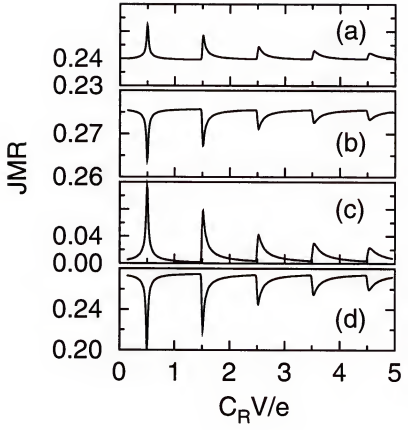

Figure 3.10: Differential Junction magnetoresistance (DJMR) as a function of voltage for the same cases as in Fig. 3.9. We see spikes in the DJMR at those places where the current increases by a step. As in Fig. 3.9, the variation in the DJMR is larger as a function of voltage for cases (c) and (d) compared to cases (a) and (b). For case (c) the DJMR changes sign. Also compared to Fig. 3.9, the change in the DJMR is larger than the JMR. The metals are the same as used in Fig. 3.9 and the parameters are identical to Fig. 3.6.

ture is reduced. These are expected in the Coulomb blockade regime. The JMR as a function of voltage shows spikes at the same places where the current increases by a step. Although the height of the spikes in general depends on the temperature, capacitances, and the resistances of the system the the height of the plateaus in the JMR vs. voltage curves are given by the classical value obtained by adding two resistors in series. For asymmetric junctions where $C_R > C_L$, the spikes go up if the ratio of the resistances of the right junction for parallel and antiparallel alignment ($R_R^{\mathrm{P}}/R_R^{\mathrm{AP}}$) is greater than the same ratio of the resistances of the left junction ($R_L^{\mathrm{P}}/R_L^{\mathrm{AP}}$). Otherwise, the spikes go down.

Many of the features of the DJMR are similar to the JMR: the spikes occur at the same places, the height of the first spike at zero temperature is the same, and the sign (up or down) of the spikes are the same. Also at high bias, the DJMR saturates to the classical value obtained by adding two resistors in series. However, there are few differences. The DJMR can be negative for some cases, while the JMR is positive as long as $R_L^{\mathrm{P}} < R_L^{\mathrm{AP}}$ and $C_R > C_L$. Finally, the variation of the DJMR is larger as a function of voltage than that of the JMR .

Thus double tunnel junction systems which have magnetic metals exhibit rich Coulomb blockade conductance vs. voltage curves. These curves provide a signature of both the Coulomb charging effects and the spin polarization of the tunneling. By measuring the magnetoresistance, one can extract information about both the capacitance charging energies and the spin polarization of the tunneling electrons. Hence theories of spin polarized tunneling and the Coulomb blockade both can be tested. Furthermore, there are cases where the magnetoresistance can

be dramatically enhanced near one of the Coulomb blockade steps, meaning that there may be some applications of these effects in electronic devices of the future.

CHAPTER 4
MAGNETIZATION REVERSAL IN SINGLE-DOMAIN THIN FILMS BY EXTERNAL ELECTRIC FIELD

Magnetization reversal in thin-films by applying a magnetic field is a well-known fact. This phenomenon has been widely used in industry. But the idea that it may be possible to change the magnetization by applying an external electric field in some spin-ordered materials was due to Landau and Lifshitz [171]. This effect is named the magnetoelectric (ME) effect and has been discussed in Section 1.3 of Chapter 1. The ME effect in single-domain ferromagnetic thin films is rather new. We propose that it is indeed possible that an electric field can change the magnetic surface anisotropy of a thin film which thereby changes the magnetization direction. The role of magnetic surface anisotropy also has been discussed in the introduction. To show the effect of the electric field on the surface anisotropy we do a simple atomic calculation which serves as a motivation and also sets the stage for studying real systems. In real systems (thin films of transition metals) the applied electric field will be screened within a layer. For real systems one also has to include the details of the band-structure of the materials [199, 200, 201].

4.1 Effect of Electric Field on Magnetic Anisotropy – An Atomic Calculation

We begin with a simple atomic calculation to evaluate the magnetic surface anisotropy for a single atom (of Fe, Co, and Ni). The Hamiltonian consists of three

parts: H_0 which is the unperturbed part of the Hamiltonian, $H_{\rm LS}$ which contains the spin-orbit coupling term, and $U_{\rm appl}$ which is due to the external electric field.

$$H = H_0 + H_{\rm LS} + U_{\rm appl}. \tag{4.1}$$

The spin-orbit part of the Hamiltonian is

$$H_{\rm LS} = g\mathbf{L}\cdot\mathbf{S}, \tag{4.2}$$

where g is the local spin-orbit coupling constant.

The part of the Hamiltonian due to the applied electric field (along the z direction) is:

$$U^{\rm appl} = |e|\mathcal{E}z. \tag{4.3}$$

To construct the full Hamiltonian matrix H the basis functions are the orthonormal atomic orbitals $|\mu\sigma>$ where μ denotes one of the atomic orbital and σ is the spin $(=\uparrow,\downarrow)$. The atomic orbitals are the $3d$ subbands which are $yz, zx, xy, d_1 = (x^2-y^2), d_2 = (3z^2-r^2)$, the $4s$ orbital, and the $4p$ orbitals p_x, p_y, and p_z. x, y, z refer to the standard axes and the spin quantization is along an axis z' characterized by the standard angular co-ordinates θ and ϕ. They are shown in Fig. 4.1.

The atomic wave functions for different orbitals are:

<u>$3d$ orbitals:</u>

$$d_{yz} = \sqrt{\frac{15}{4\pi}} f(r)\sin\theta\cos\theta\sin\phi, \tag{4.4}$$

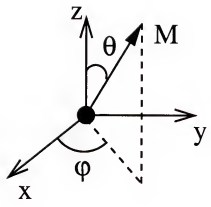

Figure 4.1: Pictorial representation of the angles. Magnetization (M) makes an angle θ with the z axis. Due to azimuthal symmetry, the magnetization and the total energy do not depend on the angle ϕ.

$$d_{xz} = \sqrt{\frac{15}{4\pi}} f(r) \sin\theta \cos\theta \cos\phi, \tag{4.5}$$

$$d_{xy} = \sqrt{\frac{15}{4\pi}} f(r) \sin^2\theta \sin\phi \cos\phi, \tag{4.6}$$

$$d_{x^2-y^2} = \sqrt{\frac{15}{16\pi}} f(r) \sin^2\theta \cos 2\phi, \tag{4.7}$$

$$d_{3z^2-r^2} = \sqrt{\frac{5}{16\pi}} f(r)(3\cos^2\theta - 1), \tag{4.8}$$

4s orbital:

$$s = \sqrt{\frac{1}{4\pi}} g(r), \tag{4.9}$$

4p orbitals:

$$p_x = \sqrt{\frac{3}{4\pi}} h(r) \sin\theta \cos\phi, \tag{4.10}$$

$$p_y = \sqrt{\frac{3}{4\pi}} h(r) \sin\theta \sin\phi, \tag{4.11}$$

$$p_z = \sqrt{\frac{3}{4\pi}} h(r) \cos\theta, \tag{4.12}$$

where $f(r), g(r)$, and $h(r)$ are radial part of the orbitals and they are normalized as

$$\int dr r^2 [f(r)]^2 = 1, \tag{4.13}$$

$$\int dr r^2 [g(r)]^2 = 1, \tag{4.14}$$

$$\int dr r^2 [h(r)]^2 = 1. \tag{4.15}$$

Using the atomic wave functions in Eqs. (4.4) – (4.12) the spin-orbit matrix elements $< \mu\sigma|\mathbf{L}\cdot\mathbf{S}|\nu\sigma' >$ can be obtained. In matrix notation the Hamiltonian in Eq. (4.2) takes the following form:

$$H_{\rm LS} = \begin{bmatrix} H_{\rm LS}^{\uparrow\uparrow} & H_{\rm LS}^{\uparrow\downarrow} \\ H_{\rm LS}^{\downarrow\uparrow} & H_{\rm LS}^{\downarrow\downarrow} \end{bmatrix} \equiv \begin{bmatrix} \mathbf{M} & \mathbf{N} \\ -\mathbf{N}^* & \mathbf{M}^* \end{bmatrix}. \tag{4.16}$$

The matrix elements of $\mathbf{M}$ and $\mathbf{N}$ are given in the Appendix A. Similarly the matrix elements for $U^{\rm appl}$ are calculated and they are also given in Appendix B.

We now diagonalize the 18×18 matrix, fill up the states using Hund's rule [202] and obtain the total energy of the filled states ($\rm E_{tot}$). In the absence of electric field (crystal or applied) our atomic Hamiltonian in Eq. (4.1) is rotationally invariant – thus there is no preferential direction for the magnetization. By applying an electric field we partially break the rotational symmetry (the azimuthal symmetry is not broken) and the magnetization then prefers to be in a particular direction. To mention that in real systems even in the absence of the applied electric field the magnetization has a preferred direction. For our simple atomic calculation in the presence of the applied field the total energy depends only on the angle θ.

The change in the total energy of the system is calculated by calculating the total energy of the system for two cases: one with the electric field and the other without the electric field. The difference of these two is the change in energy due the electric field.

$$\triangle E = E_{\rm tot}(\mathcal{E}) - E_{\rm tot}(\mathcal{E}=0). \tag{4.17}$$

The different input parameters of our problem are the ground state energies for the s, p and d atomic orbitals ($E_s, E_p, E_d^{\uparrow}, E_d^{\downarrow}$) [203], the exchange energies ($\triangle$) between up and down spin d-shell conduction electrons [147], the spin-orbit coupling parameter (g) [164], the atomic spacing (a) [199], and the two unknown parameters (p and q) which are the overlaps of the radial parts of the $3d$ with $4s$ and $4p$ orbitals.

$$p = \int dr r^3 f(r) g(r), \tag{4.18}$$

$$q = \int dr r^3 h(r) g(r). \tag{4.19}$$

To get an estimate of the parameters p and q we use the one electron atom radial wave-functions [202, 204]

$$g(r) = 2\left(\frac{Z}{3a_B}\right)^{3/2}\left[1-\left(\frac{2Zr}{3a_B}\right)+2\left(\frac{Zr}{3\sqrt{3}a_B}\right)^2\right]e^{-Zr/3a_B}, \tag{4.20}$$

$$h(r) = \frac{4\sqrt{2}}{3}\left(\frac{Z}{3a_B}\right)^{3/2}\left(\frac{Zr}{3a_B}\right)\left[1-\left(\frac{Zr}{6a_B}\right)\right]e^{-Zr/3a_B}, \tag{4.21}$$

$$f(r) = \frac{2\sqrt{2}}{3\sqrt{5}}\left(\frac{Z}{3a_B}\right)^{3/2}\left(\frac{Zr}{3a_B}\right)^2 e^{-Zr/3a_B}, \tag{4.22}$$

where Z is the atomic number and a_B is the Bohr radius. Using Eqs. (4.20 - 4.22), Eqs. (4.18) and (4.19) yield after integration

$$p = \sqrt{10}\left(\frac{Z}{3a_B}\right)^{-1}, \tag{4.23}$$

$$q = -3\sqrt{2}\left(\frac{Z}{3a_B}\right)^{-1}. \tag{4.24}$$

We calculate the anisotropy energy for Fe, Co, and Ni atoms. The different parameters chosen are listed in Table 4.1.

Table 4.1: Different Input Parameters

Element	E_s(eV)	E_p(eV)	$E_d^{\uparrow}$(eV)	$E_d^{\downarrow}$(eV)	$\triangle$(eV)	g(eV)	a(Å)
Fe	-7.95	-5.51	-7.02	-5.22	1.8	0.075	2.861
Co	-8.37	-5.38	-7.40	-6.40	1.0	0.085	3.281
Ni	-8.80	-5.48	-8.70	-8.20	0.5	0.105	3.523

To show how the energy varies with the electric field we plot the change in the energy of a Fe atom in Fig. 4.2. The change in energy is negative and also varies quadratically with the field. Similar results are seen with Co and Ni atoms. The quadratic dependence with the electric field and the negative sign is also expected for the energy from second order perturbation theory.

The effect of the electric field on the anisotropy energy for Fe and Co atoms is shown in Fig. 4.3. For a fixed value of the electric field the change in the energy (considering only the anisotropy part $\triangle E$) is plotted as a function of cosine of the angle θ. The anisotropy energy takes the form:

$$\triangle E = K_1 \cos^2\theta + K_2 \cos^4\theta + ... \tag{4.25}$$

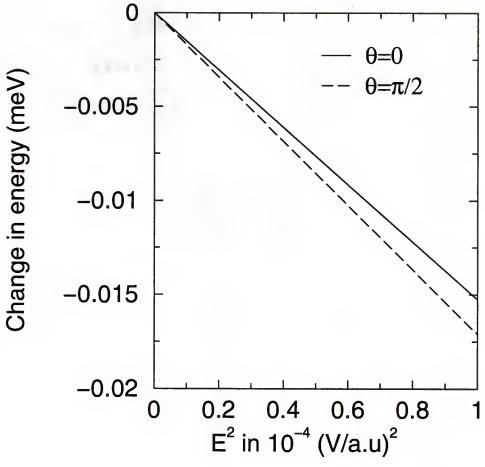

Figure 4.2: Change in the total energy of a Fe atom due to the electric field $[\Delta E_T = E(\mathcal{E}, \theta) - E(\mathcal{E} = 0, \theta)]$ is plotted as a function of square of the field for two different values of the angle $\theta = 0$ and $\pi/2$. The applied field is in volts (V)/atomic unit (a.u). The change in energy is negative and scales quadratically with the field.

The anisotropy constants K_1 and K_2 depend on the spin-orbit coupling parameter

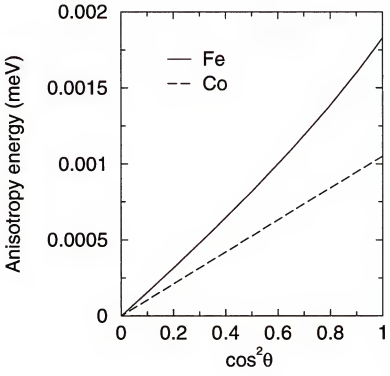

Figure 4.3: The anisotropy energy as a function of $\cos^2\theta$ for Fe and Co atoms. In all two cases the energy is minimum for $\theta = 0$ which implies that the electric field prefers the magnetization to be perpendicular to the $x-y$ plane. The electric field is fixed to $\mathcal{E} = 0.01$ V/a.u in our calculation for all cases.

and also on the electric field. K_2 is at least an order of magnitude smaller than K_1. The anisotropy energy is minimum when $\theta = 0$ – thus the anisotropy energy due to electric field and spin-orbit coupling prefers the magnetization to be perpendicular to the $x-y$ plane (See Fig. 4.1).

On the other hand, for Ni atom the anisotropy energy due to the electric field and spin-orbit coupling is minimum for $\theta = \pi/2$. Magnetization in this case prefers to be in the $x-y$ plane. This is shown in Fig. 4.4.

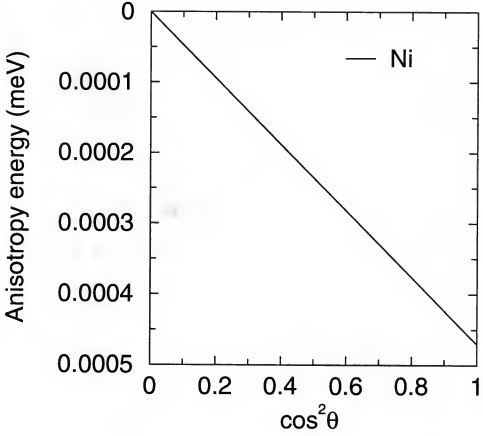

Figure 4.4: The anisotropy energy as a function of $\cos^2\theta$ for a Ni atom. In this case the energy is minimum for $\theta = \pi/2$. The electric field thus prefer the magnetization to be in the $x-y$ plane. The electric field is fixed to the same value as in Fig. 4.3
.

4.2 Conclusion

This simple atomic calculation shows that the electric field can indeed effect the magnetization. As mentioned in Section 1.3 of Chapter 1, for real magnetic systems (thin films of transition metals) the magnetization can be perpendicular to the plane (for bcc Fe 001) or in-plane (for Co and Ni films). For bcc Fe films larger than five monolayers a transition from perpendicular to in-plane has been seen experimentally [140, 141]. Our atomic calculation shows that it may be possible to control the transition by applying an external electric field. This new phenomenon holds the promise of being applied in the future recording devices.

CHAPTER 5
CONCLUSION

In this thesis I studied transport properties of three different types of nanostructures: laterally confined magnetic multilayers (Chapter 2), double-tunnel-junctions made with magnetic metals (Chapter 3), and thin ferromagnetic films (Chapter 4). This chapter will review the major results obtained and provide suggestions for future theoretical work.

5.1 GMR in Laterally Confined Magnetic Multilayers

In magnetic multilayers I studied the effect of lateral confinement on the giant magnetoresistance (GMR) in the current-in-plane geometry. GMR decreases as we decrease the width of the wire for spin-independent specularity factors at the sides of the wires. This reduction in GMR can be understood in terms of the reduction in the effective mean free path in the layers due to scattering at the sides of the wires. The length scale where the GMR decreases depends on both the mean-free paths and the thickness of the films. With spin-dependent specularity factors at the sides I find that there are parameter regimes where GMR can increase with lateral confinement.

5.2 JMR in Tunnel Junctions with Magnetic Metals

Tunnel junctions made with magnetic metals exhibit both the effects of spin-polarized tunneling and the phenomenon of the Coulomb blockade. The purpose of my study was to investigate in the Coulomb blockade regime the current, conductance, and the junction magnetoresistance (JMR) in double-tunnel junctions made with magnetic metals. I find that the current-voltage characteristic curves show a stair-case structure as expected at low voltage and low temperatures (the Coulomb blockade regime), the conductance curves show oscillations which eventually saturate with increasing voltage. On the other hand, the JMR as a function of voltage exhibits spikes – the spikes may go up or may go down depending on the magnetic material in the leads. The spikes occur at those places where the current increases by a step. At large voltages (Ohmic region) no spikes are seen in the JMR vs. voltage curves.

Recently the effect of barrier impurity atoms on the magnetoresistance of ferromagnetic tunnel junctions has been investigated [205]. A submonolayer amounts of Co, Pd, Cu, or Ni is incorporated into the middle of the insulating oxide of $Co/Al_2O_3/Ni_{80}Fe_{20}$ junctions. It has been observed that the JMR decays approximately linearly with increasing impurity content (except for Co at 300 K in Fig. 5.1b). The slope depends sensitively on the type of element but the decrease of JMR is much more pronounced in case of Ni impurities. This is shown in Fig. 5.1. Nevertheless the shape of the JMR curves remains practically unchanged. For Ni impurities this is illustrated in Fig. 5.2. Although spin-flip scattering may be a reason for such a decrease of JMR with impurity thickness for most cases but

(a)

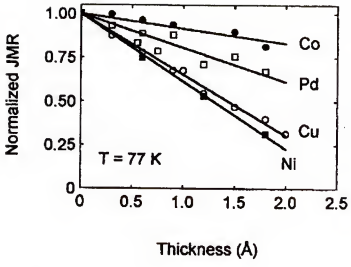

(b)

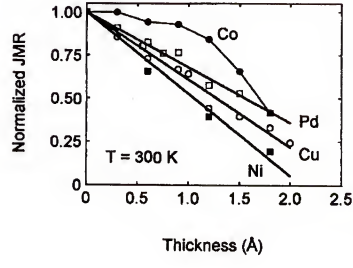

Figure 5.1: Normalized JMR as a function of the thickness of the layer of impurities present in the tunneling barrier [205] at two different temperatures (a) 77 K and (b) 300 K. JMR approximately decreases linearly with the thickness. In case of Co at 300 K we note a clear deviation from a linear fit.

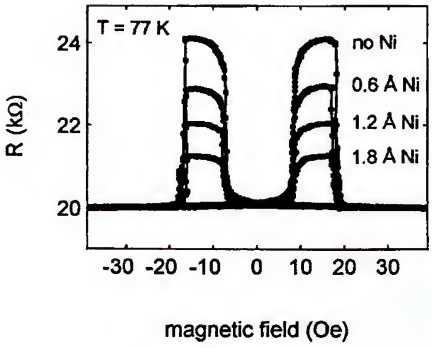

Figure 5.2: Magnetoresistance curves for tunnel junctions for different layers of Ni impurities at 77 K [205]. The shape of the JMR curves remains practically unchanged with the thickness of Ni impurities.

it fails to explain the results for Co at 300 K. A fully satisfactory theory is still lacking.

5.3 Magnetocrystalline Anisotropy in Thin Magnetic Films

Magnetocrystalline anisotropy originates due to the coupling between the spin and the angular momentum of the electrons. At the surface of the thin films the anisotropy is much more pronounced than the bulk. This is known as the surface anisotropy and has been under intense investigation recently by both theorists and experimentalists. Applying an electric field in these thin films can change the surface anisotropy and thus change the magnetization. In Chapter 4 with a simple atomic calculation I showed the effect of the electric field on the anisotropy. Band-structure calculations for real systems are needed to get quantitative values for the anisotropy. For thin films of transition metals magnetic moment is enhanced at the surface than the bulk. Thus, one can also investigate the relationship between the surface magnetic moment with the surface anisotropy.

A new interesting phenomena may be associated with thin magnetic films. Pressure-induced quantum phase transition in heavy-fermion metals has been reported [206, 207]. Quantum critical behavior of itinerant ferromagnets where a quantum phase transition from a ferromagnetic to a paramagnetic state occurs has also been studied theoretically [208]. If we can prepare a thin magnetic film near the critical regime then by applying a small electric field it may be possible to go from ferromagnetic to paramagnetic state. Applying an electric field changes the number density of electrons in each layer of the film which may lead to a quan-

tum phase transition. Experimental studies as well as theoretical investigations may unravel this interesting phenomenon.

APPENDIX A
THE SPIN-ORBIT COUPLING MATRIX ELEMENTS

As described in the text the spin-orbit part of the Hamiltonian for a monolayer is of the form:

$$H_{\text{mono}} = g \begin{bmatrix} \mathbf{M} & \mathbf{N} \\ -\mathbf{N}^* & \mathbf{M}^* \end{bmatrix}, \tag{A.1}$$

where $\mathbf{M}$ and $\mathbf{N}$ are 9×9 matrices and g is the constant spin-orbit coupling parameter.

The matrix elements for $\mathbf{M}$ are: ($d_1 = d_{x^2-y^2}$, $d_2 = d_{3z^2-r^2}$)

$$< p_x \uparrow |\mathbf{L} \cdot \mathbf{S}| p_z \uparrow > \; = \; \frac{i}{2} \sin\theta \sin\phi, \tag{A.2}$$

$$< p_x \uparrow |\mathbf{L} \cdot \mathbf{S}| p_y \uparrow > \; = \; -\frac{i}{2} \cos\theta, \tag{A.3}$$

$$< p_z \uparrow |\mathbf{L} \cdot \mathbf{S}| p_y \uparrow > \; = \; \frac{i}{2} \sin\theta \cos\phi, \tag{A.4}$$

$$< d_1 \uparrow |\mathbf{L} \cdot \mathbf{S}| d_{xz} \uparrow > \; = \; \frac{i}{2} \sin\theta \sin\phi, \tag{A.5}$$

$$< d_1 \uparrow |\mathbf{L} \cdot \mathbf{S}| d_{yz} \uparrow > \; = \; \frac{i}{2} \sin\theta \cos\phi, \tag{A.6}$$

$$< d_1 \uparrow |\mathbf{L} \cdot \mathbf{S}| d_{xy} \uparrow > \; = \; -i \cos\theta, \tag{A.7}$$

$$< d_{xz} \uparrow |\mathbf{L} \cdot \mathbf{S}| d_2 \uparrow > \; = \; \frac{\sqrt{3}i}{2} \sin\theta \sin\phi, \tag{A.8}$$

$$< d_{xz} \uparrow |\mathbf{L} \cdot \mathbf{S}| d_{yz} \uparrow > \; = \; -\frac{i}{2} \cos\theta, \tag{A.9}$$

$$< d_{xz} \uparrow |\mathbf{L} \cdot \mathbf{S}| d_{xy} \uparrow > \; = \; \frac{i}{2} \sin\theta \cos\phi, \tag{A.10}$$

$$< d_2 \uparrow |\mathbf{L} \cdot \mathbf{S}| d_{yz} \uparrow > \; = \; \frac{\sqrt{3}i}{2} \sin\theta \cos\phi, \tag{A.11}$$

$$< d_{yz} \uparrow |\mathbf{L}\cdot\mathbf{S}| d_{xy} \uparrow > \;=\; -\frac{i}{2}\sin\theta\sin\phi. \tag{A.12}$$

Other non-zero matrix elements of $\mathbf{M}$ are obtained by taking the complex conjugate:

$$< \beta \uparrow |\mathbf{L}\cdot\mathbf{S}| \alpha \uparrow > = [< \alpha \uparrow |\mathbf{L}\cdot\mathbf{S}| \beta \uparrow >]^{*}. \tag{A.13}$$

The matrix elements for $\mathbf{N}$ are:

$$< p_x \uparrow |\mathbf{L}\cdot\mathbf{S}| p_z \downarrow > \;=\; \frac{1}{2}(\cos\phi + i\sin\phi\cos\theta), \tag{A.14}$$

$$< p_x \uparrow |\mathbf{L}\cdot\mathbf{S}| p_y \downarrow > \;=\; \frac{i}{2}\sin\theta, \tag{A.15}$$

$$< p_z \uparrow |\mathbf{L}\cdot\mathbf{S}| p_y \downarrow > \;=\; -\frac{1}{2}(\sin\phi - i\cos\theta\cos\phi), \tag{A.16}$$

$$< d_1 \uparrow |\mathbf{L}\cdot\mathbf{S}| d_{xz} \downarrow > \;=\; \frac{1}{2}(\cos\phi + i\cos\theta\sin\phi), \tag{A.17}$$

$$< d_1 \uparrow |\mathbf{L}\cdot\mathbf{S}| d_{yz} \downarrow > \;=\; -\frac{1}{2}(\sin\phi - i\cos\theta\cos\phi), \tag{A.18}$$

$$< d_1 \uparrow |\mathbf{L}\cdot\mathbf{S}| d_{xy} \downarrow > \;=\; i\sin\theta, \tag{A.19}$$

$$< d_{xz} \uparrow |\mathbf{L}\cdot\mathbf{S}| d_2 \downarrow > \;=\; \frac{\sqrt{3}g}{2}(\cos\phi + i\sin\phi\cos\theta), \tag{A.20}$$

$$< d_{xz} \uparrow |\mathbf{L}\cdot\mathbf{S}| d_{yz} \downarrow > \;=\; \frac{i}{2}\sin\theta, \tag{A.21}$$

$$< d_{xz} \uparrow |\mathbf{L}\cdot\mathbf{S}| d_{xy} \downarrow > \;=\; -\frac{1}{2}(\sin\phi - i\cos\theta\cos\phi), \tag{A.22}$$

$$< d_2 \uparrow |\mathbf{L}\cdot\mathbf{S}| d_{yz} \downarrow > \;=\; -\frac{\sqrt{3}g}{2}(\sin\phi - i\cos\phi\cos\theta), \tag{A.23}$$

$$< d_{yz} \uparrow |\mathbf{L}\cdot\mathbf{S}| d_{xy} \downarrow > \;=\; -\frac{1}{2}(\cos\phi + i\cos\theta\sin\phi). \tag{A.24}$$

Other non-zero matrix elements of $\mathbf{N}$ are obtained by

$$< \beta \uparrow |\mathbf{L}\cdot\mathbf{S}| \alpha \downarrow > = - < \alpha \uparrow |\mathbf{L}\cdot\mathbf{S}| \beta \downarrow > . \tag{A.25}$$

APPENDIX B
ELECTRIC FIELD MATRIX ELEMENTS

The part of the Hamiltonian which depends on the electric field is:

$$U^{\text{appl}} = |e|\mathcal{E}z. \tag{B.1}$$

The matrix elements are calculated using the atomic orbitals given in Eqs. (4.4) – (4.12). The matrix elements also do not depend on spin of the electrons, i.e.

$$< \alpha \uparrow |e\mathcal{E}z|\beta \uparrow > \;=\; < \alpha \downarrow |e\mathcal{E}z|\beta \downarrow >, \tag{B.2}$$

$$< \alpha \uparrow |e\mathcal{E}z|\beta \downarrow > \;=\; < \alpha \downarrow |e\mathcal{E}z|\beta \uparrow > = 0. \tag{B.3}$$

and they are:

$$< s|e\mathcal{E}z|p_z > = < p_z|e\mathcal{E}z|s > \;=\; \sqrt{\frac{5}{15}}e\mathcal{E}q, \tag{B.4}$$

$$< d_{yz}|e\mathcal{E}z|p_y > = < p_y|e\mathcal{E}z|d_{yz} > \;=\; \sqrt{\frac{3}{15}}e\mathcal{E}p, \tag{B.5}$$

$$< d_{xz}|e\mathcal{E}z|p_x > = < p_x|e\mathcal{E}z|d_{xz} > \;=\; \sqrt{\frac{3}{15}}e\mathcal{E}p, \tag{B.6}$$

$$< d_2|e\mathcal{E}z|p_z > = < p_z|e\mathcal{E}z|d_2 > \;=\; \sqrt{\frac{4}{15}}e\mathcal{E}p, \tag{B.7}$$

where the two unknown parameters p and q are overlaps of the radial parts of the $3d$ with $4s$ and $4p$ orbitals.

$$p = \int dr r^3 f(r) g(r), \tag{B.8}$$

$$q = \int dr r^3 h(r) g(r). \tag{B.9}$$

REFERENCES

[1] F. J. Himpsel, J. E. Ortega, G. J. Mankey, and R. F. Willis. Magnetic nanostructures. *Adv. Phys.*, 47(4):511, 1998.

[2] Y. Imry. *Introduction to Mesoscopic Physics.* Oxford, New York, 1997.

[3] S. von Molnar and S. Methfessel. Giant Negative Magnetoresistance in ferromagnetic $Eu_{1-x}Gd_xSe$. *J. Appl. Phys.*, 38(3):959, 1967.

[4] H. Sato, P. A. Schroeder, J. Slaughter, W. P. Pratt Jr., and W. Abdul-Razzaq. Galvanomagnetic properties of Ag/M (M = Fe, Ni, Co) layered metallic films. *Superlattices Microstruct.*, 4:45, 1988.

[5] E. Velu, C. Dupas, D. Renard, J. P. Renard, and J. Seiden. Enhanced magnetoresistance of ultrathin $(Au/Co)_n$ multilayers with perpendicular anisotropy. *Phys. Rev. B*, 37:668, 1988.

[6] M. N. Baibich, J. M. Broto, A. Fert, F. Nguyen Van Dau, F. Petroff, P. Etienne, G. Creuzet, A. Friederich, and J. Chazelas. Giant magnetoresistance of (001)Fe/(001)Cr magnetic superlattices. *Phys. Rev. Lett.*, 61:2472, 1988.

[7] A. Barthélémy, A. Fert, M. N. Baibich, S. Hadjoudj, F. Petroff, P. Etienne, R. Cabanel, S. Lequien, and G. Creuzet. Magnetic and transport properties of Fe/Cr superlattices. *J. Appl. Phys.*, 67:5908, 1990.

[8] E. E. Fullerton, M. J. Conover, J. E. Mattson, C. H. Sowers, and S. D. Bader. 150% magnetoresistance in sputtered Fe/Cr(100) superlattices. *Appl. Phys. Lett.*, 63:1699, 1993.

[9] S. S. P. Parkin, R. Bhadra, and K. P. Roche. Oscillatory magnetic exchange coupling through thin copper layers. *Phys. Rev. Lett.*, 71:1641, 1991.

[10] S. S. P. Parkin. Systematic variation of the strength and oscillation period of indirect magnetic exchange coupling through the 3d, 4d, and 5d transition metals. *Phys. Rev. Lett.*, 67:3598, 1991.

[11] S. S. P. Parkin. In B. Heinrich and J. A. C. Bland, editors, *Ultrathin Magnetic Structures II*, New York, 1995. Springer-Verlag. Chapter 2.2, Vol 48, page 148.

[12] K. B. Hathaway. In B. Heinrich and J. A. C. Bland, editors, *Ultrathin Magnetic Structures II*, New York, 1995. Springer-Verlag. Chapter 2.1, Vol 48, page 45.

[13] F. Petroff, A. Barthélémy, A. Hamzić, A. Fert, P. Etienne, S. Lequien, and G. Creuzet. Magnetoresistance of Fe/Cr superlattices. *J. Magn. Magn. Mater.*, 93:95, 1991.

[14] E. E. Fullerton, D. M. Kelly, J. Guimpel, I. K. Schuller, and Y. Bruynseraede. Roughness and giant magnetoresistance in Fe/Cr superlattices. *Phys. Rev. Lett.*, 68:859, 1992.

[15] W. P. Pratt Jr., S. F. Lee, J. M. Slaughter, R. Loloee, P. A. Schroeder, and J. Bass. Perpendicular giant magnetoresistances of Ag/Co multilayers. *Phys. Rev. Lett.*, 66:3060, 1991.

[16] W. P. Pratt Jr., S. F. Lee, Q. Yang, D. Holody, R. Loloee, P. A. Schroeder, and J. Bass. Giant magnetoresistance with current perpendicular to the layer planes of Ag/Co and AgSn/Co multilayers. *J. Appl. Phys.*, 73:5326, 1993.

[17] P. M. Levy. *Solid State Physics*, volume 47, page 367. Academic Press, San Diego, 1994.

[18] A. Fert. Magnetic and transport properties of metallic multilayers. *Materials Science Forum*, 59:439, 1990.

[19] A. Fert and P. Bruno. In B. Heinrich and J. A. C. Bland, editors, *Ultrathin Magnetic Structures II*, New York, 1995. Springer-Verlag. Chapter 2.2, Vol 48, page 82.

[20] X.-G. Zhang and W. H. Butler. Conductivity of metallic films and multilayers. *Phys. Rev. B*, 51:10 085, 1995.

[21] K. Fuchs. The conductivity of thin metallic films according to the electron theory of metals. *Proc. Camb. Philos. Soc.*, 34:100, 1938.

[22] E. H. Sondheimer. The mean free path of electrons in metals. *Adv. Phys.*, 1:1, 1952.

[23] R. E. Camley and J. Barnaś. Theory of giant magnetoresistance effects in magnetic layered structures with antiferromagnetic coupling. *Phys. Rev. Lett.*, 63:664, 1989.

[24] J. Barnaś, A. Fuss, R. E. Camley, P. Grünberg, and W. Zinn. Layered magnetic structures: magnetoresistance due to antiparallel alignment. *Phys. Rev. B*, 42:8110, 1990.

[25] M. Liu and D. Y. Xing. Analytical approach to the Camley-Barnaś theory for giant magnetoresistance in magnetic layered structures. *Phys. Rev. B*, 47:12 272, 1993.

[26] G. Binasch, P. Grünberg, F. Saurenbach, and W. Zinn. Enhanced magnetoresistance in layered magnetic structures with antiferromagnetic interlayer exchange. *Phys. Rev. B*, 39:4828, 1989.

[27] A. Barthélémy and A. Fert. Theory of the magnetoresistance in magnetic multilayers: analytical expressions from a semiclassical approach. *Phys. Rev. B*, 43:13 124, 1991.

[28] D. M. Edwards, R. B. Muniz, and J. Mathon. A resistor network theory of the giant magnetoresistance in magnetic superlattices. *IEEE Trans. Magn.*, 27:3548, 1991.

[29] B. L. Johnson and R. E. Camley. Theory of giant magnetoresistance effects in Fe/Cr multilayers: spin-dependent scattering from impurities. *Phys. Rev. B*, 44:9997, 1991.

[30] R. Q. Hood and L. M. Falicov. Boltzmann-equation approach to the negative magnetoresistance of ferromagnetic-normal-metal multilayers. *Phys. Rev. B*, 46:8287, 1992.

[31] T. Valet and A. Fert. Theory of the perpendicular magnetoresistance in magnetic multilayers. *Phys. Rev. B*, 48:7099, 1993.

[32] T. Valet and A. Fert. Classical theory of perpendicular giant magnetoresistance in magnetic multilayers. *J. Magn. Magn. Mater.*, 121:378, 1993.

[33] Z. Tešanovic, M. Jarić, and S. Maekawa. Quantum transport and surface scattering. *Phys. Rev. Lett.*, 57:2760, 1986.

[34] M. Buttiker. Symmetry of electrical conduction. *IBM J. Res. Dev.*, 32:317, 1988.

[35] H. E. Camblong and P. M. Levy. Novel results for quasiclassical linear transport in metallic multilayers. *Phys. Rev. Lett.*, 69:2835, 1992.

[36] H. E. Camblong and P. M. Levy. Magnetic multilayers: quasiclassical transport via the Kubo formula. *J. Appl. Phys.*, 73:5533, 1993.

[37] P. M. Levy and S. Zhang. Electrical conductivity of magnetic multilayered structures. *Phys. Rev. Lett.*, 65:1643, 1990.

[38] S. Zhang, P. M. Levy, and A. Fert. Conductivity and magnetoresistance of magnetic multilayered structures. *Phys. Rev. B*, 45:8689, 1992.

[39] H. E. Camblong. Linear transport theory of magnetoconductance in metallic multilayers: a real-space approach. *Phys. Rev. B*, 51:1855, 1995.

[40] G. E. Bauer. Perpendicular transport through magnetic multilayers. *Phys. Rev. Lett.*, 69:1676, 1992.

[41] A. Fert. In G. C. Hadjipanayis and G. A. Prinz, editors, *Science and Technology of Nanostructured Magnetic Materials*, London, 1991. Plenum. page 221.

[42] D. S. Fisher and P. A. Lee. Relation between conductivity and transmission matrix. *Phys. Rev. B*, 23:6851, 1981.

[43] P. B. Visscher. Transport in magnetic multilayers from the quantum Boltzmann equation. *Phys. Rev. B*, 49:3907, 1994.

[44] I. Mertig, P. Zahn, M. Richter, H. Eschrig, R. Zeller, and P. H. Dederichs. Ab initio calculation of residual resistivity in dilute Fe alloys and giant magnetoresistance in Fe/Cr multilayers. *J. Magn. Magn. Mater.*, 151:363, 1995.

[45] R. Coehoorn. Relation between interfacial magnetism and spin-dependent scattering at non-ideal Fe/Cr and Fe/V interfaces. *J. Magn. Magn. Mater.*, 151:341, 1995.

[46] H. J. F. Jansen. Electronic structure calculations for magnetically ordered systems. *Phys. Today*, 48:50, 1995.

[47] C. Blaas, P. Weinberger, L. Szunyogh, P. M. Levy, and C. B. Sommers. Ab-initio calculations of magnetotransport for magnetic multilayers. 1998. Unpublished.

[48] J. C. Mallinson. *Magneto-Resistive Heads - Fundamentals and Applications.* Academic Press, San Diego, California, 1996.

[49] J. E. Lenz. A review of magnetic sensors. *Proc. IEEE*, 78(6):973, 1990.

[50] R. L. White. Giant Magnetoresistance: A Primer. *IEEE Trans. Magn.*, 28:2482, 1992.

[51] J. Daughton and Y. J. Chen. GMR materials for low field applications. *IEEE Trans. Magn.*, 29:6, 1993.

[52] J. Brown. GMR materials: theory and applications. *Sensors*, 11(9):42, September 1994.

[53] J. Daughton. Magnetoresistive memory technology. *Thin Solid Films*, 216(1):162, 1992.

[54] A. V. Pohm, J. S. T. Huang, J. M. Daughton, D. R. Krahn, and V. Mehra. The design of a one megabit non-volatile M-R memory chip using 1.5*5μm cells. *IEEE Trans. Magn.*, 24(6):3117, 1988.

[55] Y. D. Park, J. A. Caballero, A. Cabbibo, J. R. Childress, H. D. Hudspeth, T. J. Schultz, and F. Sharifi. Fabrication of nanometer-sized magnetic structures using e-beam patterned deposition masks. *J. Appl. Phys.*, 81:4717, 1997.

[56] L. Piraux, S. Dubois, J. L. Duvail, K. Ounadjela, and A. Fert. Arrays of nanowires of magnetic metals and multilayers: Perpendicular GMR and magnetic properties. *J. Magn. Magn. Mater.*, 175:127, 1997.

[57] S. Dubois, J. L. Duvail, A. Fert, J. M. George, J. L. Maurice, and L. Piraux. Perpendicular giant magnetoresistance in Co/Cu and permalloy/Cu multilayered nanowires. *J. Appl. Phys.*, 81:4569, 1997.

[58] S. C. Sanders, R. W. Cross, S. E. Russek, A. Roshko, and J. O. Oti. Size effects and giant magnetoresistance in unannealed NiFe/Ag multilayer stripes. *J. Appl. Phys.*, 79:6240, 1996.

[59] M. Kume, A. Maeda, T. Tanuma, and K. Kuroki. Giant magnetoresistance effect in multilayered wire arrays. *J. Appl. Phys.*, 79:6402, 1996.

[60] M. Vazquez, M. Knobel, M. L. Sanchez, R. Valenzuela, and A. P. Zhukov. Giant magneto-impedance effect in soft magnetic wires for sensor applications. *Sens. Actuators A, Phys. (Switzerland)*, A59:20, 1997.

[61] K. Majumdar, J. Chen, and S. Hershfield. Calculation of giant magnetoresistance in laterally confined multilayers in the current-in-plane geometry. *Phys. Rev. B*, 57:2950, 1998.

[62] E. L. Wolf. *Principles of Tunneling Spectroscopy.* Clarendon Press, New York, 1969.

[63] P. M. Tedrow and R. Meservey. Spin-polarized electron tunneling. *Phys. Rep.*, 238:1714, 1994.

[64] C. B. Duke. *Tunneling in Solids.* Academic Press, New York, NY, 1969.

[65] M. Julliere. Tunneling between ferromagnetic films. *Phys. Lett.*, 54A:225, 1975.

[66] C. T. Tanaka, J. Nowak, and J. S. Moodera. Magnetoresistance in ferromagnet-insulator-ferromagnet tunnel junctions with half-metallic ferromagnet NiMnSb compound. *J. Appl. Phys.*, 81:5515, 1997.

[67] C. L. Platt, B. Dieny, and A. E. Berkowitz. Spin polarized tunneling in reactively sputtered tunnel junctions. *J. Appl. Phys.*, 81:5523, 1997.

[68] S. Maekawa and U. Gäfvert. Electron tunneling between ferromagnetic films. *IEEE Trans. Magn.*, 18:707, 1982.

[69] J. Nowak and J. Rauluszkiewicz. Spin dependent electron tunneling between ferromagnetic films. *J. Magn. Magn. Mater.*, 109:79, 1992.

[70] Y. Suezawa and Y. Gondo. Spin-polarized electrons and magnetoresistance in ferromagnetic tunnel junctions and multilayers. *J. Magn. Magn. Mater.*, 126:524, 1993.

[71] R. Nakatani and M. Kitada. Changes in the electrical resistivity of Fe-C/Al_2O_3/Fe-Ru multilayered films due to a magnetic field. *J. Mater. Sci. Lett.*, 10:827, 1991.

[72] T. S. Plaskett, P. P. Freitas, N. P. Barradas, M. F. da Silva, and J. C. Soares. Magnetoresistance and magnetic properties of NiFe/oxide/Co junctions prepared by magnetron sputtering. *J. Appl. Phys.*, 76:6104, 1994.

[73] P. LeClair, J. S. Moodera, and R. Meservey. Ferromagnetic-ferromagnetic tunneling and the spin filter effect. *J. Appl. Phys.*, 76:6546, 1994.

[74] T. Miyazaki, T. Yaoi, and S. Ishio. Large magnetoresistance effect in 82Ni-Fe/Al-Al_2O_3/Co magnetic tunneling junction. *J. Magn. Magn. Mater.*, 98:L7, 1991.

[75] T. Miyazaki and N. Tezuka. Giant magnetic tunneling effect in Fe/Al_2O_3/Fe junction. *J. Magn. Magn. Mater.*, 139(3):L231, 1995.

[76] T. Miyazaki and N. Tezuka. Spin polarized tunneling in ferromagnet/insulator/ferromagnet junctions. *J. Magn. Magn. Mater.*, 151:403, 1995.

[77] J. S. Moodera, L. R. Kinder, T. M. Wong, and R. Meservey. Large magnetoresistance at room temperature in ferromagnetic thin film tunnel junctions. *Phys. Rev. Lett.*, 79:4724, 1995.

[78] J. J. Sun, P. Freitas, and V. Soares. Low resistance spin-dependent tunnel juntions. *Appl. Phys. Lett.*, 79, 1998. To appear.

[79] R. A. de Groot, F. M. Mueller, P. G. van Engen, and K. H. J. Buschow. New class of materials: half-metallic ferromagnets. *Phys. Rev. Lett.*, 50:2024, 1983.

[80] J. A. Caballero, W. J. Geerts, F. Petroff, J. U. Thiele, D. Weller, and J. R. Childress. Magnetic and magneto-optical properties of NiMnSb thin films. *J. Magn. Magn. Mater.*, 177-181:1229, 1998.

[81] C. T. Tanaka and J. S. Moodera. Spin polarized tunneling in half-metallic ferromagnets. *J. Appl. Phys.*, 78:6265, 1996.

[82] C. J. Gorter. A possible explanation of the increase of the electrical resistance of thin metal films at low temperatures and small field strengths. *Physica*, 17(8):777, 1951.

[83] I. O. Kulik and R. I. Shekhter. Kinetic phenomena and charge discreteness effects in granulated media. *Sov. Phys. JETP*, 41:308, 1975.

[84] K. K. Likharev. Correlated discrete transfer of single electrons in ultrasmall tunnel junctions. *IBM J. Res. Dev.*, 32:144, 1988.

[85] D. V. Averin and K. K. Likharev. In B. Altshuler, editor, *Mesoscopic Phenomena in Solids*, New York, 1991. Elsevier.

[86] G. Schon and A. D. Zaikin. Quantum coherent effects, phase transitions, and the dissipative dynamics of ultra small tunnel junctions. *Phys. Rep.*, 198:237, 1990.

[87] In H. Grabert and M. Devoret, editors, *Single Charge Tunneling*, New York, 1992. Plenum, New York. Vol 294 of NATO Advanced Study Institute, Series B: Physics.

[88] D. C. Ralph, C. T. Black, and M. Tinkham. Gate-voltage studies of discrete electronic states in aluminum nanoparticles. *Phys. Rev. Lett.*, 78:4087, 1997.

[89] M. S. Raven. Charge transport and conductance oscillations in gold island films. *Phys. Rev. B*, 29:6218, 1984. and reference therein.

[90] A. E. Hanna and M. Tinkham. Variation of the Coulomb staircase in a two-junction system by fractional electron charge. *Phys. Rev. B*, 44:5919, 1991.

[91] D. C. Ralph, C. T. Black, and M. Tinkham. Spectroscopic measurements of discrete electronic states in single metal particles. *Phys. Rev. Lett.*, 74:3241, 1995.

[92] C. T. Black, D. C. Ralph, and M. Tinkham. Spectroscopy of the superconducting gap in individual nanometer-scale aluminum particles. *Phys. Rev. Lett.*, 76:688, 1996.

[93] D. A. Fulton and G. J. Dolan. Observation of single-electron charging effects in small tunnel junctions. *Phys. Rev. Lett.*, 59:109, 1987.

[94] H. Boeve, R. J. M. van de Veerdonk, B. Dutta, J. De Boeck, and J. S. Moodera. Area scaling of planar ferromagnetic tunnel junctions: From shadow evaporation to lithographic microfabrication. *J. Appl. Phys.*, 83(11):6700, 1998.

[95] V. Chandrasekhar, Z. Ovadyahu, and R. A. Webb. Single-electron charging effects in insulating wires. *Phys. Rev. Lett.*, 67:2862, 1991.

[96] S. Gregory. Inelastic tunneling spectroscopy and single-electron tunneling in an adjustable microscopic tunnel junction. *Phys. Rev. Lett.*, 64:689, 1990.

[97] R. Wilkins, E. Ben-Jacob, and R. C. Jaklevic. Scanning tunneling microscope observations of Coulomb blockade and oxide polarization in small metal droplets. *Phys. Rev. Lett.*, 63:801, 1989.

[98] J. B. Barner and S. T. Ruggiero. Observation of the incremental charging of Ag particles by single electrons. *Phys. Rev. Lett.*, 59:807, 1987.

[99] L. S. Kuz'min and K. K. Likharev. Direct experimental observation of discrete correlated single-electron tunneling. *JETP Lett.*, 45:495, 1987.

[100] P. J. M. Bentum, T. T. M. Smokers, and H. van Kempen. Incremental charging of single small particles. *Phys. Rev. Lett.*, 60:2543, 1988.

[101] C. W. J. Beenakker. Theory of Coulomb-blockade oscillations in the conductance of a quantum dot. *Phy. Rev. B*, 44:1646, 1991.

[102] S. Sankar, B. Dieny, and A. E. Berkowitz. Spin-polarized tunneling in discontinuous $CoFe/HfO_2$ multilayers. *J. Appl. Phys.*, 81:5512, 1997.

[103] K. Ono, H. Shimada, S. Kobayashi, and Y. Ootuka. Magnetoresistance of Ni/NiO/Co small tunnel junctions in Coulomb blockade regime. *J. Phys. Soc. Jpn.*, 65:3449, 1996.

[104] K. Ono, H. Shimada, and Y. Ootuka. Spin polarization and magneto-Coulomb oscillations in ferromagnetic single electron devices. *J. Phys. Soc. Jpn.*, 66:1261, 1998.

[105] L. F. Schelp, A. Fert, F. Fettar, P. Holody, S. F. Lee, J. L. Maurice, F. Petroff, and A. Vaures. Spin-dependent tunneling with Coulomb blockade. *Phys. Rev. B*, 56:R5747, 1997.

[106] R. Desmicht, G. Faini, V. Cros, A. Fert, F. Petroff, and A. Vaures. Point-contact electrodes to probe charging effects in individual ultrasmall cobalt clusters. *App. Phys. Lett.*, 72:386, 1998.

[107] J. Barnaś and A. Fert. Magnetoresistance oscillations due to charging effects in double ferromagnetic tunnel junctions. *Phys. Rev. Lett.*, 80:1058, 1998.

[108] K. Majumdar and S. Hershfield. Magnetoresistance of the double-tunnel-junction Coulomb blockade with magnetic metals. *Phys. Rev. B*, 57:11 521, 1998.

[109] A. Brataas, Yu. V. Nazarov, J. Inoue, and Gerrit E. W. Bauer. Spin-accumulation in small ferromagnetic double barrier junctions. *To appear in Euro. Phys. Jour. B, cond-mat/9811179*, 1998.

[110] K. Wang, S. Zhang, P. M. Levy, L. Szunyogh, and P. Weinberger. Role of electronic structure in magnetic tunneling. 1998. Unpublished.

[111] S. Zhang and P. M. Levy. Models for magnetoresistance in tunnel junctions. 1998. Unpublished.

[112] S. Zhang and P. M. Levy. Magnetoresistance of magnetic tunnel junctions in the presence of a non-magnetic layer. 1998. Unpublished.

[113] G. A. Prinz. Spin-polarized transport. *Phys. Today*, 48:24, 1995.

[114] J. M. Daughton. Magnetic tunneling applied to memory. *J. Appl. Phys.*, 8:3758, 1997.

[115] A. D. Kent, T. M. Shaw, S. von Molnar, and D. D. Awschalom. Growth of high aspect ratio nanometer-scale magnets with chemical vapor deposition and scanning tunneling microscopy. *Science*, 262:1249, 1993.

[116] A. D. Kent, S. von Molnar, S. Gider, and D. D. Awschalom. Properties and measurement of scanning tunneling microscope fabricated ferromagnetic particle arrays. *J. Appl. Phys.*, 76:6656, 1994.

[117] W. Wernsdorfer, B. Doudin, D. Mailly, K. Hasselbach, A. Benoit, J. Meiera, J.-Ph Ansermet, and B. Barbara. Magnetization reversal in single ferromagnetic Ni and Co particles. *Phys. Rev. Lett.*, 77:1873, 1996.

[118] W. Wernsdorfer, K. Hasselbach, D. Mailly, B. Barbara, A. Benoit, L. Thomas, and G. Suran. Magnetization of single magnetic particles. *J. Magn. Magn. Mater.*, 140–144:389, 1995.

[119] M. Lederman, S. Schultz, and M. Ozaki. Measurement of the dynamics of the magnetization reversal in individual single-domain ferromagnetic particles. *Phys. Rev. Lett.*, 73:1986, 1994.

[120] H. L. Richards, M. A. Novotny, and P. A. Rikvold. Analytical and computational study of magnetization switching in kinetic Ising systems with demagnetizing fields. *Phys. Rev. B*, 54:4113, 1996.

[121] H. L. Richards, S. W. Sides, M. A. Novotny, and P. A. Rikvold. Effects of boundary conditions on magnetization switching in kinetic Ising models of nanoscale ferromagnets. *J. Magn. Magn. Mater.*, 150:37, 1995.

[122] H. L. Richards, S. W. Sides, M. A. Novotny, and P. A. Rikvold. Kinetic Ising systems as models of magnetization switching in submicron ferromagnets. *J. Appl. Phys.*, 79:5749, 1996.

[123] J. Lee, M. A. Novotny, and P. A. Rikvold. Method to study relaxation of metastable phases: macroscopic mean-field dynamics. *Phys. Rev. E*, 52:356, 1995.

[124] H. L. Richards, M. Kolesik, P. Lindgard, P. A. Rikvold, and M. A. Novotny. Effects of boundary conditions on magnetization switching in kinetic Ising models of nanoscale ferromagnets. *Phys. Rev. B*, 55:11 521, 1997.

[125] C. C. A. Gunther, P. A. Rikvold, and M. A. Novotny. Application of a constrained-transfer-matrix method to metastability in the $d = 2$ Ising ferromagnets. *Physica A*, 212:194, 1994.

[126] P. A. Rikvold, H. Tomita, S. Miyashita, and S. W. Sides. Metastable lifetimes in a kinetic Ising model: dependence on field and system size. *Phys. Rev. E*, 49:5080, 1994.

[127] J. D. Gunton, M. San Miguel, and P. S. Sahni. In C. Domb and J. L. Lebowitz, editors, *Phase Transitions and Critical Phenomena, Vol 8*, New York, 1983. Academic.

[128] L. Néel. Magnetism and local molecular field. *Science*, 174:985, 1971.

[129] W. F. Brown Jr. *Magnetostatic Principles in Ferromagnetism.* North-Holland, Amsterdam, 1962.

[130] W. F. Brown Jr. *Micromagnetics.* Wiley, New York, 1963.

[131] A. Aharoni. *Introduction to the Theory of Ferromagnetism.* Clarendon, Oxford, New York, 1996.

[132] P. A. Rikvold and B. M. Gorman. In D. Stauffer, editor, *Annual Reviews of Computational Physics I*, Singapore, 1994. World Scientific. References therein.

[133] T. Chang, J.-G. Zhu, and J. H. Judy. Method for investigating the reversal properties of isolated barium ferrite fine particles utilizing magnetic force microscopy (MFM). *J. Appl. Phys.*, 73:6716, 1993.

[134] Y. Luo and J.-G. Zhu. Switching field characteristics of individual iron particles by MFM. *IEEE Trans. Magn.*, 30:4080, 1994.

[135] N. S. Wei and S. Y. Chou. Size effects on switching field of isolated and interactive arrays of nanoscale single-domain Ni bars fabricated using electron-beam nanolithography. *J. Appl. Phys.*, 76:6679, 1994.

[136] S. Shtrikman and D. Treves. *Magnetism III.* Academic, New York, 1963.

[137] J. H. Van Vleck. On the anisotropy of cubic ferromagnetic crystals. *Phys. Rev.*, 32:1178, 1937.

[138] U. Gradmann. Magnetic surface anisotropies. *J. Magn. Magn. Mater.*, 54-57:733, 1986.

[139] H. J. Elmers, G. Liu, and U. Gradmann. Magnetometry of the ferromagnetic monolayer Fe(110) on W(110) coated with Ag. *Phys. Rev. Lett.*, 63:566, 1989.

[140] B. Heinrich, Z. Celinski, J. F. Cochran, A. S. Arrott, and K. Myrtle. Magnetic anisotropies in single and multilayered structures. *J. Appl. Phys.*, 70:5769, 1991.

[141] B. Heinrich, K. B. Urquhart, A. S. Arrott, J. F. Cochran, K. Myrtle, and S. T. Purcell. Ferromagnetic-resonance study of ultrathin BCC Fe(100) films grown epitaxially on FCC Ag(100) substrates. *Phys. Rev. Lett.*, 59:1756, 1987.

[142] M. Sakurai. Magnetic anisotropy of epitaxial Fe/Pt(001) multilayers. *Phys. Rev. B*, 50:3761, 1994.

[143] E. D. Dahlberg and J.-G Zhu. Micromagnetic microscopy and modeling. *Phys. Today*, 48:34, 1995.

[144] J.-G Zhu and H. N. Bertram. Micromagnetic studies of thin metallic films. *J. Appl. Phys.*, 63:3248, 1988.

[145] J.-G Zhu and H. N. Bertram. Magnetization structures in thin-film recording media. *IEEE Trans. Magn.*, 27:3553, 1991.

[146] A. Aharoni. Surface anisotropy in micromagnetics. *J. Appl. Phys.*, 61:3302, 1987.

[147] T. Kaneyoshi. *Introduction to Surface Magnetism.* CRC Press, Boca Raton, 1991.

[148] B. T. Jonker, K.-H. Walker, E. Kisker, G. A. Prinz, and C. Carbone. Spin-polarized photoemission study of epitaxial Fe(001) films on Ag(001). *Phys. Rev. Lett.*, 57:142, 1986.

[149] N. C. Koon, B. T. Jonker, F. A. Volkening, J. J. Krebs, and G. A. Prinz. Direct evidence for perpendicular spin orientations and enhanced hyperfine fields in ultrathin Fe(100) films on Ag(100). *Phys. Rev. Lett.*, 59:2463, 1987.

[150] C. L. Wooten, J. Chen, G. A. Mulhollan, J. L. Erskine, and J. T. Market. Direct observation of enhanced magnetic moments in Fe/Ag(100). 1998. Unpublished.

[151] S. Ohnishi, A. J. Freeman, and M. Weinert. Surface magnetism of Fe (001). *Phys. Rev. B*, 28:6741, 1983.

[152] M. Alden, S. Mirbt, H. L. Skriver, N. M. Rosengaard, and B. Johansson. Surface magnetism in iron, cobalt, and nickel. *Phys. Rev. B*, 46:6303, 1992.

[153] C. L. Fu, A. J. Freeman, and T. Oguchi. Prediction of strongly enhanced two-dimensional ferromagnetic moments on metallic overlayers, interfaces, and superlattices. *Phys. Rev. Lett.*, 54:2700, 1985.

[154] J. G. Gay and R. Richter. Spin anisotropy of ferromagnetic films. *Phys. Rev. Lett.*, 56:2728, 1986.

[155] O. Jepsen, J. Madsen, and O. K. Andersen. Spin-polarized electronic structure of the Ni(001) surface and thin films. *Phys. Rev. B*, 26:2790, 1982.

[156] X. Zhu and J. Hermanson. Energy bands and magnetization of a Ni(001) monolayer. *Phys. Rev. B*, 27:2092, 1983.

[157] E. Wimmer, A. J. Freeman, and H. Krakauer. Magnetism at the Ni(001) surface: a high-precision, all-electron local-spin-density-functional study. *Phys. Rev. B*, 30:3113, 1984.

[158] F. Weling and J. Callaway. Semiempirical description of energy bands in nickel. *Phys. Rev. B*, 26:710, 1982.

[159] J. Kanamori. In G. Rado and H. Suhl, editors, *Magnetism*, New York, 1963. Academic.

[160] L. Szunyogh, B. Ujfalussy, and P. Weinberger. Magnetic anisotropy of iron multilayers on Au(001): first-principles calculations in terms of the fully relativistic spin-polarized screened KKR method. *Phys. Rev. B*, 51:9552, 1995.

[161] R. Coehoorn. First principles band structure calculations for rare earth-transition metal compounds: magnetization, hyperfine parameters and magnetocrystalline anisotropy. *J. Magn. Magn. Mater.*, 99:55, 1991.

[162] D. Wang, R. Wu, and A. J. Freeman. First-principles theory of surface magnetocrystalline anisotropy and the diatomic-pair model. *Phys. Rev. B*, 47:14 932, 1993.

[163] M. Asdente and M. Delitala. Magnetocrystalline energy, electronic charge distribution, and Fermi surface of iron from a tight-binding calculation. *Phys. Rev.*, 163:497, 1967.

[164] M. Cinal, D. M. Edwards, and J. Mathon. Magnetocrystalline anisotropy in ferromagnetic films. *Phys. Rev. B*, 50:3754, 1994.

[165] P. Bruno. Tight-binding approach to the orbital magnetic moment and magnetocrystalline anisotropy of transition-metal monolayers. *Phys. Rev. B*, 39:865, 1989.

[166] A. Lessard, T. H. Moos, and W. Hubner. Magnetocrystalline anisotropy energy of transition-metal thin films: a nonperturbative theory. *Phys. Rev. B*, 56:2594, 1997.

[167] S. V. Beiden, W. M. Temmerman, Z. Szotek, G. A. Gehring, G. M. Stocks, Y. Wang, D. M. C. Nicholson, W. A. Shelton, and H. Ebert. Real-space approach to the calculation of magnetocrystalline anisotropy in metals. *Phys. Rev. B*, 57:14 247, 1998.

[168] E. Abate and M. Asdente. Tight-binding calculation of 3d bands of Fe with and without spin-orbit coupling. *Phys. Rev.*, 140:1303, 1965.

[169] A. J. Bennett and B. R. Cooper. Origin of the magnetic 'surface anisotropy' of thin ferromagnetic films. *Phys. Rev. B*, 3:1642, 1971.

[170] H. Takayama, K. Bohnen, and P. Fulde. Magnetic surface anisotropy of transition metals. *Phys. Rev. B*, 14:2287, 1976.

[171] L. D. Landau and E. M. Lifshitz. *Electrodynamics of continuous media.* Pergamon Press, Oxford, 1960.

[172] D. N. Astrov. The magnetoelectric effect in antiferromagnetics. *Sov. Phys. JETP*, 11:708, 1960.

[173] G. T. Rado. Mechanism of the magnetoelectric effect in an antiferromagnet. *Phys. Rev. Lett.*, 6:609, 1961.

[174] G. T. Rado and J. M. Ferrari. Electric field dependence of the magnetic anisotropy energy in magnetite (Fe_3O_4). *Phys. Rev. B*, 12:5166, 1975.

[175] L. E. Gurevich and D. A. Flippov. Theory of linear magnetoelectric effect in antiferromagnets. *Sov. Phys. Solid State*, 28:1510, 1986.

[176] J. C. Slonczewski. Current-driven excitation of magnetic multilayers. *J. Magn. Magn. Mater.*, 159:L1, 1996.

[177] Ya. B. Bazaliy, B. A. Jones, and S-C. Zhang. Modification of the Landau-Lifshitz equation in the presence of a spin-polarized current in colossal- and giant-magnetoresistive materials. *Phys. Rev. B*, 57:R3213, 1998.

[178] L. Berger. Emission of spin waves by a magnetic multilayer traversed by a current. *Phys. Rev. B*, 54:9353, 1996.

[179] M. A. M. Gijs and G. E. W. Bauer. Perpendicular giant magnetoresistance of magnetic multilayers. *Adv. Phys.*, 46:285, 1997.

[180] In M. Abramowitz and I. A. Stegun, editors, *Handbook of Mathematical Functions*, New York, 1972. Dover.

[181] Bruce A. Gurney, Virgil S. Speriosu, Jean-Pierre Nozieres, Harry Lefakis, Dennis R. Wilhoit, and Omar U. Need. Direct measurement of spin-dependent conduction-electron mean free paths in ferromagnetic metals. *Phys. Rev. Lett.*, 71:4023, 1993.

[182] M. D. Stiles. Spin-dependent interface transmission and reflection in magnetic multilayers. *J. Appl. Phys.*, 79:5805, 1996.

[183] C. Cercignani. In F. John, J. E. Marsden, and L. Sirovich, editors, *Theory and Application of the Boltzmann Equation*, New York, 1975. Elsevier.

[184] D. K. C. MacDonald and K. Sarginson. Size effect variation of the electrical conductivity of metals. *Proc. Roy. Soc. A*, 203:223, 1950.

[185] R. B. Dingle. The electrical conductivity of thin wires. *Proc. Roy. Soc. A*, 201:545, 1950.

[186] R. G. Chambers. The conductivity of thin wires in a magnetic field. *Proc. Roy. Soc. A*, 202:378, 1950.

[187] J. M. Ziman. *Principles of the Theory of Solids.* Cambridge Univ. Press, Cambridge, 1965.

[188] R. Lenk and A. Knábchen. The roughness-induced classical size effect in thin films. *J. Phys.: Condens. Matter*, 5:6563, 1993.

[189] G. Fishman and D. Calecki. Surface-induced resistivity of ultrathin metallic films: a limit law. *Phys. Rev. Lett.*, 62:1302, 1989.

[190] P. M. Levy and S. Zhang. Spin dependent tunneling. 1998. A short review (to be published).

[191] J. Lambe and R. C. Jaklevic. Charge-quantization studies using a tunnel capacitor. *Phys. Rev. Lett.*, 22:1371, 1969.

[192] M. Amman, K. Mullen, and E. Ben-Jacob. The charge-effect transistor. *J. Appl. Phys.*, 65:339, 1989.

[193] K. K. Likharev. Single-electron transistors: electrostatic analogs of the DC SQUIDs. *IEEE Trans. Magn.*, MAG-23:1142, 1987.

[194] H. Tamura and S. Hasuo. Analysis of a field-effect transistor with a channel made of ultrafine metal particles. *J. Appl. Phys.*, 62:3036, 1987.

[195] M. Amman, R. Wilkins, E. Ben-Jacob, P. D. Maker, and R. C. Jaklevic. Analytic solution for the current-voltage characteristic of two mesoscopic tunnel junctions coupled in series. *Phys. Rev. B*, 43:1146, 1991.

[196] S. Hershfield, J. H. Davies, P. Hyldgaard, C. J. Stanton, and J. W. Wilkins. Zero-frequency current noise for the double-tunnel-junction Coulomb blockade. *Phys. Rev. B*, 47:1967, 1993.

[197] B. Laikhtman. Current-voltage characteristic of double normal tunnel junctions. *Phys. Rev. B*, 43:2731, 1991.

[198] S. H. Chang, J. Nowak, R. Jansen, and J. S. Moodera. Temperature dependence of magnetoresistance and surface magnetization in ferromagnetic tunnel junctions. *Phys. Rev. B*, 58:R2917, 1998.

[199] D. A. Papaconstantopoulos. *Handbook of the Band Structure of Elemental Solids.* Plenum Press, New York, 1986.

[200] J. C. Slater and G. F. Koster. Simplified LCAO method for the periodic potential problem. *Phys. Rev.*, 94:1498, 1954.

[201] W. A. Harrison. *Electronic Structure and the Properties of Solids.* Freeman, San Francisco, 1980.

[202] B. H. Bransden and C. J. Joachain. *Physics of Atoms and Molecules.* Longman, New York, 1983.

[203] C. M. Moore. *Selected Tables of Atomic Spectra.* National Bureau of Standards, Washington D. C., 1965.

[204] U. Pustogowa, W. Hubner, and K. H. Bennemann. Theory for the nonlinear magneto-optical Kerr effect at ferromagnetic transition-metal surfaces. *Phys. Rev. B*, 48:8607, 1993.

[205] R. Jansen and J. S. Moodera. Influence of barrier impurities on the magnetoresistance in ferromagnetic tunnel junctions. *J. Appl. Phys.*, 83(11):6682, 1998.

[206] F. Steglich, B. Buschinger, P. Gegenwart, M. Lohmann, R. Helfrich, C. Langhammer, P. Hellman, L. Donnevert, S. Thomas, A. Link, C. Geibel, M. Lang, G. Sparn, and W. Assmus. Quantum critical phenomena in undoped heavy-fermion metals. *J. Phys.: Condens. Matter*, 8:9909, 1996.

[207] K. Umeo, H. Kadomatsu, and T. Takabatake. Non-Fermi-liquid behaviour at the pressure-induced antiferromagnetic to nonmagnetic transition in a heavy-fermion compound, Ce_7Ni_3. *J. Phys.: Condens. Matter*, 8:9743, 1996.

[208] D. Belitz and T. R. Kirkpatrick. Quantum critical behaviour of itinerant ferromagnets. *J. Phys.: Condens. Matter*, 8:9707, 1996.

BIOGRAPHICAL SKETCH

Kingshuk Majumdar was born on January 27, 1968 in West-Bengal, India. He was awarded national merit scholarship for his performance in the secondary examination in 1984. After finishing his higher secondary studies in 1986 he went to Presidency College, Calcutta for undergraduate education. He obtained his B.Sc degree with first class in physics in 1989. He received UGC (University Grant Commission) scholarship for his achievement in the B. Sc examination. In 1992, Kingshuk graduated from University of Calcutta with a M. Sc degree in physics. After spending few months in the physics department of Indian Statistical Institute as a research scholar he came to University of Florida, Gainesville in the fall of 1993 to pursue doctoral research in physics. In the spring of 1995, he joined the research group of Professor Selman Hershfield to begin work in theoretical condensed matter physics. He received "outstanding academic achievement award by an international student" by University of Florida in 1997. He also won the second prize for oral presentation of his work in the Graduate Student Forum of University of Florida in 1998. This thesis is the collection of works Kingshuk did on magnetic nanostructures. Besides the work of this dissertation, he has also published work on non-equilibrium Kondo impurity.

I certify that I have read this study and that in my opinion it conforms to acceptable standards of scholarly presentation and is fully adequate, in scope and quality, as a dissertation for the degree of Doctor of Philosophy.

S. Hershfield, Chairman
Associate Professor of Physics

I certify that I have read this study and that in my opinion it conforms to acceptable standards of scholarly presentation and is fully adequate, in scope and quality, as a dissertation for the degree of Doctor of Philosophy.

K. Muttalib
Associate Professor of Physics

I certify that I have read this study and that in my opinion it conforms to acceptable standards of scholarly presentation and is fully adequate, in scope and quality, as a dissertation for the degree of Doctor of Philosophy.

P. Hirschfeld
Associate Professor of Physics

I certify that I have read this study and that in my opinion it conforms to acceptable standards of scholarly presentation and is fully adequate, in scope and quality, as a dissertation for the degree of Doctor of Philosophy.

D. Tanner
Professor of Physics

I certify that I have read this study and that in my opinion it conforms to acceptable standards of scholarly presentation and is fully adequate, in scope and quality, as a dissertation for the degree of Doctor of Philosophy.

S. Pearton
Professor of Materials Science
and Engineering

This dissertation was submitted to the Graduate Faculty of the Department of Physics in the College of Liberal Arts and Sciences and to the Graduate School and was accepted as partial fulfillment of the requirments for the degree of Doctor of Philosophy.

May 1999

Dean, Graduate School